TECHNISCHE UNIVERSITÄT WIEN
Vienna | Austria

Diploma Thesis

COMPARISON OF ANALYTICAL AND NUMERICAL MODELS FOR COMPOSITES WITH SPHERE-SHAPED REINFORCEMENTS

carried out for the purpose of obtaining the degree of Master of Science (MSc or Diplom-Ingenieur or Dipl.-Ing or DI), submitted at TU Wien, Faculty of Mechanical and Industrial Engineering, by

Christoph KLANCNIK, BSc

01225587

Waldgasse 3

2500 Baden

under the supervision of

Ao.Univ.Prof. Dipl.-Ing. Dr.techn. Helmut Böhm

Institute of Lightweight Design and Structural Biomechanics

Vienna, on Name

I confirm, that going to press of this thesis needs the confirmation of the examination committee.

Affidavit

I declare in lieu of oath, that I wrote this thesis and performed the associated research myself, using only literature cited in this volume. If text passages from sources are used literally, they are marked as such.

I confirm that this work is original and has not been submitted elsewhere for any examination, nor it is currently under consideration for a thesis elsewhere.

Vienna, August, 2017

Signature

Acknowledgment

I would first like to thank my thesis advisor, Ao.Univ.Prof. Dipl.-Ing. Dr.techn. Helmut Böhm, of the Institute of Lightweight Design and Structural Biomechanics at TU Wien. Prof. Böhm has always taken the time when I needed it and was available whenever I had a question in general or about a particular topic.
I would also like to thank the whole team of the Institute of Lightweight Design and Structural Biomechanics at TU Wien. Without the resources and software provided this thesis could not be finished.
Finally, I must express my gratitude to my parents, family and friends for providing me with support and encouragement throughout my years of study. This accomplishment would not have been possible without them.

Thank you.

Contents

Abstract

The aim of this thesis was to compare predictions of the macroscopic linear elastic responses of two-phase composites. These were obtained by analytical models and numerical methods. The fictitious composite being studied consists of a matrix reinforced by randomly dispersed, spherical particles of identical size.

The analytical approaches used are highly developed statistics-based models which, in turn, provide bounds and estimates of the different elastic parameters.
The numerical predictions are obtained by discrete multi-particle models and take advantage of finite element modelling for periodic homogenization.
These analytical models and numerical methods were applied for different reinforcement volume fractions and elastic contrasts.

In general, there is good agreement between the analytical and the numerical predictions. Differences were found in the linear elastic response of different mesh types.

Kurzfassung

Das Ziel dieser Arbeit war es, theoretische Vorhersagen über das linear elastische Verhalten von zweiphasigen Composites, erlangt durch analytische Modelle und numerische Methoden, zu vergleichen. Das zu untersuchende fiktive Composite besteht aus einer Matrix welche durch zufällig angeordnete kugelförmige Partikel gleicher Größe verstärkt wird.

Bei den analytischen Modellen handelt es sich um hochentwickelte statistik-basierte Verfahren, welche einerseits Schranken (engl. bounds) und andererseits Abschätzungen (engl. estimates) der Materialparameter liefern.
Bei den numerischen Vorhersagen handelt es sich um diskrete Multi-Partikel Modelle welche das Verfahren der Finite Elemente für die periodische Homogenisierung einsetzen.
Die genannten analytischen Modelle und numerischen Methoden wurden für verschiedene Verstärkungs-Volumsfraktionen und elastische Kontraste untersucht.

Im Allgemeinen gib es gute Übereinstimmung zwischen den Vorhersagen der analytischen Modelle und den numerischen Vorhersagen. Zwischen den Vorhersagen verschiedener Vernetzungsstrategien wurden Unterschiede festgestellt.

Notation

In this work, tensors of rank four are represented by bold capital Roman letters (e.g., $\mathbf{A}$, $\mathbf{B}$). Tensors of rank two are described by bold lower case Greek letters (e.g., $\boldsymbol{\sigma}$, $\boldsymbol{\varepsilon}$). Vectors are represented by bold lower case Roman letters (e.g., $\mathbf{u}$, $\mathbf{x}$). Scalars are described by non-bold Italic or Greek letters (e.g., E, σ, c_{el}).

Voigt-Nye notation [22] is used in this thesis. This means that Hooke's law $\boldsymbol{\sigma} = \mathbf{E}\boldsymbol{\varepsilon}$ can be written as

$$\begin{bmatrix} \sigma_{11} \\ \sigma_{22} \\ \sigma_{33} \\ \sigma_{23} \\ \sigma_{13} \\ \sigma_{12} \end{bmatrix} = \begin{bmatrix} E_{11} & E_{12} & E_{13} & E_{14} & E_{15} & E_{16} \\ E_{21} & E_{22} & E_{23} & E_{24} & E_{25} & E_{26} \\ E_{31} & E_{32} & E_{33} & E_{34} & E_{35} & E_{36} \\ E_{41} & E_{42} & E_{43} & E_{44} & E_{45} & E_{46} \\ E_{51} & E_{52} & E_{53} & E_{54} & E_{55} & E_{56} \\ E_{61} & E_{62} & E_{63} & E_{64} & E_{65} & E_{66} \end{bmatrix} \begin{bmatrix} \varepsilon_{11} \\ \varepsilon_{22} \\ \varepsilon_{33} \\ \gamma_{23} \\ \gamma_{13} \\ \gamma_{12} \end{bmatrix} \tag{1}$$

wherein $\gamma_{ij} = 2\varepsilon_{ij}$, $i \neq j$ represents the shear angles [20].

The subscripts m and i denote the specific constituents of a two-phase matrix-inclusion topology. A subscript p is used when the inhomogeneities occur in form of particles.

Chapter 1

Introduction

1.1 Motivation

The use of composites has increased rapidly with new manufacturing methods and increased demands on materials and structures. Composites can have two or more different phases. Inhomogeneities dispersed in a matrix or laminated layers of two materials belong to the so called two-phase composites. Reinforcing an elastic homogeneous isotropic matrix with elastic homogeneous isotropic equiaxed particles will change the effective material properties depending on the particle volume fraction. These particle reinforced composites have a wide range of use and, therefore, there is considerable interest in good estimates for their effective material properties.
There exist a wide range of analytical tools for obtaining the effective material properties of such two-phase elastic composites. Some of them give an estimated value for a given modulus of a given configuration and others provide a range of values for the effective material properties, the so called bounds. With the falling costs of computational power it has become favourable to use the Finite Element Method to predict the effective material properties of said composites.
In most of the analytical models of particle reinforced composites the particles are approximated by spheres. This will be applied in this thesis as well.

This work will compare selected analytical estimates and bounds with the effective linear-elastic material properties predicted by finite element modelling of appropriate volume elements.
Using the commercial micromechanics code *Digimat* (e-Xstream, Luxembourg, and MSC Software, Newport Beach, 2017), a fictitious composite with different elastic contrasts c_{el} consisting of a matrix reinforced by identical spherical inhomogeneous will be modelled and analysed.

1.1.1 Some Words on Literature

A considerable amount of research work on the linear-elastic material behaviour of composite materials has been published over the past decades. In addition finite element based modelling has been applied to evaluating the effective material properties, for example [25].
A brief summary and introduction into the field of micromechanics is given by Böhm [3]. This report covers the main aspects and gives a good overview of common used methods.
One of the methods considered in this thesis are the widely used Hashin-Shtrikman bounds [10]. The sharper three-point bounds, derived by Beran and Molyneux [1], are used as one of the main references. Another important piece of work on effective material properties was done by Torquato [27][26], the resulting estimates play a considerable role in this thesis.
The influence of different sets of statistical parameters for hard impenetrable random dispersed spheres will be discussed as well.

1.2 Assumptions of the Present Thesis

There are some main assumptions and simplifications which were used in this thesis. First of all the inhomogeneities are particles which are considered as identical in shape and uniform in size. Also the particles are randomly embedded in a matrix, creating a nearly isotropic macroscopic material behaviour. The study is limited to linear-elastic, small strain behaviour of said composites. This thesis examines the behaviour at given elastic contrasts c_{el} between two constitutes. The used material properties are normalized with respect to the matrix and, therefore, are treated as non-dimensional.

Chapter 2

Methods

There are various methods for obtaining the effective material properties of two-phase composites made of elastic isotropic impenetrable spheres embedded in an elastic isotropic matrix. They are called mean-field methods, bounding methods and full-field models. The focus in this thesis lies on the bounding methods, see Section 2.4, and the use of periodic microfields models, a type of full-field model, see Section 2.5.
Before going into detail of the topics mentioned above, a short general introduction is given.

2.0.1 Scales

When talking about micromechanics it is unavoidable to talk about the different length scales used to describe the material properties and the geometry. The macroscale is the largest one to be used, corresponding to the length scale of the structure or sample made of the material to be studied. On the opposite side the microscale is the smallest one, describing the length of an inhomogeneity. In-between the micro- and macroscale there is at least one mesoscale. It is an intermediate length scale which gives information on the geometries of the structure, for example the position of particles. Therefore the model size corresponds to the mesoscale.

Using these length scales allows separating the stress and strain-fields into two contributions [3]

$$\boldsymbol{\varepsilon}(\boldsymbol{x}) = \langle \boldsymbol{\varepsilon} \rangle + \boldsymbol{\varepsilon}'(\boldsymbol{x}) \qquad \text{and} \qquad \boldsymbol{\sigma}(\boldsymbol{x}) = \langle \boldsymbol{\sigma} \rangle + \boldsymbol{\sigma}'(\boldsymbol{x}). \tag{2.1}$$

wherein the variables in the angled brackets $\langle \star \rangle$ are contributions on the macroscopic level, i.e., averaged fields. A prime $\star'$ denotes variables fluctuating at the microscale.

2.0.2 Volume Fraction

The volume fraction ξ is the most important geometrical parameter when considering particle reinforced composites. It is defined as

$$\xi_k = \frac{V_k}{\sum_l V_l} \tag{2.2}$$

wherein V_k is the volume of the desired phase and $\sum_l V_l$ is the combined volume of all phases. Beside the material properties of the different phases, the volume fraction is the main parameter needed to give a first appraisal of the macroscopic material properties.

2.0.3 Elastic Contrast

Another important parameter of linear-elastic two-phase composites is the so called elastic contrast c_{el}. It is defined as

$$c_{\mathrm{el}} = \frac{E_{\mathrm{i}}}{E_{\mathrm{m}}} \tag{2.3}$$

wherein the E_{i} defines the Young's modulus of the inhomogeneities and E_{m} the Young's modulus of the matrix. It can be seen as a parameter of inhomogeneity of the two-phase composite material behaviour.

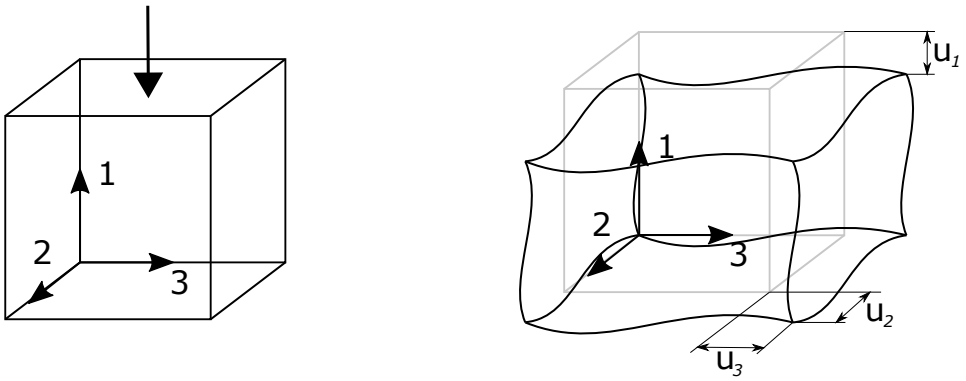

(a) Undeformed shape with applied load

(b) Deformed shape with displacements

Figure 2.1: Schematic illustration of a volume element with periodic boundary conditions and a macroscopic load acting in direction 1

2.1 Material Properties

Evaluation of Effective Material Properties

To acquire the linear-elastic material properties of a given three-dimensional unit cell, six linearly independent load cases have to be applied.

For example, consider a three-dimensional volume element subjected to a load in direction 1, see figure 2.1, inspired by [14]. This causes a volume averaged normal stress only in said direction

$$\langle \sigma_{11} \rangle \neq 0, \qquad \langle \sigma_{22} \rangle = \langle \sigma_{33} \rangle = 0 \tag{2.4}$$

There are displacements u_1, u_2, u_3 in all three directions. Considering a positive Poisson's ratio, linear-elastic material behaviour and small strain the volume averaged strains can be calculated as

$$\langle \varepsilon_{11} \rangle = \frac{u_1}{L}, \qquad \langle \varepsilon_{22} \rangle = \frac{u_2}{L}, \qquad \langle \varepsilon_{33} \rangle = \frac{u_3}{L} \tag{2.5}$$

where L is the side length of the volume element. Hooke's law can than be written as

$$\begin{aligned}
\langle\varepsilon_{11}\rangle &= \frac{1}{E}\left[\langle\sigma_{11}\rangle - \nu\left(\langle\sigma_2 2\rangle + \langle\sigma_3 3\rangle\right)\right] \\
\langle\varepsilon_{22}\rangle &= \frac{1}{E}\left[\langle\sigma_{22}\rangle - \nu\left(\langle\sigma_{11}\rangle + \langle\sigma_{33}\rangle\right)\right] \\
\langle\varepsilon_{33}\rangle &= \frac{1}{E}\left[\langle\sigma_{33}\rangle - \nu\left(\langle\sigma_{11}\rangle + \langle\sigma_{22}\rangle\right)\right]
\end{aligned} \tag{2.6}$$

Substituting equations (2.5) and (2.4) into equation (2.6) leads to expressions for the Young's modulus and the Poisson's ratio in the load direction

$$E^1 = \frac{L}{u_1}, \qquad \nu^{12} = -\frac{u_2}{u_1}, \qquad \nu^{13} = -\frac{u_3}{u_1} \tag{2.7}$$

wherein the superscripts indicate the direction according to figure 2.1.
The material properties of the other directions can be computed using the same logic. In general one would obtain six different systems of equation of the type

$$\begin{bmatrix} \sigma_{11} \\ \sigma_{22} \\ \sigma_{33} \\ \sigma_{23} \\ \sigma_{13} \\ \sigma_{12} \end{bmatrix} = \begin{bmatrix} E_{11} & E_{12} & E_{13} & E_{14} & E_{15} & E_{16} \\ & E_{22} & E_{23} & E_{24} & E_{25} & E_{26} \\ & & E_{33} & E_{34} & E_{35} & E_{36} \\ & & & E_{44} & E_{45} & E_{46} \\ & sym. & & & E_{55} & E_{56} \\ & & & & & E_{66} \end{bmatrix} \begin{bmatrix} \varepsilon_{11} \\ \varepsilon_{22} \\ \varepsilon_{33} \\ \gamma_{23} \\ \gamma_{13} \\ \gamma_{12} \end{bmatrix} \tag{2.8}$$

where E_{kl} are the different components of the elasticity tensor $\mathbf{E}$. This gives 36 equations for 36 unknown variables (disregarding the symmetry of $\mathbf{E}$).

Isotropic Material Behaviour

One target of the thesis is to acquire the isotropic stiffness and compliance tensors of two-phase composites reinforced by randomly positioned particles.

An isotropic material behaviour provides the same elastic response irrespective of the loading direction. The linear-elastic behaviour of an isotropic material is described by two independent parameters. For example, the compliance tensor $\mathbf{C}$ can be expressed using only the Young's modulus and the Poisson's ratio. The compliance tensor is defined as

$$\mathbf{E} = \mathbf{C}^{-1} \tag{2.9}$$

$$\mathbf{C} = \begin{bmatrix} \frac{1}{E} & -\frac{\nu}{E} & -\frac{\nu}{E} & 0 & 0 & 0 \\ -\frac{\nu}{E} & \frac{1}{E} & -\frac{\nu}{E} & 0 & 0 & 0 \\ -\frac{\nu}{E} & -\frac{\nu}{E} & \frac{1}{E} & 0 & 0 & 0 \\ 0 & 0 & 0 & \frac{2(1+\nu)}{E} & 0 & 0 \\ 0 & 0 & 0 & 0 & \frac{2(1+\nu)}{E} & 0 \\ 0 & 0 & 0 & 0 & 0 & \frac{2(1+\nu)}{E} \end{bmatrix} \tag{2.10}$$

where one can interpret $\frac{2(1+\nu)}{E}$ as $\frac{1}{G}$, the inverse of the shear modulus.

2.2 Modelling Approaches

In order to predict the material behaviour of composites, micromechanical models are needed. The major part of these modelling approaches can be assigned to two groups. The first group describes the material in terms of phase-wise uniform stress and strain fields [3]. Some methods of this type are

- Mean-Field Methods (abbr. MFM) which approximate the material behaviour through the phase averaged strain $\langle \boldsymbol{\varepsilon} \rangle$ and stress $\langle \boldsymbol{\sigma} \rangle$ of each constituent.
- Bounding Methods, which are described in section 2.4, use variational principles to restrict the material behaviour between an upper and lower bound.

The second group of methods deals with discrete microgeometries. They study the interactions between the different phases in a highly detailed way. Some examples are

- Embedded Cell Models (abbr. ECM) which consist of a cell, containing the discrete microgeometry, embedded in a region to which the far field loads are applied. They are good choices if specific arrangements or crack tips are to be studied [3].
- Windowing Approaches are used to study relatively small samples of a given material. The boundary conditions are chosen in a way that there is energy equivalence between the micro- and macroscales.
- Periodic Microfield Approaches (abbr. PMA) approximate the composite by using an infinite periodic phase arrangement, more on this in section 2.5.

2.3 Eshelby's Solution

When Eshelby studied the stress and strain distributions in homogeneous materials he considered a thought experiment which includes an ellipsoidal inclusion embedded in an elastic matrix of infinite size [8]. The aim was to obtain the stress and strain distributions for the case that the ellipsoidal inclusion changes its shape but is still constrained by the surrounding matrix. Eshelby's solution to this problem indicates that the strain $\boldsymbol{\varepsilon}_\mathrm{c}$ in the ellipsoidal constrained inclusion is uniform loaded with a homogeneous eigenstrain $\boldsymbol{\varepsilon}_\mathrm{t}$. The two strains are related via

$$\boldsymbol{\varepsilon}_\mathrm{c} = \mathbf{S}\boldsymbol{\varepsilon}_\mathrm{t} \tag{2.11}$$

wherein $\mathbf{S}$ denotes the so-called Eshelby tensor. It depends on the geometric shape of the inclusion and properties of the embedding material. Expressions for the Eshelby tensor of spherical inclusions can be found, for example, in [5].

2.4 Bounding Methods

With this group of methods the effective material properties, for example the moduli of isotropic materials, are described via lower and upper bounds, that give the physically possible range. There are a number of bounds available. Depending on the elastic contrast these bounds can give relatively good approximations of the material properties and are going to be compared with finite element models in this thesis.

2.4.1 Hill bounds

The Hill bounds [11] are so-called one-point bounds. These bounds are very simple and are even valid for small, non-representative volume elements. Only the phase volume fraction ξ is needed. They take the form [3]

$$\left[\sum_k \xi_k \mathbf{C}_k\right]^{-1} \leq \mathbf{E} \leq \sum_k \xi_k \mathbf{E}_k \tag{2.12}$$

wherein $\mathbf{E}_k$ is the elasticity tensor of phase k and $\mathbf{C}_k$ is the corresponding compliance tensor.

2.4.2 Hashin-Shtrikman Bounds

The Hashin-Shtrikman Bounds (abbr. HSB)[10] are the tightest bounds one can get with information on the phase volume fraction ξ and the macroscopic material symmetry. This type of bound is a two-point bound, because it can be written in terms of integrals that depend on the two-point probability function [29]. This function gives the probability that two points, which are separated by the vector $\mathbf{r}$, are located in a given combination of the two phases. The two-point correlation function is illustrated in figure 2.2. Hashin-Shtrikman bounds will be also the most slack bounds used as comparison in this thesis. With the use of the Hashin-Shtrikman variational principle the strain energy is bounded and, as a consequence, the effective

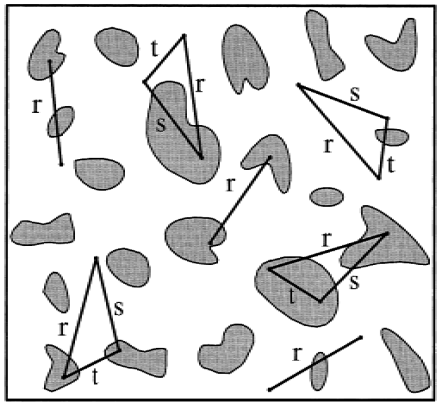

Figure 2.2: Illustration of the three-point (triangle made of **r**, **s** and **t**) and two-point (line **r**) correlation functions [29]

elastic moduli as well [10]. This leads to bounds on the elasticity tensor for two-phase composites which, for the case that the reinforcement is stiffer than the matrix, take the form [3]

$$\begin{aligned}\mathbf{E}_{\text{HS-}} &= \mathbf{E}_{\text{m}} + \xi_{\text{i}} \left[(\mathbf{E}_{\text{i}} - \mathbf{E}_{\text{m}})^{-1} + (1-\xi_{\text{i}})\mathbf{S}_{\text{m}}\mathbf{C}_{\text{m}} \right]^{-1} \\ &= \left[(1-\xi_{\text{i}})\mathbf{E}_{\text{m}}\bar{\mathbf{A}}^{\text{dil}}_{\text{m,m}} + \xi_{\text{i}}\mathbf{E}_{\text{i}}\bar{\mathbf{A}}^{\text{dil}}_{\text{i,m}} \right] \left[(1-\xi_{\text{i}})\bar{\mathbf{A}}^{\text{dil}}_{\text{m,m}} + \xi_{\text{i}}\bar{\mathbf{A}}^{\text{dil}}_{\text{i,m}} \right]^{-1}\end{aligned} \tag{2.13}$$

$$\begin{aligned}\mathbf{E}_{\text{HS+}} &= \mathbf{E}_{\text{i}} + \xi_{\text{i}} \left[(\mathbf{E}_{\text{m}} - \mathbf{E}_{\text{i}})^{-1} + (1-\xi_{\text{i}})\mathbf{S}_{\text{i}}\mathbf{C}_{\text{i}} \right]^{-1} \\ &= \left[(1-\xi_{\text{i}})\mathbf{E}_{\text{m}}\bar{\mathbf{A}}^{\text{dil}}_{\text{m,i}} + \xi_{\text{i}}\mathbf{E}_{\text{i}}\bar{\mathbf{A}}^{\text{dil}}_{\text{i,i}} \right] \left[(1-\xi_{\text{i}})\bar{\mathbf{A}}^{\text{dil}}_{\text{m,i}} + \xi_{\text{i}}\bar{\mathbf{A}}^{\text{dil}}_{\text{i,i}} \right]^{-1}\end{aligned} \tag{2.14}$$

wherein $\mathbf{S}$ is the Eshelby tensor for spherical inhomogeneities, see section 2.3 and equation (2.11). $\bar{\mathbf{A}}^{\text{dil}}_{k,l}$ is a strain concentration tensor describing a dilute inhomogeneity of material k embedded in material l.

$$\bar{\mathbf{A}}^{\text{dil}}_{k,l} = \left[\mathbf{I} + \mathbf{S}\mathbf{C}_l \left(\mathbf{E}_k - \mathbf{E}_l \right) \right]^{-1} \tag{2.15}$$

The bounds for the bulk and shear moduli can be evaluated directly from equation (2.13) and (2.14). Zimmerman shows how to derive bounds for the Poisson's ratio from bounds for the shear and bulk moduli [31].

Because the Hashin-Shtrikman bounds do not contain any information regarding the

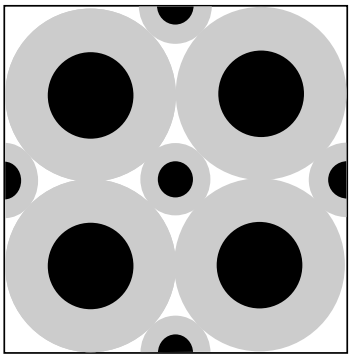

(a) most separated - lower bound

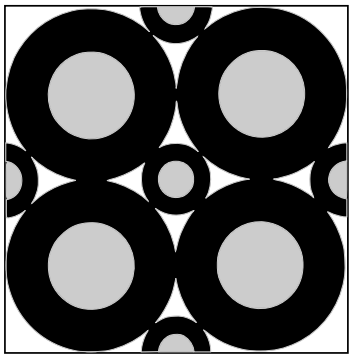

(b) most connected - upper bound

Figure 2.3: Illustration of the structure corresponding to the optimal upper and lower Hashin-Shtrikman bound according to Torquato [29]. Black denotes a phase stiffer than grey $K_{black} > K_{grey}$, $G_{black} > G_{grey}$

microgeometry beyond the two-point statistics, the upper and lower bound can be interpreted in terms of an arrangement proposed by Torquato [29]. The lower Hashin-Shtrikman bound would therefore correspond to an arrangement where the stiffer phase is the most "disconnected" due to the presence of the other phase. Conversely, for the upper Hashin-Shtrikman bound the stiffer phase is the most connected for the desired volume fraction [29]. There is an illustration in figure 2.3 showing a structure corresponding to the optimal upper and lower Hashin-Shtrikman bound. It only consists of a polydispersed composite sphere assemblage (abbr. CSA) with the diameters of the composite spheres becoming infinitesimally small and therefore filling the complete space. The white spaces in figure 2.3 are therefore filled with those progressively smaller coated spheres.

2.4.3 Three-Point Bounds

The Three-Point Bounds (abbr. 3PB) [18] are tighter bounds than the Hashin-Shtrikman ones. Accordingly, they require additional information on the microgeometry.

First derived by Beran and Molyneux [1] these bounds use information on the statistics of the phase arrangement in the form of two three-point microstructural parameters, $\eta(\xi_p)$ and $\zeta(\xi_p)$ [3]. In this thesis two different sets of statistical parameters for identical impeneterable spheres are used. The first set consists of the $\zeta(\xi_p)$ derived by Miller and Torquato [18] and the $\eta(\xi_p)$ by Torquato et al. [28]. In terms of this thesis this set is called "Miller parameters". The second set of parameters was recently evaluated by Gillman et al. [9]. The statistical parameter $\zeta(\xi_p)$ is restricted to the closed interval $[0, 1]$ [29]. For the extreme case of $\zeta(\xi_p) = 0$ the three-point bound becomes the lower Hashin-Shtrikman bound [26], and for $\zeta(\xi_p) = 1$ the upper Hashin-Shtrikman bound.

For engineers the Young's modulus and the Poisson's ratio tend to be more important than the shear and bulk moduli because they are comparable to the uniaxial tensile test results. Nevertheless, in terms of calculating material properties, it is usually preferable to evaluate the bulk and shear moduli because they directly correspond to the purely hydrostatic and purely deviatoric load cases. In [1] one can find the three-point bounds for the bulk and shear moduli.

2.4.4 Torquato's Third Order Estimates

Torquato's Third Order Estimates (abbr. 3OE) alias "weak contrast expansion estimates"[27] also rely on the three-point statistical parameters for describing a given microstructure. They always lie between the three-point bounds and can be directly compared to predictions from numerical studies. In figure 2.4 a comparison between the Hill bounds, the Hashin-Shtrikman bounds, the three-point bounds and the third-order estimates is given for particle volume fractions up to $\xi_p = 0.6$, the material parameters used for for the constitutes being provided in table 2.1. The phase geometry consists of identical, randomly positioned, spherical particles embedded in the matrix, the statistical parameters of Miller et al. [18][28] are used. As one can see, the third order estimates are positioned closer to the lower bounds and lie within

Table 2.1: Fictitious material properties used for the comparison

Matrix properties		**Particle properties**	
E_{m}	ν_{m}	E_{p}	ν_{p}
1	0.3	10	0.1

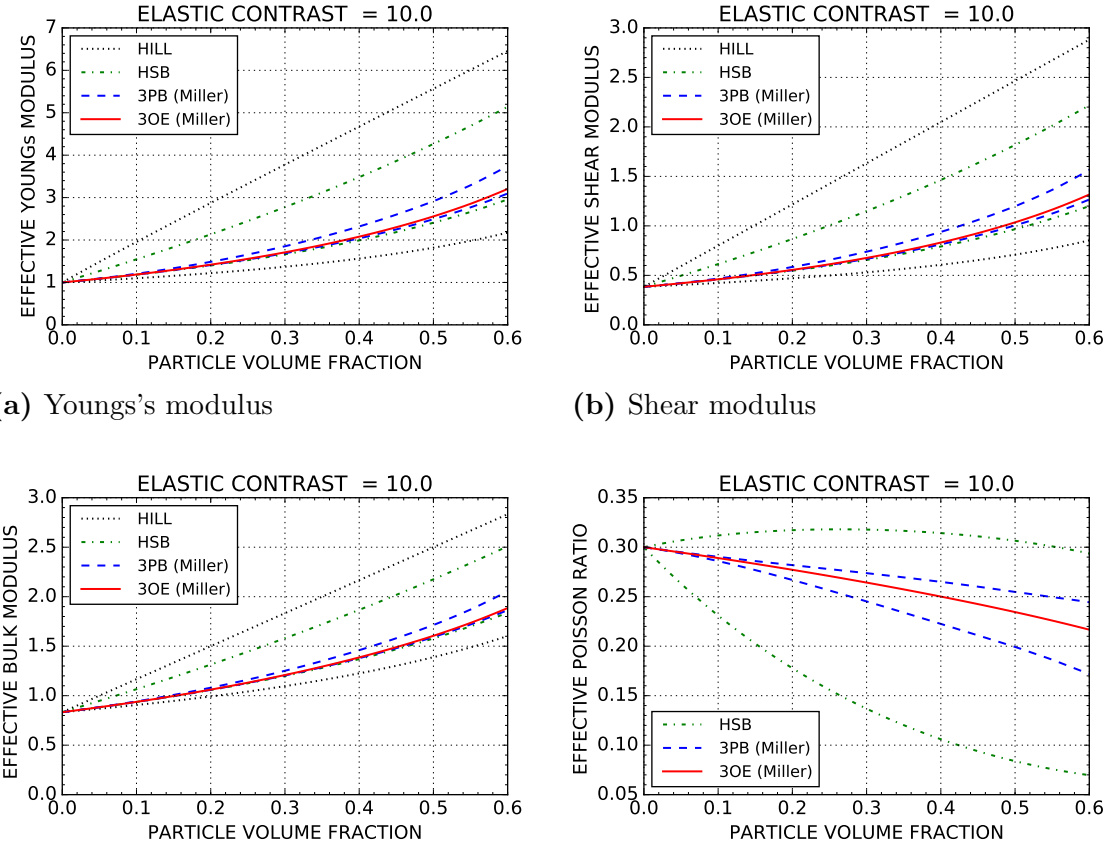

(a) Youngs's modulus

(b) Shear modulus

(c) Bulk modulus

(d) Poisson's ratio

Figure 2.4: Comparison of three-point bounds, Hill bounds, Hashin-Shtrikman bounds and Torquato's third order estimates for the material parameters from table 2.1, the three-point parameters of Miller et al. [18][28] corresponding to identical, random positioned spheres being used.

the three-point bounds, which, in turn, are inside the Hashin-Shtrikman bounds and the slacker Hill bounds

2.4.5 Statistical Parameters

As mentioned for the three-point bounds, section 2.4.3, and the third order estimates, section 2.4.4, different sets of statistical parameters can be used for describing different microstructures. For this thesis statistical parameters for impenetrable identical spheres in a three-dimensional random arrangement taken from the literature are used. Evaluating these parameters requires a major computational effort.
Two sets of statistical parameters are used in the following analysis. The most recent statistical parameters for impenetrable identical spheres were derived by Gillman et al. [9]. The statistical parameters by Gillman et al. interestingly provide slacker bounds at higher volume fractions compared to those derived Miller and Torquato [18][28]. A comparison indicates that the difference in the three-point bounds evaluated with the two parameter sets becomes visible at particle volume fractions in excess of $\xi_p = 0.4$. This behaviour can be seen in figure 2.5 a-c. The bounds for the Poisson's ratio, evaluated by using the parameters of Gillman et al. and Zimmerman's method [31], widen up with rising particle volume fraction, see figure 2.5 d. Due to the lack of statistical parameters for particle volume fractions beyond $\xi_p = 0.6$ the comparison ceases there.

2.4.6 Dependence on Elastic Contrast

In this section the behaviour of the various bounds with different elastic contrasts is discussed. Figure 2.4 presents a number of bounds evaluated for an elastic contrast of $c_{el} = 10$. In figures 2.6 to 2.9 the same bounds are shown for an elastic contrast of $c_{el} = 100$, $c_{el} = 0.1$ and an elastic contrast of $c_{el} = 0.01$, respectively. The Poisson's ratios are chosen the same as defined in table 2.1. As one can see in figure 2.6, with a higher elastic contrast the lower Hashin-Shtrikman and the lower three-point bound start with a smaller gradient, resulting in slacker bounds. The third-order estimates tend to stay close to the lower bounds, a behaviour typical for composites of stiff particles in a compliant matrix. This can be seen in figure 2.7 in the enlarged region.

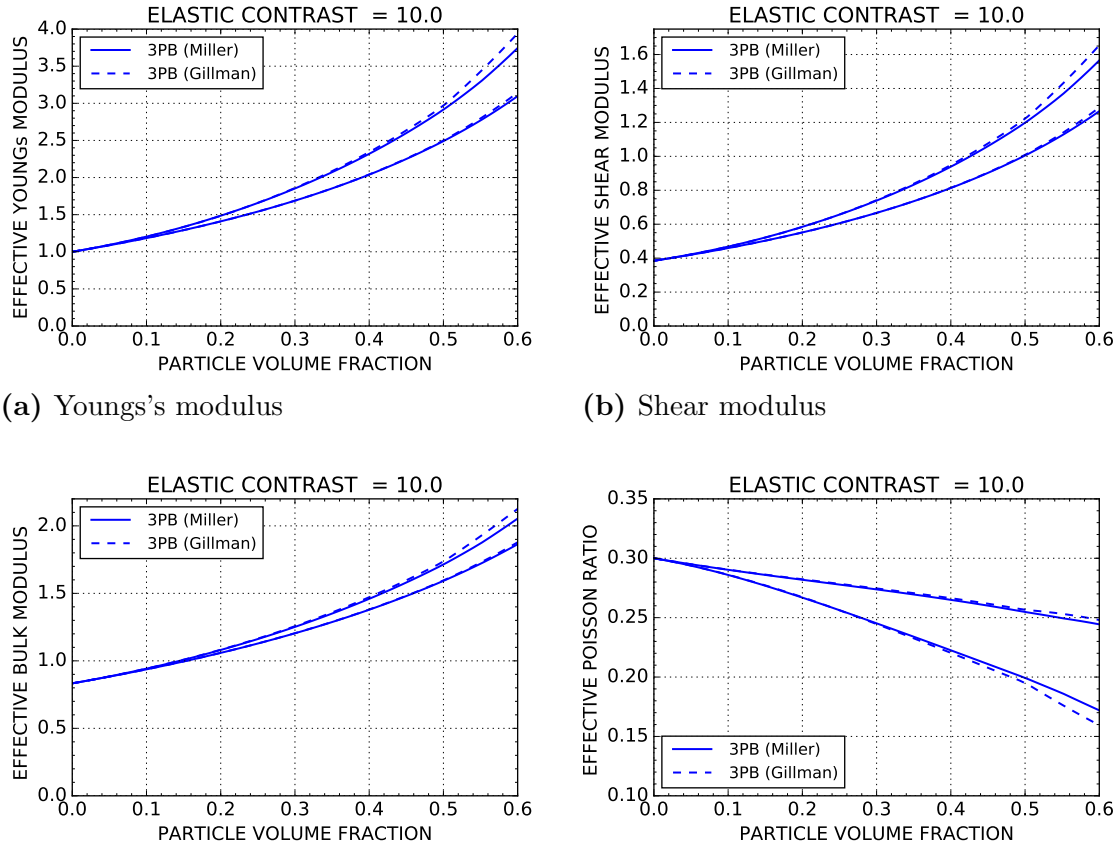

(a) Youngs's modulus **(b)** Shear modulus

(c) Bulk modulus **(d)** Poisson's ratio

Figure 2.5: Comparison of three-point bounds evaluated with different statistical parameters

An elastic contrast lower than unity, i.e. particles that are more compliant than the matrix, is explored in figures 2.8 and 2.9. For the bounds in figure 2.8 an elastic contrast of $c_{\mathrm{el}} = 0.1$ was selected. For this configuration the three-point bounds are rather sharp and the third-order estimate is closer to the upper bound as one can see in the diagrams. The Hashin-Shtrikman bounds show a slackness compared to that obtained for an elastic contrast of $c_{\mathrm{el}} = 10$. The slopes of the curves are reversed, as expected. One can see for an elastic contrast of $c_{\mathrm{el}} = 0.01$ in figure 2.9 that the three-point bounds become slack again. The third-order estimate is closer to the upper bound as well.

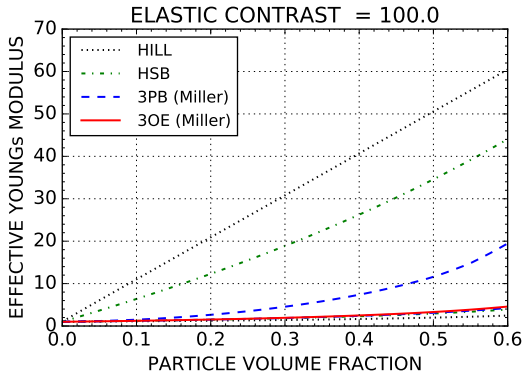

(a) Youngs's modulus

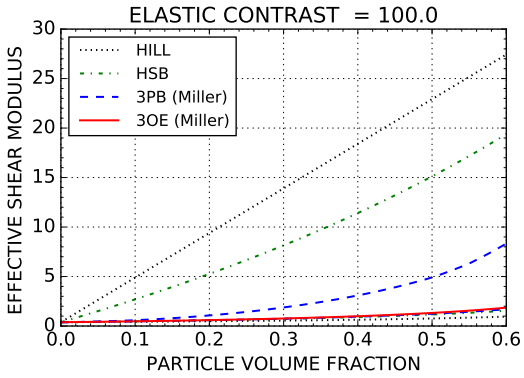

(b) Shear modulus

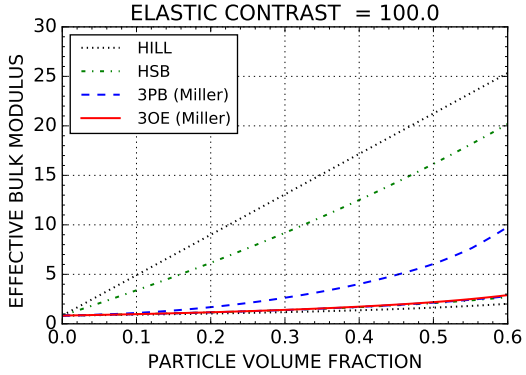

(c) Bulk modulus

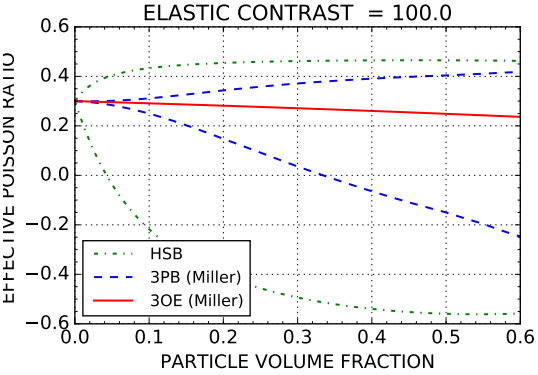

(d) Poisson's ratio

Figure 2.6: Comparison of three-point bounds, Hill bounds, Hashin-Shtrikman bounds and Torquato's third order estimates for the statistical parameters evaluated by Miller and Torquato [18][28] for an elastic contrast $c_{\mathrm{el}} = 100$

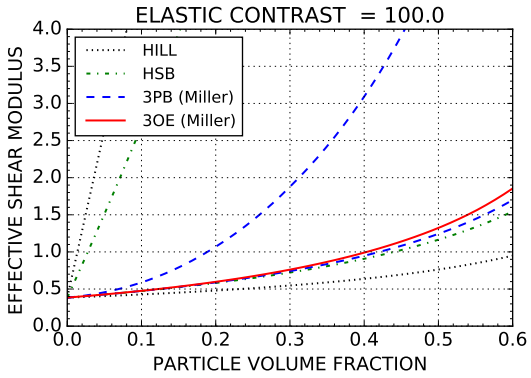

(a) Shear modulus

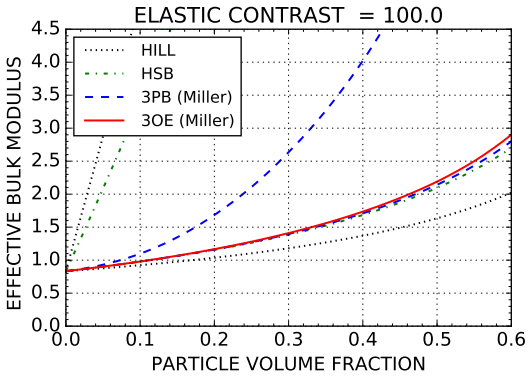

(b) Bulk modulus

Figure 2.7: Detail of the lower bounds for a high elastic contrast of $c_{\mathrm{el}} = 100$

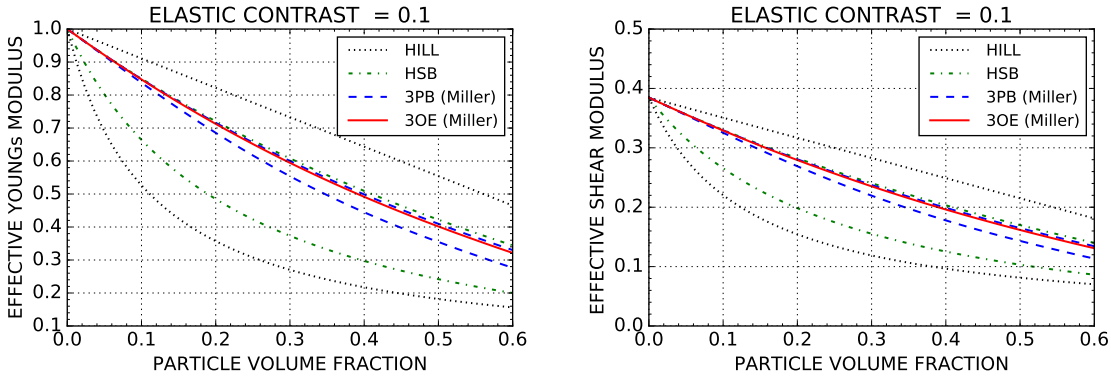

(a) Youngs's modulus

(b) Shear modulus

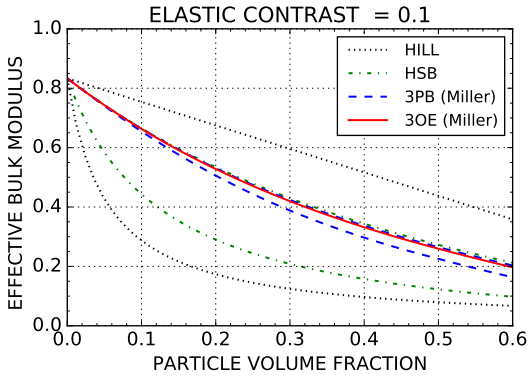

(c) Bulk modulus

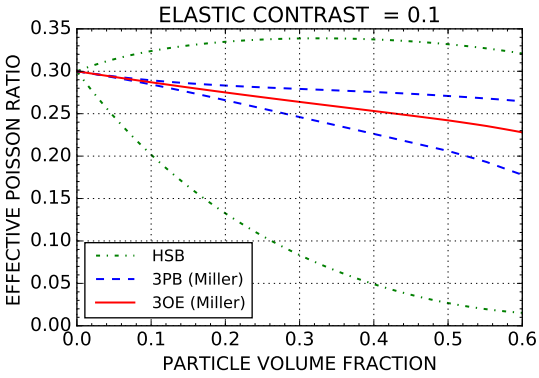

(d) Poisson's ratio

Figure 2.8: Comparison of three-point bounds, Hill bounds, Hashin-Shtrikman bounds and Torquato's third order estimates for the statistical parameters evaluated by Miller and Torquato [18][28] for an elastic contrast $c_{\mathrm{el}} = 0.1$

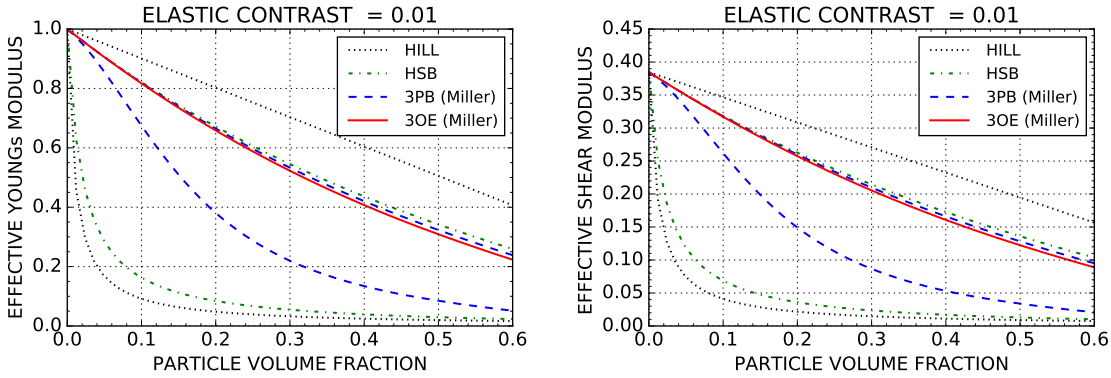

(a) Youngs's modulus

(b) Shear modulus

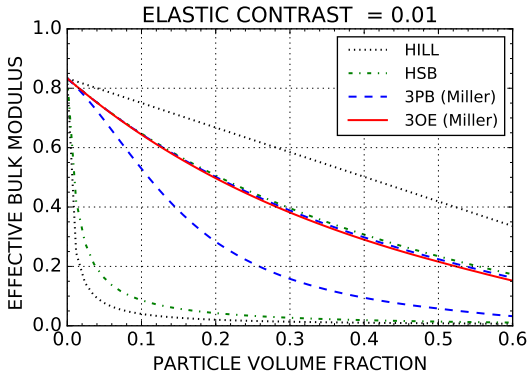

(c) Bulk modulus

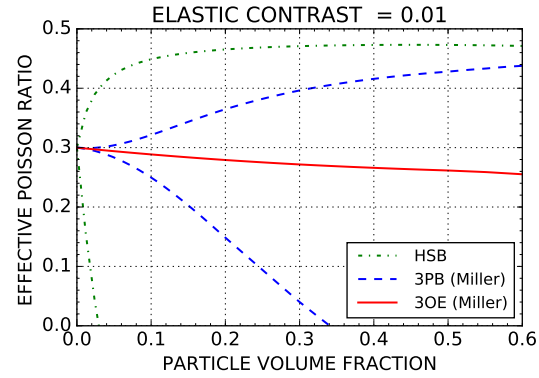

(d) Poisson's ratio

Figure 2.9: Comparison of three-point bounds, Hill bounds, Hashin-Shtrikman bounds and Torquato's third order estimates for the statistical parameters evaluated by Miller and Torquato [18][28] for an elastic contrast $c_{\text{el}} = 0.01$

2.5 Periodic Microfield Approaches

In contrast to bounding and mean-field methods, periodic microfield approaches are based on studying discrete microgeometries.
The basic assumption is that actual microgeometries can be well described by periodic phase arrangements. The latter can be studied by evaluating the behaviour of a single, periodic volume element or unit cell. Mechanical loads are applied to the resulting infinite models and the specific responses can be studied. The information obtained this way can be used to compute the effective material properties of the periodic phase arrangement. Instead of studying one very large volume element that closely approaches being a representative volume element (abbr. RVE), see section 2.5.1, one can study a series of different, smaller statistical volume elements (abbr. SVEs), see section 2.5.2, and evaluate the ensemble average of their responses.

2.5.1 Representative Volume Element

The representative volume element represents, in a statistical sense, the actual microstructure of a given composite. As a consequence an RVE also truly represents the material properties of statistically homogeneous materials. For this aspect an RVE must be sufficiently large to provide full information on the microstructure, but it must, of course, be small enough that the influences of macroscopic gradients can be neglected [3].

2.5.2 Statistical Volume Element

It has been found difficult to prove that given volume elements are actually RVEs. As a consequence, statistical volume elements [23] have been introduced. This term describes volume elements the size of which is insufficient to be a proper RVE. Using a number of SVEs with different geometries but following the same arrangement statistics and having the same particle volume fractions plus ensemble averaging, see

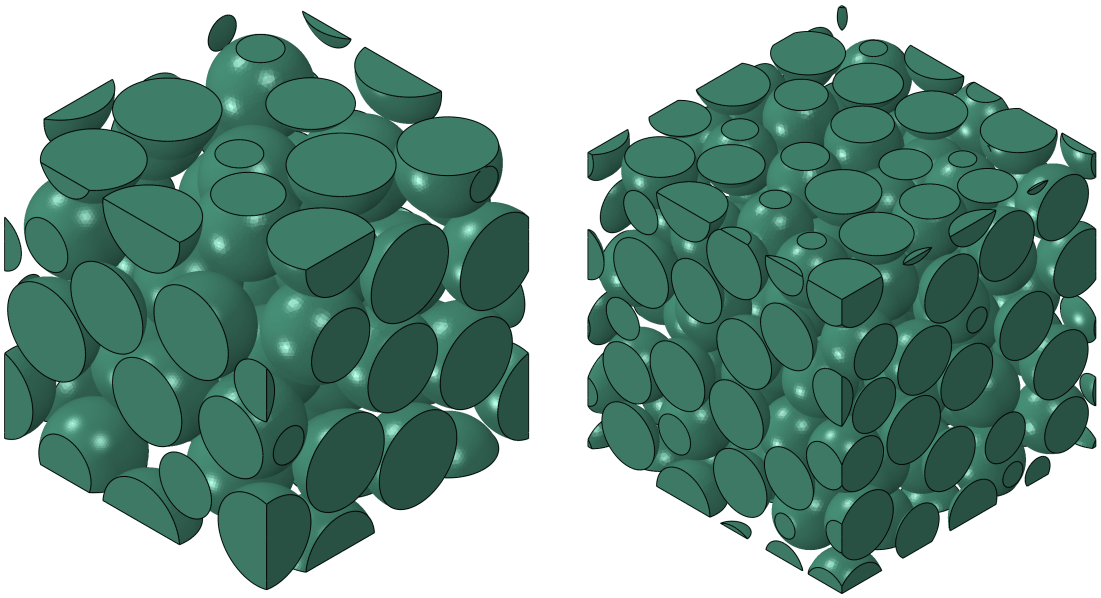

(a) 40 particles **(b)** 105 particles

Figure 2.10: Periodic statistical volume elements used in this thesis, of a particle volume fraction of $\xi_p = 0.55$ but containing different numbers of particles.

Section 2.5.4, is an appropriate way to approximate the effective material properties of a particle reinforced composite [24]. Figure 2.10 shows two different periodic SVEs used in this thesis. They have the same particle volume fraction of $\xi_p = 0.55$ but different numbers of particles.

2.5.3 Boundary Conditions

To extend a given unit cell appropriate boundary condition must be applied. These boundary conditions can describe translational periodicity, symmetry and antisymmetry (point-symmetriy) [3]. In figure 2.11 one can see a variety of possible unit cells for a periodic arrangement of circles embedded in a matrix. It may be noted that periodic arrangements can be subjected to either non-periodic or periodic boundary conditions.

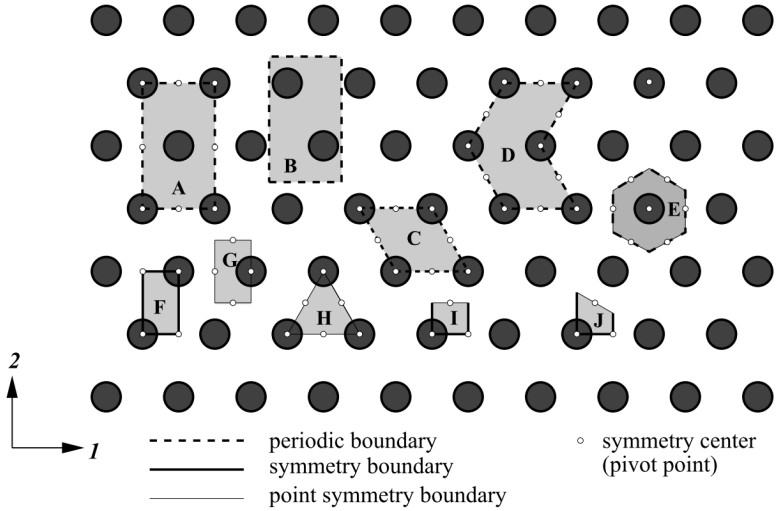

Figure 2.11: Periodic arrangement of particles with a variety of possible unit cells with different boundaries [3]

2.5.4 Ensemble Averaging

Evaluating the responses of an appropriate number of statistically equivalent SVEs and using ensemble averaging to obtain the effective moduli has been proven useful by Kanit et al. [15] as well as Rasool and Böhm [24]. The ensemble average represents the arithmetic mean of the given samples, wherein the samples are functions of the possible states of the underlying statistics.

2.5.5 Closest Isotropic Tensor

In general, even an ensemble average of a number of SVEs consisting of an isotropic matrix and randomly positioned isotropic particles will not be completely isotropic. Therefore, it is often worthwhile to find the closest isotropic tensor to the ensemble averaged one in order to obtain isotropic elastic material properties. There are a number of ways to achieve this. In this work the closest isotropic tensor will be found by optimization based on the log-Euclidean distance. To use the log-Euclidean distance ensures obtaining the same closest isotropic tensor no matter if the compliance

or stiffness tensor is used [21]. This is due the fact that the log-Euclidean distance is not influenced by the inversion of elasticity-like tensors.

2.6 Microgeometries

To obtain realistic material properties approaching isotropy, samples of sufficient size with random microgeometries are needed. This can be achieved in two different ways. The first is to create microgeometries which are based on real microstructure information gained from experiments. The second method, and the one chosen in this work, is to create synthetic random arrangements of particles.
There are various approaches to generating such random arrangements. The one which will be used in this work is random sequential adsorption, which is introduced in Section 2.6.1.

2.6.1 Random Sequential Adsorption

One of the most common methods for creating random matrix-inclusion geometries, for example randomly positioned impenetrable spheres, are random sequential adsorption algorithms (abbr. RSA). Spheres are placed randomly in the volume element. If a test sphere penetrates another, previously accepted sphere or is placed within a certain minimum distance to said sphere, it will be rejected and the algorithm starts placing another sphere. This procedure is continued till the desired volume fraction of spheres is reached or no further spheres can be placed in the volume element. The latter difficulty, referred to as jamming, is taken to occur if the placement of a new sphere fails within a finite number of tries ("geometric frustration") [3]. The volume fraction which can be achieved for periodic arrangements of identical spheres with the RSA method lies in-between 30% to 35%.
It must be mentioned that periodicity as well as the minimum distance between spheres and the minimum distance to the face of the box which are used by the al-

gorithm restrict the comparability to the bounds and the estimates. This is because the bounds are based on a hardcore distribution, where spheres can touch each other, whereas the RSA algorithm chosen here is based on a penetrable-concentric-shell model [27] to improve meshability, see section 3.2.1. The difference can be seen in figure 2.12.

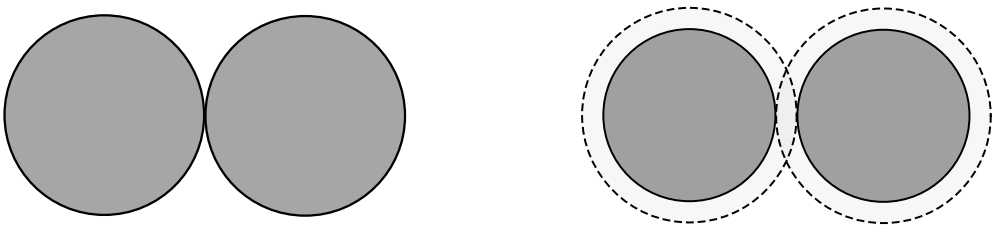

(a) Hardcore distribution **(b)** "Cherry pit" model

Figure 2.12: Comparison of the penetrable-concentric-shell model alias "cherry pit" [27] and the hardcore distribution of identical spheres.

Closer Packings

To obtain closer packings other methods must be used. In this thesis the in-house program *Arigen* was used for this purpose. The algorithm to create packings beyond the jamming limit of the RSA method consists a number of "pseudo-repulsive-force based vectorial shifting compression" [2] steps. In this thesis 50 to 200 steps were applied to create the packings with particle volume fractions up to $\xi_p = 0.6$.
The closest packing which would be possible for identical spheres is a hexagonal or cubic close packing with a packing density of $\xi_p = 0.74048$ [6]. However, such packings cannot be considered as random any more because they follow a lattice model.

Chapter 3

Modelling

In this section the knowledge from section 2 is used to set up and postprocess a number of analyses to obtain the effective material properties of an elastic isotropic matrix reinforced with elastic isotropic spherical particles.
The program *Digimat* (e-Xstream, Luxembourg, and MSC Software, Newport Beach, 2017), which was used to generate most microgeometries and the meshes, has an interactive workflow which operates through different input pages.

3.1 Define Phase Properties

The phase properties, such as the geometric shape, the size of a particle as well as the elastic isotropic material properties of the matrix and particles, are defined in separate input pages ("tabs"). For the material properties each Poisson's ratio and Young's modulus are input parameters. The particle size is calculated from the size of the volume element, the number of particles and the desired particle volume fraction. Cube-shaped SVE of edge length 1 were used throughout. Because spherical particles are used as inhomogeneities there is no need to define orientations.

3.2 Generation of Microgeometries

For this work two programs were used to produce the SVEs. For particle volume fractions lower than $\xi_p = 0.3$ the random sequential adsorption algorithm integrated in Digimat was used. Its usage is described in section 3.2.1. Due to the jamming limit of the RSA method higher particle volume fractions where generated with the ILSB in-house program Arigen, see section 3.2.2. Both options can generate periodic arrangements.

3.2.1 Digimat

As mentioned above, Digimat was used for generating volume elements with particle volume fractions up to $\xi_p = 0.3$. In addition to the particle volume fraction the minimum distance between neighbouring particles as well as the minimum distance from a given particles to the box, i.e., the edges of the SVE, must be selected.
These input parameters must be chosen in balance with the meshability of the generated SVE and they must allow a proper comparison with the bounds. If the minimum distances are too small, problems with unsatisfactory meshing can occur. Particles which are too close together may produce an ill-conditioned stiffness matrix. This is due the fact that the elements tend to be unfavourably shaped in small gaps. On the other hand, if the minimum distances are too big, the statistics of the phase geometry may differ too strongly from the hardcore models underlying the three-point parameters, see figure 2.12.

3.2.2 Arigen

Arigen is an ILSB in-house code for creating periodic or non-periodic microgeometries with high volume fractions of spherical particles or aligned cylindrical fibres. For this thesis it was used to generate three-dimensional unit cells with identical impenetrable spheres. The program follows two steps. In the first step, volume elements

with particle volume fractions of $\xi_p = 0.33$ were generated by a random sequential adsorption algorithm. In the second stage 50 to 200 "compression steps" are used to reach higher particle volume fraction. This method is used to create SVEs with up to $\xi_p = 0.6$. To reach particle volume fractions exceeding, say, $\xi_p = 0.55$, smaller inter-particle and particle-wall distances must be selected and computing times may be rather high.
The results of Arigen are imported into a spreadsheet program. The positions and sizes of the spheres were then passed on to Digimat for visualization and integration into the workflow.

3.3 Meshing

The meshing of the generated geometries is done with the built-in Digimat mesher. Some meshing parameters are available to influence the mesh quality and the total number of degrees of freedom (abbr. DOF). There are options for generating smooth or voxel meshes.

3.3.1 Smooth Meshes

The main element type used in smooth meshes is isoparametric, quadratic, 10-node tetrahedral elements with full integration. Some analyses were also done with linear 4-node tetrahedral elements, which are known to have sub-optimum convergence properties. The meshes which are based on tetrahedra are called smooth meshes. An appropriate element size is used which is fine enough to represent the geometry and is still in balance with the computation time. Digimat offers some tools for improving the mesh efficiency. Two options discussed here are "internal coarsening" and "curvature control". Internal coarsening enlarges elements which are far away from a phase boundary, see [19], p.521, thereby reducing the number of elements and, consequently, the number of degrees of freedom and improving the efficiency. This

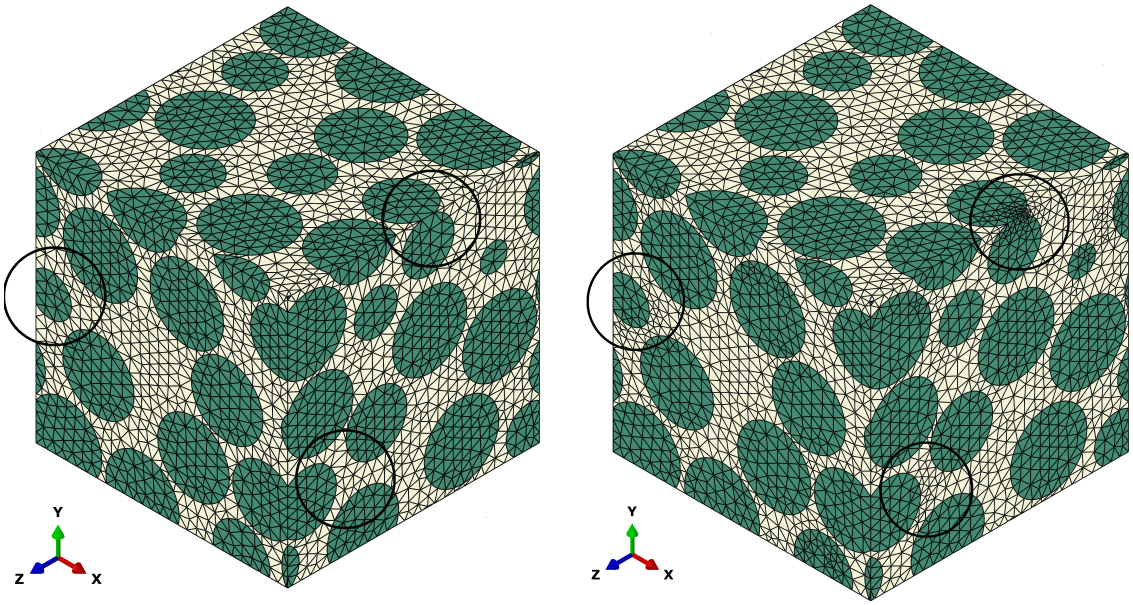

(a) without curvature control

(b) curvature control set to 0.1

Figure 3.1: Influence of curvature control on the mesh discretization of an SVE with 40 particles and $\xi_p = 0.55$. Pertinent regions are marked for comparison.

option was chosen for all analyses. The curvature control option allows to improve the discretization of curved surfaces. The influence of curvature control can be seen in figure 3.1. One undesirable effect which was found using curvature control is that it may produce non-conforming meshes on opposite faces of the SVE, see figure 3.2. Non-conforming meshes tend to produce nodes without a partner on the opposite face, which, in turn, may give rise to unphysical perturbations in local stresses, compare figure 3.3. Even though such errors tend to have minimal influence on the predicted macroscopic responses, such meshes are clearly problematic in the context of periodic homogenization.

Furthermore, it is difficult for the user to predict where curvature control will refine the mesh. Accordingly, curvature control was not applied for the analyses in this thesis. There is also the option to generate meshes where the interfaces are modelled with separate nodes. This means that each phase has its own node at the interface at the same position. This feature can be used for non-linear models of interfaces

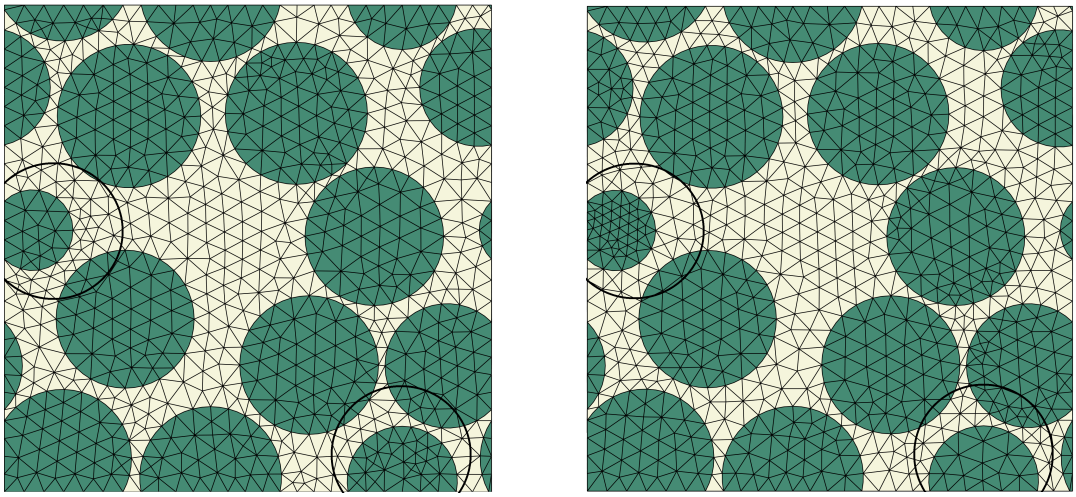

(a) Positive $x - y$ face **(b)** Negative $x - y$ face

Figure 3.2: Opposite faces of a volume element with 40 particles and $\xi_p = 0.55$, meshed with curvature control. Some regions with incompatible meshes are marked for comparison.

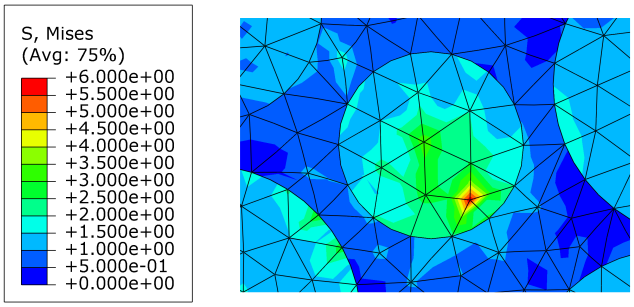

Figure 3.3: Detail of an outer face of a model showing particles intersected by the box. The Von Mises stress distribution shows a local peak due to an "unconnected" node caused by incompatible meshing.

and separation. Because these are not part of this thesis the interfaces are modelled with shared nodes.

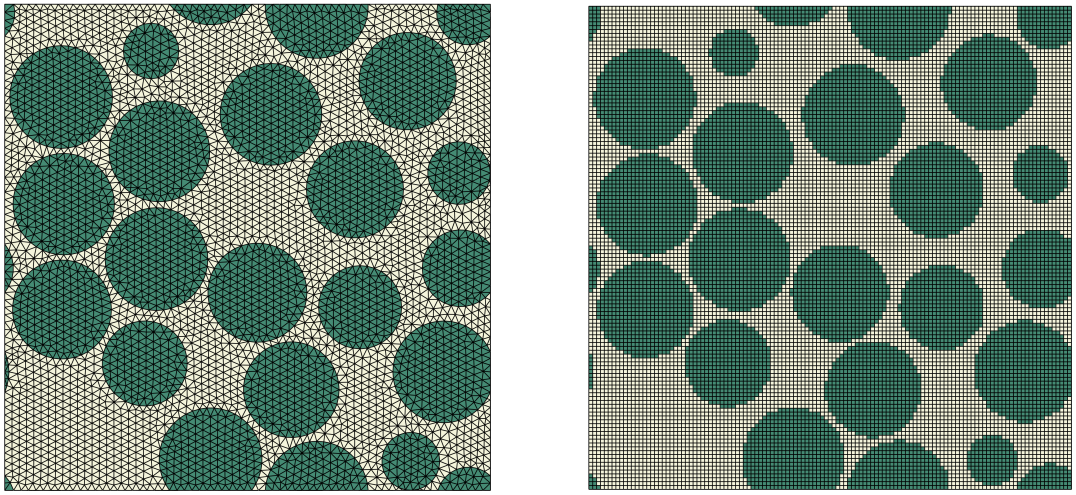

(a) Smooth mesh **(b)** Voxel mesh

Figure 3.4: Comparison of the same microgeometry discretized by smooth and voxel meshes, respectively. The meshing parameters are the same as used in this thesis.

3.3.2 Voxel Meshes

At a first look, it does not seem to make sense to take an exact digital geometry and generate a voxel based mesh from it. Voxel based meshes are more usually generated from computed tomography or magnetic resonance imaging scans [4], where they provide three-dimensional visualisations and are predestined for generating meshes made of voxels.

The main advantage of voxel meshes in the present setting is their simplicity. Compared to smooth meshes one can give the exact number of elements to be generated in a voxel mesh a priori. This is due to the fact that voxel meshes are built as a fixed array with n_{vox}^3 elements, where n_{vox} is the number of hexahedron elements in each direction. In figure 3.4 one can see a comparison of the same microgeometry discretized with the two types of mesh such that comparable numbers of degrees of freedom result. Although voxel meshes tend to require more degrees of freedom for obtaining a discretisation of a spatial resolution that is comparable to that of smooth meshes the computational effort to generate the mesh and solve the system is smaller

Table 3.1: Effective volume fraction of the actual geometry in comparison with the volume fraction of smooth and voxel meshes. The deviations are given in %, normalized in respect to the actual geometry.

		Effective Volume Fraction			Deviation	
No.	Phase	Smooth	Voxel	Geometry	ΔSmooth	ΔVoxel
1	Particles	0.549938	0.550063	0.549996	-0.0105	0.0122
	Matrix	0.450062	0.449937	0.450004	0.0129	-0.0149
2	Particles	0.549932	0.550060	0.549997	-0.0118	0.0115
	Matrix	0.450068	0.449940	0.449986	0.0182	-0.0102
3	Particles	0.549939	0.550082	0.549995	-0.0102	0.0158
	Matrix	0.450061	0.449918	0.450014	0.0104	-0.0213
4	Particles	0.549938	0.550049	0.550000	-0.0113	0.0089
	Matrix	0.450062	0.449951	0.450010	0.0116	-0.0131
5	Particles	0.549938	0.550056	0.549998	-0.0109	0.0105
	Matrix	0.450062	0.449944	0.450019	0.0096	-0.0167

[30]. Voxel meshes also have the advantage of a better conditioned stiffness matrix because for two-phase composites only two different stiffness entries exist and that there are no issues with mesh periodicity.

In the first step of generating the voxel mesh a regular, structured mesh of identical, cube shaped elements is built. The voxel-elements are then assigned the material properties of the phase which occupies the center of the voxel, see [19], p.522. Therefore, for glancing intersections of spheres the original geometries tend to become disturbed depending on the size of the elements. One can see in figure 3.5 that the diameter of glacing intersections of spheres appears bigger on a voxel based mesh. With finer discretization the original geometry is better represented.

Upon explicit checking the voxel models were found to accurately correspond to the prescribed phase volume fractions. This can be seen in table 3.1. The percentage deviation between the different meshes and the actual geometry is almost always below 0.02%. The voxel meshes tend to have minimally higher particle volume fractions compared to the actual geometry.

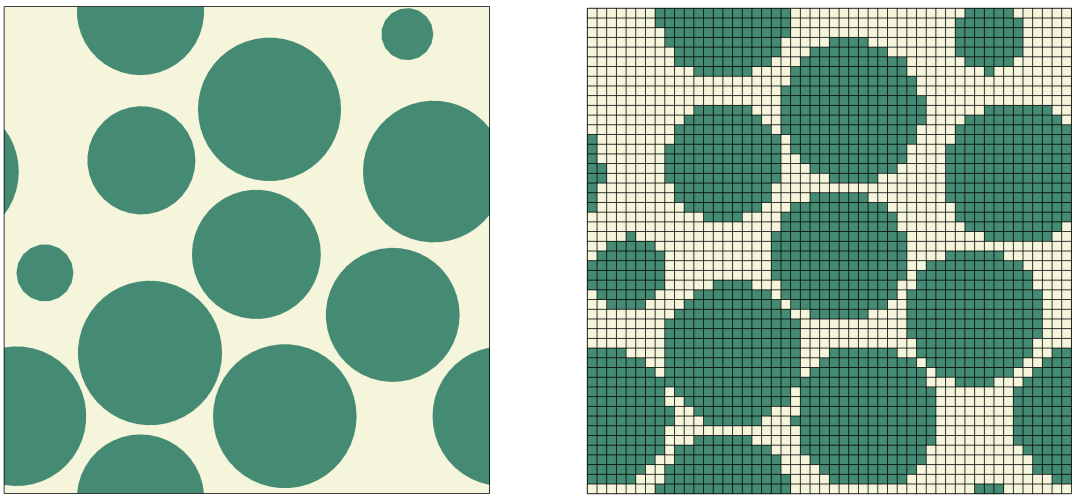

(a) Original microgeometry **(b)** Badly discretized voxel mesh

Figure 3.5: Example of a badly discretized mesh in which some of the voxels pertaining to different particles, effectively introducing non-spherical "super-inclusions" into the model. Also notable are effects of glancing intersections of spheres with the box, the resulting circles showing considerable changes to their radii.

Complications with Voxel Meshes

Using voxel based meshes can lead to issues with the discretization. If the diagonal of a voxel is bigger than the minimum distance between two particles, changes of topology may occur, an issue illustrated in figure 3.5. One can see that the discretization of this sample is so bad that some particles become connected. Even if the voxels touch only in one vertex, a larger "super-inclusion" is effectively generated within the finite element framework. This gives rise to volume elements that do not correspond to identical spherical particles, making them ill-suited for the present work.

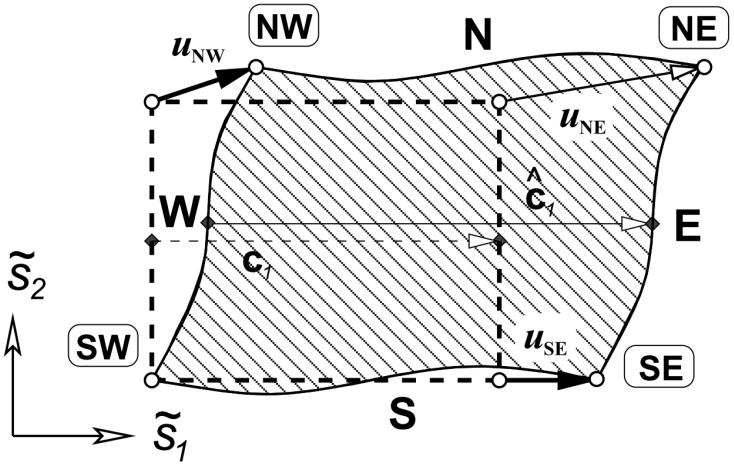

Figure 3.6: Illustration of a rectangular cell with periodic boundary conditions [3]

3.4 Boundary Conditions

For micromechanical finite element analysis appropriate boundary conditions must be applied, which ensure that the Mandel-Hill [16][12] conditions are fulfilled, i.e., that microscopic and macroscopic behaviour are energetically equivalent. One can choose between a number of different conditions [3]. In this thesis periodic boundary conditions were applied, a brief introduction to which is given here.

3.4.1 Periodic Boundary Condition

Periodic boundary condition are used to extend a finite volume element into an infinite periodic arrangement. They have been proven to provide fast convergence in terms of model size as well as allowing reduced SVE sizes [13]. For periodic boundary conditions the displacements of half of the faces of the volume element is fully controlled by the opposite face of the unit cell. For example, in figure 3.6 the face pairs W-E and N-S share the same fluctuations. A general expression for periodic boundary conditions for small strains is [3]

$$\boldsymbol{u}_k^+ - \boldsymbol{u}_k^- = \boldsymbol{u}(\boldsymbol{s}_k + \boldsymbol{c}_k) - \boldsymbol{u}(s_k) = \langle \boldsymbol{\varepsilon} \rangle * \boldsymbol{c}_k \tag{3.1}$$

wherein $\boldsymbol{u}_k^+$ and $\boldsymbol{u}_k^-$ are the displacements of the homologous points $\boldsymbol{s}_k$ and $\boldsymbol{s}_k + \boldsymbol{c}_k$. $\boldsymbol{c}_k$ is the linking vector which connects those points. Using the notation from figure 3.6 and applying equation (3.1) on a two-dimensional rectangular cell one can write [3]

$$\boldsymbol{u}_N(\tilde{s}_1) = \boldsymbol{u}_S(\tilde{s}_1) + \boldsymbol{u}_{NW}, \qquad \boldsymbol{u}_E(\tilde{s}_2) = \boldsymbol{u}_W(\tilde{s}_2) + \boldsymbol{u}_{SE} \tag{3.2}$$

Here $\tilde{s}_k$ denotes the local coordinates on a pair of faces. Therefore each pair of faces should be meshed with the same discretization.
Comparing equations (3.1) and (3.2) shows that the information of the macroscopic strain $\langle \boldsymbol{\varepsilon} \rangle$ is contained in the nodal displacements of the edge nodes SE and NW [3]. Every single deformed unit cell can be seen as a piece of a jigsaw puzzle which fits in perfectly with its neighbours. The approach described above can be applied to three-dimensional unit cells as well [17].

3.5 Exporting Input Data

To carry out an analysis with *Abaqus* (Dassault Systèmes, Vélizy-Villacoublay, 2016), the mesh created with Digimat has to be exported. This can be done automatically via a Digimat option. It creates an Abaqus .inp file. To obtain the material properties of the unit cell six different linear independent load cases have to be applied.

Modifying the Input

The input file generated by Digimat was modified such that load controlled instead of displacement controlled analyses were done. This has the advantage of allowing all six necessary analyses to be done as six steps in a single analysis. The modification was carried out by replacing the ∗STEP section of the Abaqus input file provided by Digimat. Then the file "StepDataDIT.inp" was imported. In this file the new loads are provided.

3.6 Solving

The six different load cases of the generated microgeometries are either computed with Digimat or Abaqus. The voxel based meshes are mainly computed with Abaqus due to the high number of degrees of freedom involved which make the parallelization capabilities and optional iterative solver of Abaqus especially valuable. The smooth meshes using quadratic tetrahedral elements were primarily analysed with Digimat. Results were found to be independent of the solver used.

3.7 Post-processing

Digimat can evaluate the material properties of a given microgeometry directly. There is only a need to ensemble average the output files. In contrast, more post-processing steps are necessary for analyses carried out with Abaqus. This is done with tools available from the Institute of Lightweight Design and Structural Biomechanics.

3.7.1 ILSB In-house Tools

There are suitable post-processing tools available at the Institute of Lightweight Design and Structural Biomechanics. The ones which are used in this thesis are explained below.

procDNdata

procDNdata is a tool for extracting information on master nodes and loads from the output database (abbr. odb) created by the analysis using the Python linking to the Abaqus output database. It is used by calling it in the shell and afterwards entering the output database's name to started the processing. procDNdata creates a .rne file.

etfrpt

The tool etfprt is used to extract the stiffness and compliance tensors from the .rne file created with procDNdata. The results are stored in an .out file.

avgelt

With avgelt a set of elastic tensors can be ensemble averaged. The purpose is to replace big analyses with a number of smaller ones to obtain a approximation to the macroscopically isotropic material behaviour. Avgelt reads a number of .out files and computes an .ave file which contains the ensemble averaged stiffness and compliance tensors. Due to numerical errors and inaccuracies due the limited number of particles in a given set of SVEs obtained with a finite number of analyses the tensor, in general, is not perfectly isotropic.

closelt

To improve the approximation of the isotropic effective material behaviour the ILSB in-house tool closelt is used. It computes the closest isotropic tensor to the approximately isotropic tensor provided by an .ave file. It can use different methods to do so. For this thesis the closest isotropic tensor using the log-Euclidean distance was used for the effective material behaviour. As an example equation (3.3) shows the

compliance tensor of a statistic volume element with a particle volume fraction of $\xi_\mathrm{p} = 0.55$ and 40 particles, which obviously shows some anisotropy.

$$\mathbf{C} = \begin{bmatrix} 0.3348943 & -0.0727037 & -0.0731641 & 0.0079077 & -0.0050045 & 0.0077936 \\ -0.0726824 & 0.3403466 & -0.0771278 & -0.0003539 & -0.0003791 & -0.0007849 \\ -0.0731539 & -0.0771646 & 0.3395461 & -0.0073117 & 0.0037889 & -0.0039859 \\ 0.0078925 & -0.0003436 & -0.0073263 & 0.8221935 & 0.0020122 & -0.0140192 \\ -0.0049982 & -0.0003620 & 0.0037847 & 0.0020300 & 0.8053628 & -0.0129824 \\ 0.0077822 & -0.0008082 & -0.0039911 & -0.0140271 & -0.0129741 & 0.8208980 \end{bmatrix} \tag{3.3}$$

The closest isotropic compliance tensor of the same statistic volume element obtaining via the log-Euclidean distance is

$$\mathbf{C}_\mathrm{isotrop} = \begin{bmatrix} 0.336367 & -0.073387 & -0.073387 & 0.000000 & 0.000000 & 0.000000 \\ -0.073387 & 0.336367 & -0.073387 & 0.000000 & 0.000000 & 0.000000 \\ -0.073387 & -0.073387 & 0.336367 & 0.000000 & 0.000000 & 0.000000 \\ 0.000000 & 0.000000 & 0.000000 & 0.819508 & 0.000000 & 0.000000 \\ 0.000000 & 0.000000 & 0.000000 & 0.000000 & 0.819508 & 0.000000 \\ 0.000000 & 0.000000 & 0.000000 & 0.000000 & 0.000000 & 0.819508 \end{bmatrix} \tag{3.4}$$

The isotropic engineering moduli can be obtained from this tensor using the relations

$$\begin{aligned} C_{11} = C_{22} = C_{33} = 0.336367 &= \frac{1}{E} \\ C_{12} = C_{13} = C_{23} = -0.073387 &= -\frac{\nu}{E} \\ C_{44} = C_{55} = C_{66} = 0.819508 &= \frac{1}{G} \\ K &= \frac{E}{2(1-2\nu)} \end{aligned} \tag{3.5}$$

resulting in

$$E = 2.97294, \qquad \nu = 0.218175, \qquad G = 1.22024, \qquad K = 1.75815 \tag{3.6}$$

Note that due to the linearity of the analyses discussed here, input and output data remain valid if multiplied by an arbitrary factor. For this reason, no units are given for the moduli.

Chapter 4

Results

4.1 Definition of the Main Analysis

The main aim of this thesis is to compare analytical bounds for composite materials, made of an elastic homogeneous matrix reinforced with elastic isotropic spherical particles, with the effective material properties extracted from discrete finite element models with the use of the periodic unit cell approach.

The statistical parameters needed for some of the bounds (for example the three-point bounds) are available only for particle volume fractions up to $\xi_p = 0.6$. Therefore volume elements were modelled up to that limit. A second limitation is that with the methods used it may take considerable computational effort to generate random microstructures with particle volume fractions higher than $\xi_p = 0.55$. Thus the main analysis covers a range of particle volume fractions from 0 to 0.55 with an increment of $\Delta\xi_p = 0.05$. Because the solution for $\xi_p = 0$ is trivial, modelling of the unit cells starts with $\xi_p = 0.05$. The "main analysis" pertains to an elastic contrast of $c_{el} = 10$. There are also analyses with $c_{el} = 100$ and $c_{el} = 0.1$, but these where done with a bigger increment $\Delta\xi_p = 0.1$, also starting at $\xi_p = 0.05$. Furthermore, both smooth and voxel meshes are used to check if there is a difference in the resulting effective material properties. The Poisson's ratios for the matrix, $\nu_m = 0.3$, and the particles,

Table 4.1: Input material properties for the different elastic contrasts which were computed in this thesis

Elastic contrast	**Matrix Parameter**		**Particle Parameter**	
c_{el}	E_{m}	ν_{m}	E_{p}	ν_{p}
10	1	0.3	10	0.1
100	1	0.3	100	0.1
0.1	1	0.3	0.1	0.1
0.01	1	0.3	0.01	0.1

$\nu_{\mathrm{p}} = 0.1$, are the same in all analyses. All the input material properties of the main analysis are summarized in table 4.1. The number of particles was set to 40 for the main analyses. Nevertheless there were also analyses with a higher number of particles, see section 4.4

In total 55 microgeometries were generated for the main analysis. The edge length of the SVEs was always set to 1 to perform comparable meshing on the unit cells. To ensure successful meshing and to avoid numerical difficulties there was a prescribed minimum distance between neighbouring particles, see figure 2.12. This distance was set to 0.01 of the particle diameter. For some analyses covering higher volume fractions and increased numbers of particles this distance was reduced, more on this in section 4.4.

4.2 Comparison of Numerical and Analytical Solutions

The main comparison between the numerical and analytical solutions employs the input parameters defined in section 4.1. In sum, the effective material properties achieved with smooth meshes using tetrahedral elements are compared with the Hashin-Shtrikman bounds, the three-point bounds and the third-order estimates up

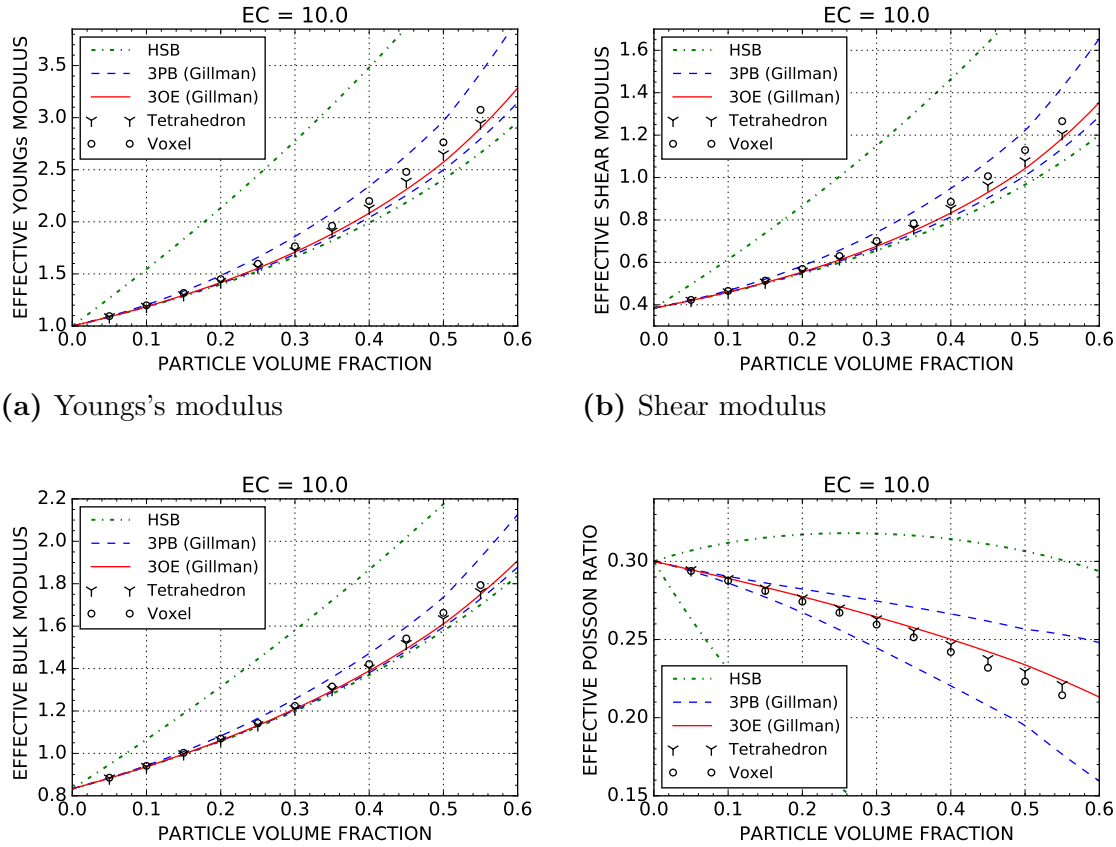

(a) Youngs's modulus

(b) Shear modulus

(c) Bulk modulus

(d) Poisson's ratio

Figure 4.1: Effective material properties predicted with smooth and voxel meshes in comparison with various bounds and estimates for an elastic contrast of $c_{\mathrm{el}} = 10$.

to a particle volume fraction of $\xi_{\mathrm{p}} = 0.55$. The results of these analyses can be found in figure 4.1. The statistical parameters derived by Gillman et al. are used for the three-point bounds and the third-order estimates, compare figure 2.4. Enlarged versions of the diagrams including different statistical parameters can be found in the appendix A.1 on page 71.

All the effective moduli computed with the smooth meshes are within the three-point bounds and therefore between the Hashin-Shtrikman bounds as well. The values computed are located near the lower bounds and close to the third-order estimates. With increasing particle volume fraction the difference between the computed values

and the third-order estimates tend to increase to some extent. However, at a particle volume fraction of $\xi_p = 0.55$ the two values approached each other again. To some extent this can be attributed to the statistical parameters of Gillman et al. which provide stiffer estimates at particle volume fractions exceeding $\xi_p = 0.5$, see figure 2.4.

Figure 4.2 shows one of the undeformed SVEs used in this thesis. It contains 40 particles at a particle volume fraction $\xi_p = 0.55$. Six different linear independent load cases were used to predict the effective material properties. The deformed stress fringe plots for these load cases can be found in figures 4.3 - 4.8. The loading directions correlate with the given coordinate system.

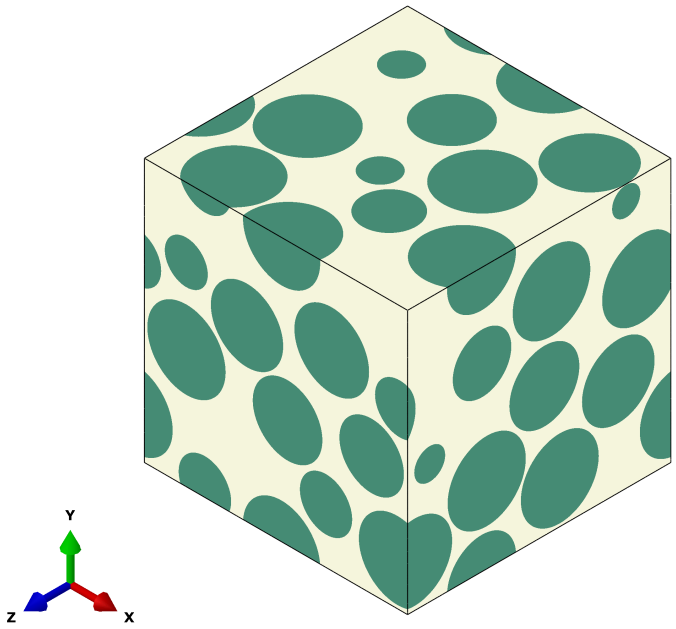

Figure 4.2: Undeformed SVE used in this thesis containing 40 particles at a particle volume fraction $\xi_p = 0.55$. The elastic contrast was $c_{el} = 10$.

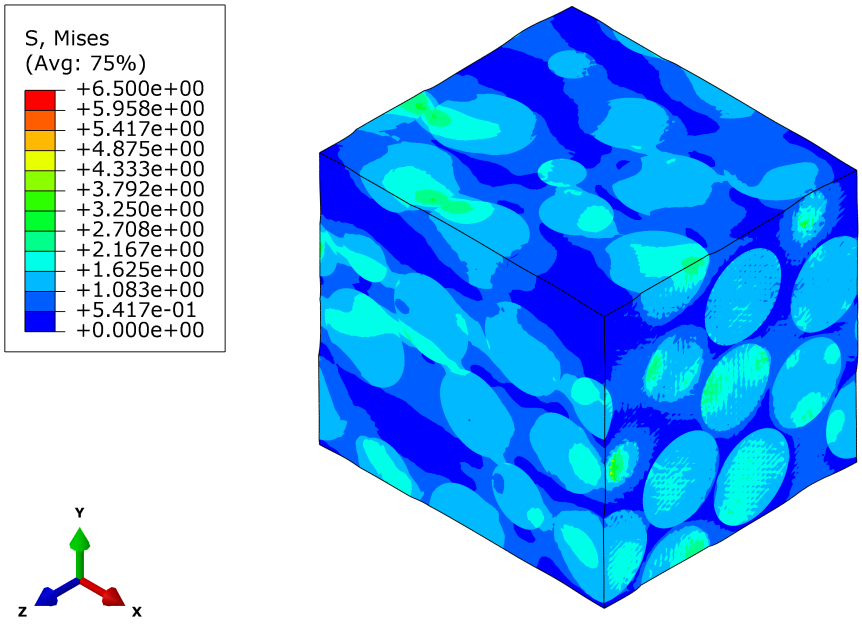

Figure 4.3: Resulting deformed shape of the SVE and predicted distribution of effective stress for an unidirectional load in x direction. ($\xi_p = 0.55$, $c_{el} = 10$, 40 particles)

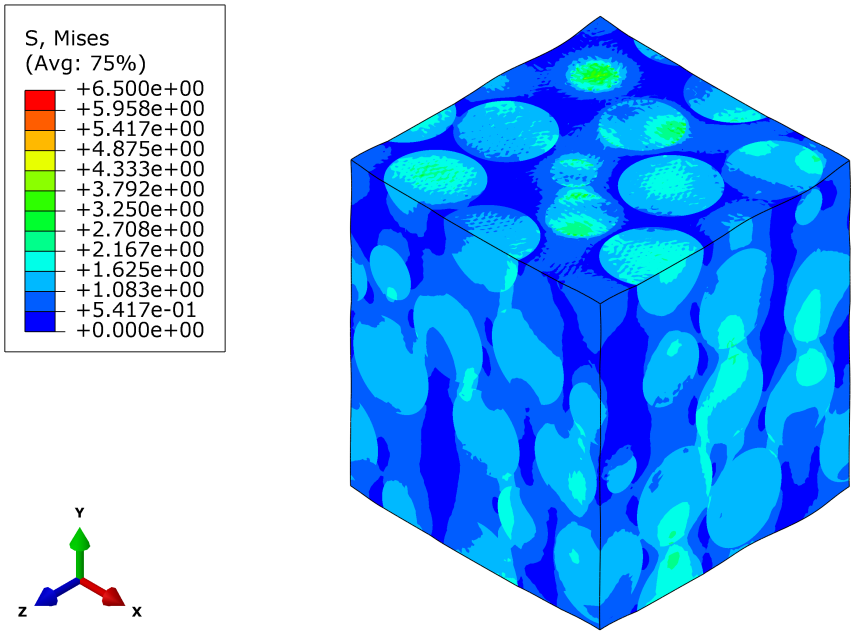

Figure 4.4: Resulting deformed shape of the SVE and predicted distribution of effective stress for an unidirectional load in y direction. ($\xi_p = 0.55$, $c_{el} = 10$, 40 particles)

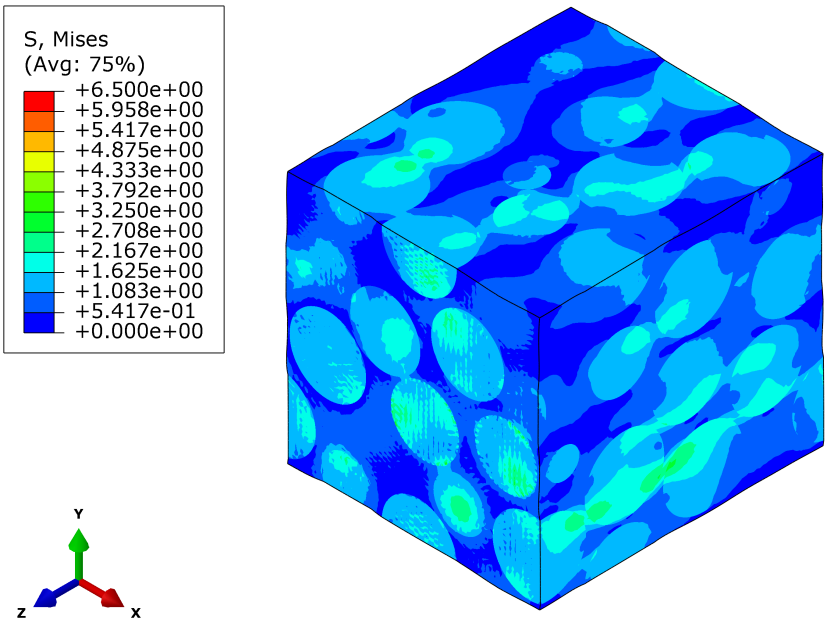

Figure 4.5: Resulting deformed shape of the SVE and predicted distribution of effective stress for an unidirectional load in z direction. ($\xi_p = 0.55$, $c_{el} = 10$, 40 particles)

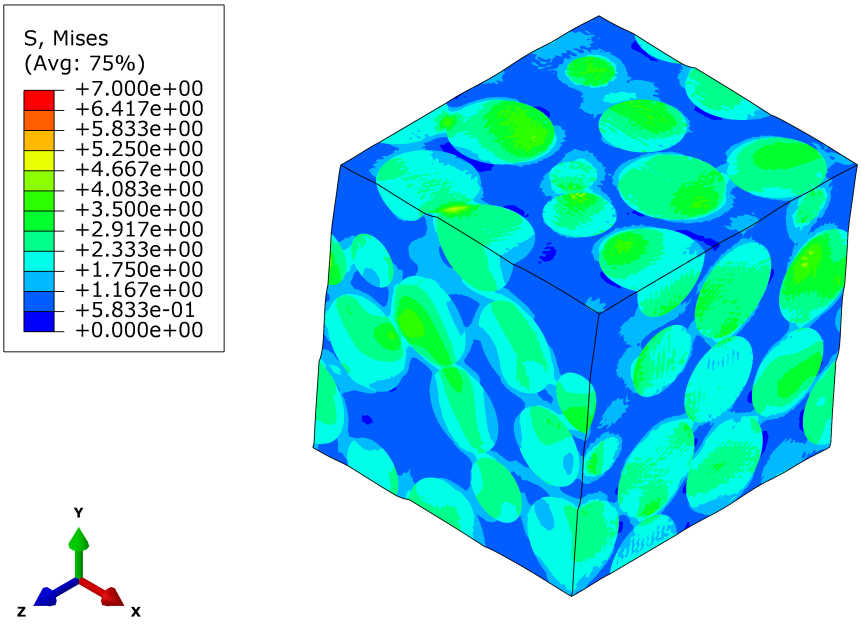

Figure 4.6: Resulting deformed shape of the SVE and predicted distribution of effective stress for a shear load in $x - y$ direction. ($\xi_p = 0.55$, $c_{el} = 10$, 40 particles)

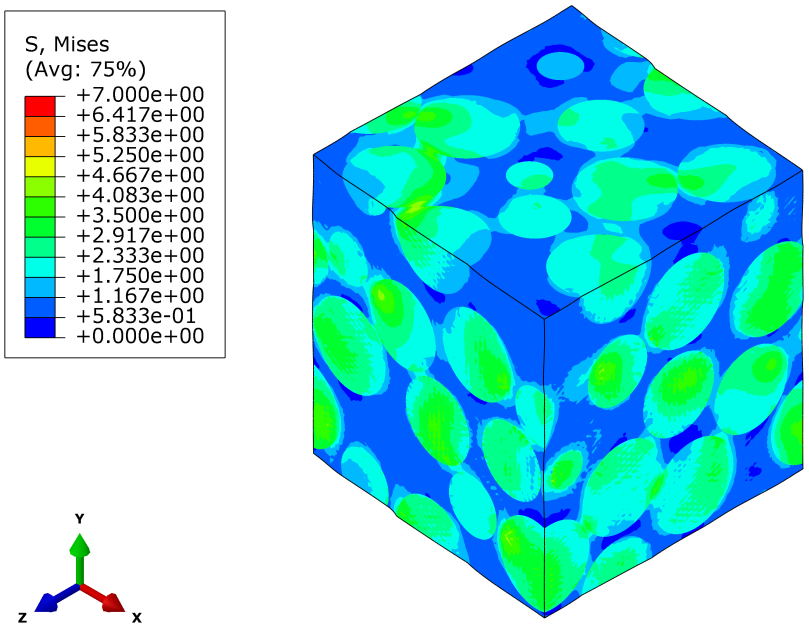

Figure 4.7: Resulting deformed shape of the SVE and predicted distribution of effective stress for a shear load in $x - z$ direction. ($\xi_p = 0.55$, $c_{el} = 10$, 40 particles)

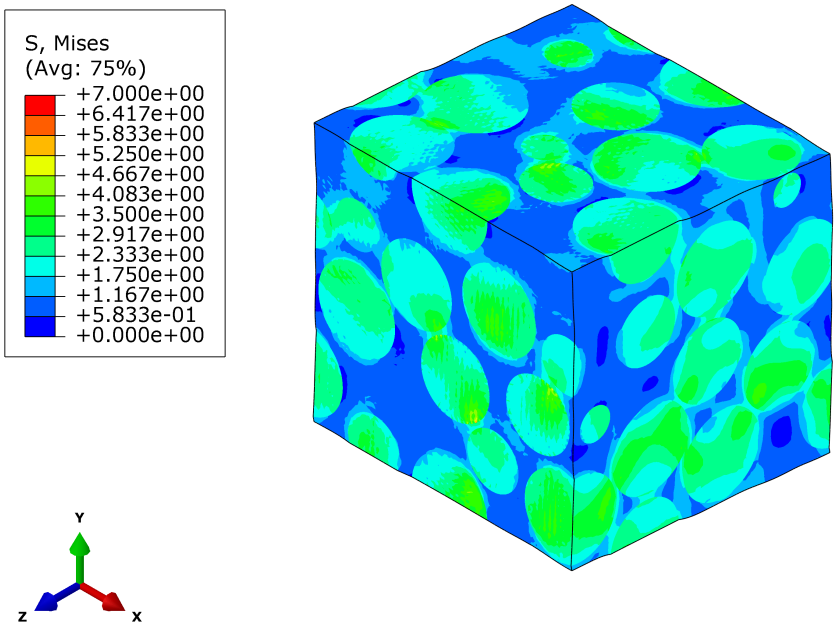

Figure 4.8: Resulting deformed shape of the SVE and predicted distribution of effective stress for a shear load in $y - z$ direction. ($\xi_p = 0.55$, $c_{el} = 10$, 40 particles)

Table 4.2: Comparison of the normalized effective shear modulus G and bulk modulus K obtained with smooth and voxel models. The deviations ΔK and ΔG are given in % and normalized with respect to the smooth meshes. (elastic contrast $c_{\mathrm{el}} = 10$)

	G		K		Deviations	
ξ_{p}	Smooth	Voxel	Smooth	Voxel	ΔG	ΔK
0.05	0.42052	0.42304	0.88344	0.88522	0.5997	0.2013
0.10	0.46081	0.46556	0.93810	0.94129	1.0321	0.3407
0.15	0.50674	0.51404	0.99801	1.00275	1.4404	0.4751
0.20	0.55849	0.56885	1.06357	1.07017	1.8557	0.6206
0.25	0.61631	0.63013	1.13455	1.14313	2.2420	0.7562
0.30	0.68152	0.70081	1.21176	1.22386	2.8309	0.9985
0.35	0.76030	0.78374	1.30122	1.31505	3.0826	1.0628
0.40	0.85426	0.88546	1.40241	1.42107	3.6532	1.3306
0.45	0.96471	1.00631	1.51764	1.54152	4.3125	1.5735
0.50	1.07808	1.12934	1.63442	1.66268	4.7547	1.7291
0.55	1.20689	1.26576	1.76172	1.79373	4.8778	1.8170

4.2.1 Comparison of Smooth and Voxel Models

Whereas the smooth models used 10-node fully integrated tetrahedral elements (C3D10 in Abaqus), the voxel models employed fully integrated 8-node hexahedra (C3D8 in Abaqus), each representing a voxel. The meshing parameters for the tetrahedra were set such that each analysis had approximately three millions degrees of freedom. For smaller particle volume fractions the internal coarsening option for the meshing reduced that number a little, see section 3.3.1. For the standard voxel meshes 125 voxels in each direction were chosen. This results in six million degrees of freedom, which is close to the convergence limit, see section 4.3. Identical microgeometries were used with the two types of models to achieve comparable results.

The results are presented in figure 4.1. As one can see from the diagrams the voxel meshes tend to predict higher effective moduli compared to the smooth models. This

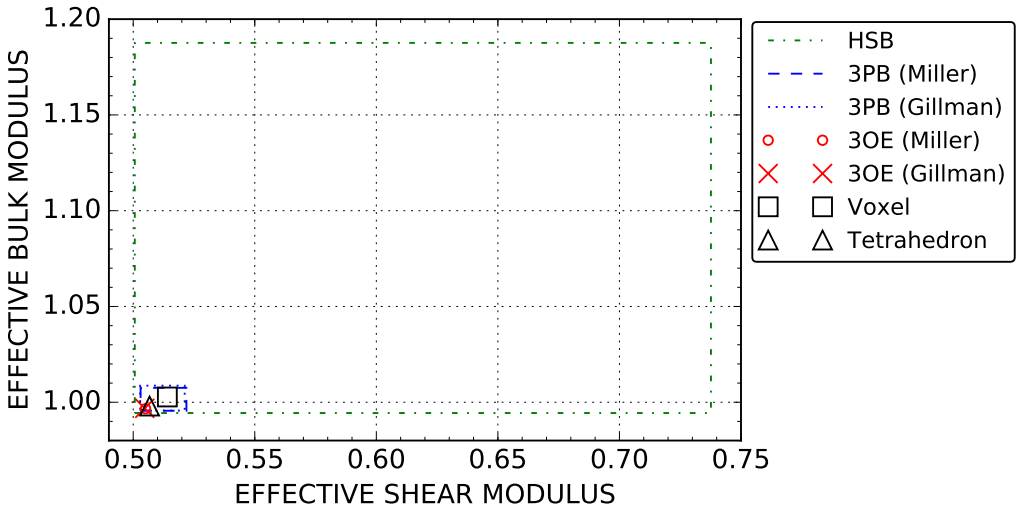

(a) Particle volume fraction $\xi_p = 0.15$

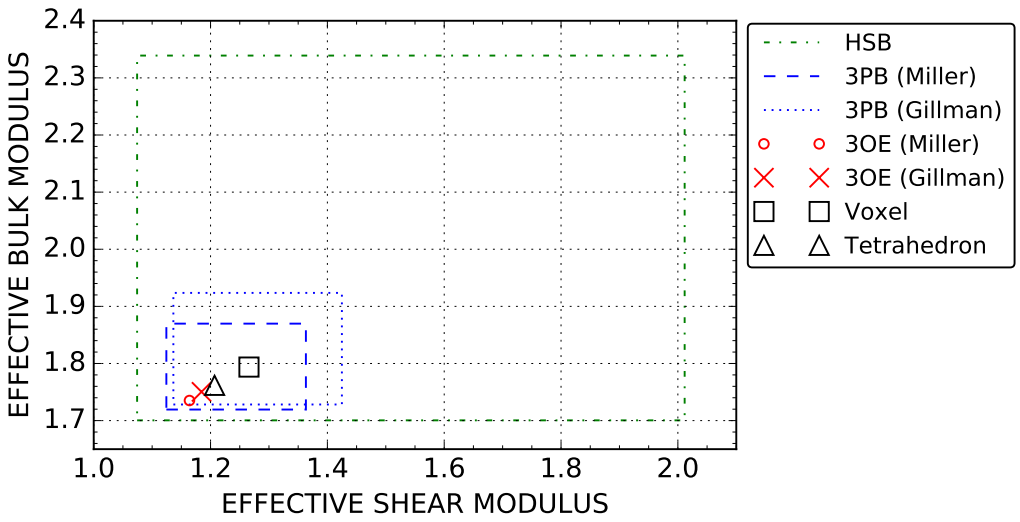

(b) Particle volume fraction $\xi_p = 0.55$

Figure 4.9: Comparison of bulk over shear modulus plots for different particle volume fractions ξ_p. The elastic contrast was $c_{el} = 10$.

is remarkable because the voxel meshes contain around twice as many degrees of freedom as smooth meshes and might, therefore, be expected to show a less stiff material behaviour. This indicates that the voxel meshes generated by Digimat tend to give rise to stiffer material properties for the given microgeometries and discretizations. Also, one can discern in table 4.2 that the values computed for the bulk modulus show

smaller differences between the two types of model than do the results for the shear modulus. This indicates that the voxel elements, in terms of these analyses, show a stiffer shape change performance compared to the volume change performance.

Figure 4.9 shows so-called bulk over shear modulus plots for two different particle volume fractions, which provide information on the bounds and estimates at the chosen particle volume fractions. One can again see that the smooth models tend to give lower moduli compared to the voxel meshes for the volume fractions shown.

Comparison of Different Statistical Parameters

In this section the material properties computed with the smooth models using tetrahedral elements are compared with the third-order estimates using two different sets of statistical parameters, see section 2.4.5. Table 4.3 shows the percentage deviation between the predictions from periodic homogenization and the third-order estimates. As one can see, the statistical parameters of Miller et al. give slightly closer agreement for the shear modulus for particle volume fractions of $\xi_{\mathrm{p}} \leq 0.3$. Beyond that value the full-field predictions of the shear and bulk moduli are closer to the estimates obtained with the statistical parameters of Gillman et al. The deviations indicate that beyond a particle volume fraction of $\xi_{\mathrm{p}} = 0.5$ both estimates tend to approach the numerical values again. The statistical parameters published by Gillman et al. give better agreement at evaluated particle volume fractions. For all cases considered, the ensemble averaged predictions of the smooth models lie slightly above the third-order estimates, the difference being clearly smaller for the bulk modulus. Since the results obtained with the voxel models are consistently stiffer than the ones predicted with the smooth meshes, the latter obviously are in better agreement with the analytical results.

Overall, there is very satisfactory agreement between the two modelling approaches despite the minor differences in the geometries considered.

Table 4.3: Normalized effective shear modulus G and bulk modulus K predicted with the third-order estimates using different sets of statistical parameters and an elastic contrast of $c_{\mathrm{el}} = 10$. The percentage deviations ΔK and ΔG are between the smooth mesh and the third-order estimates and are normalized with respect to the third-order estimates.

	Third-order estimates				Deviations			
	Gillman et al.		Miller et al.		Gillman et al.		Miller et al.	
ξ_{p}	G	K	G	K	ΔG	ΔK	ΔG	ΔK
0.05	0.42033	0.88331	0.42036	0.88328	0.0452	0.0148	0.0383	0.0178
0.10	0.46018	0.93764	0.46030	0.93754	0.1363	0.0483	0.1095	0.0597
0.15	0.50476	0.99684	0.50508	0.99663	0.3915	0.1174	0.3283	0.1382
0.20	0.55479	1.06146	0.55541	1.06112	0.6676	0.1988	0.5549	0.2309
0.25	0.61161	1.13219	0.61207	1.13153	0.7688	0.2084	0.6940	0.2669
0.30	0.67603	1.20978	0.67613	1.20871	0.8112	0.1637	0.7963	0.2523
0.35	0.74934	1.29516	0.74874	1.29336	1.4628	0.4679	1.5438	0.6077
0.40	0.83311	1.38939	0.83149	1.38668	2.5388	0.9371	2.7375	1.1344
0.45	0.92998	1.49389	0.92633	1.49001	3.7341	1.5898	4.1428	1.8543
0.50	1.04195	1.61008	1.03559	1.60483	3.4675	1.5117	4.1030	1.8438
0.55	1.18454	1.75033	1.16392	1.73516	1.8868	0.6507	3.6918	1.5307

Low Particle Volume Fractions

At a fixed size of the unit cell and fixed numbers of particles going to smaller particle volume fractions implies that the diameter of the particles must become smaller. Accordingly, at very low particle volume fractions a voxel based mesh with the chosen discretization may not represent the spherical shape particularly well. In fact, in some cases the moduli predicted by such models slightly exceed the three-point bounds, see figure 4.10. This can be explained by the fact that the three-point bounds are sensitive to the geometric shape of the particles. The values are still within the Hashin-Shtrikman bounds, however, these bounds depend only on the phase volume fraction and the macroscopic symmetry of the composite. A comparison between discretizations for the particles can be found in figure 4.11. Note how the voxel mesh is limited in representing the spherical shapes.

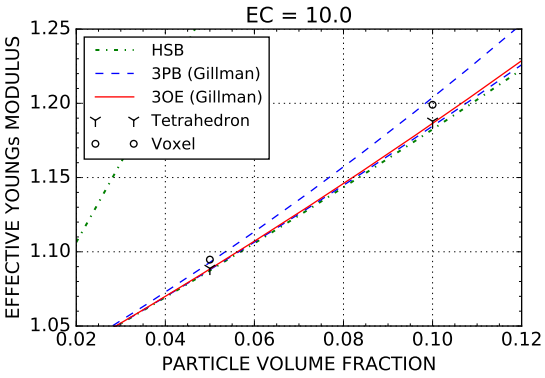

(a) Youngs's modulus

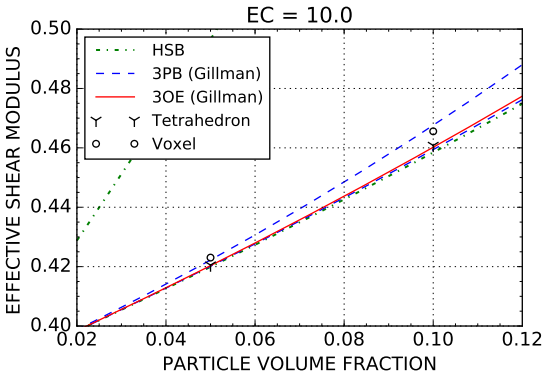

(b) Shear modulus

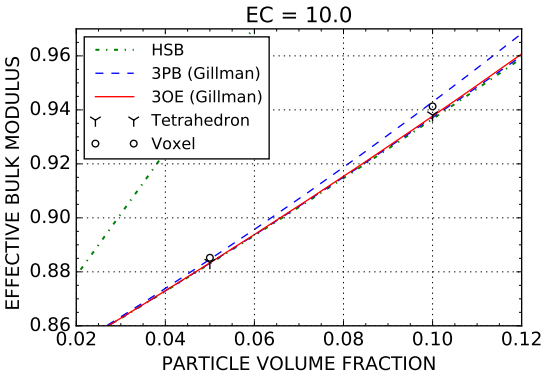

(c) Bulk modulus

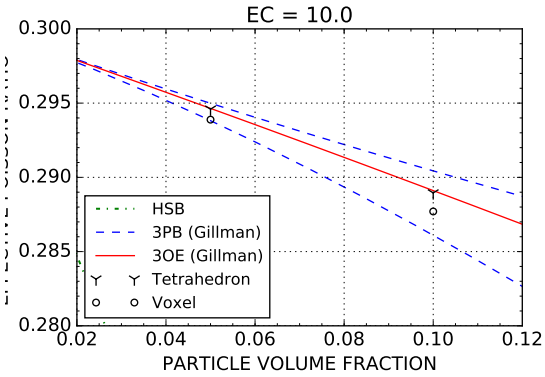

(d) Poisson's ratio

Figure 4.10: Enlarged section of the low particle volume fraction region of figure 4.1

4.2.2 Different Elastic Contrasts c_{el}

The following section concentrates on the effective material behaviour for different elastic contrasts c_{el}. There were four different sets of material parameters used for this analysis, the pertinent data being listed in table 4.1 along with the elastic contrasts c_{el}. The same sets of microgeometries as in section 4.2 were used in order to obtain comparable results.

The results can be found in figures 4.12, 4.13 and 4.14. The numerical values of the moduli predicted for the different discretizations are listed in tables 4.4, 4.6 and 4.8. Enlarged versions of the plots are provided in the appendices A.2, A.3 and A.4 be-

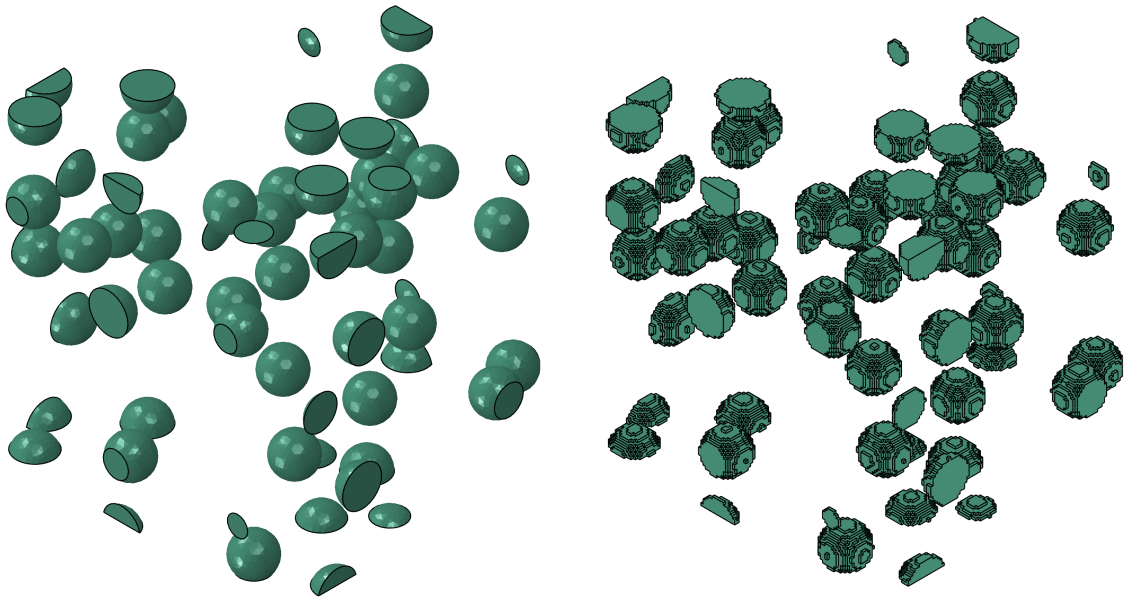

(a) Tetrahedron mesh **(b)** Voxel mesh

Figure 4.11: Phase arrangement for a particle volume fraction of $\xi_p = 0.05$ meshed with quadratic tetrahedra to obtain a smooth mesh (a) and discretized with a voxel mesh (b). Both are meshed with the parameters used in the main analysis.

ginning with page 76. Tables 4.5, 4.7 and 4.9 provide the corresponding predictions from the third-order estimates and their percentage deviation from smooth meshes. As can be seen from figure 4.12 the voxel models tend towards higher effective moduli compared to the smooth meshes for the elevated elastic contrast of $c_{el} = 100$, especially at elevated particle volume fractions. This statement can be verified via the deviations of the material properties shown in table 4.4. One can see that the percentage deviations between the two sets of models increase drastically with increasing particle volume fraction ξ_p. For a particle volume fraction of $\xi_p = 0.55$ the difference between shear moduli evaluated with the voxel and smooth meshes exceeds 20%. As for the elastic contrast $c_{el} = 10$, for all cases considered the predictions obtained with the smooth meshes are higher than the third-order estimates, but lie below the results of the voxel meshes.

For the case of particles that are more compliant than the matrix, $c_{el} = 0.1$, how-

ever, the smooth models using tetrahedral elements predict stiffer effective material behaviour. The differences in the shear and bulk moduli between voxel and smooth meshes always remains below 1% in this regime and therefore is of minor importance, see table 4.6. All predicted material properties are closer to the upper three-point bound rather than the lower one, see in figure 4.13. Such behaviour is typical for composites consisting of compliant inhomogeneities in a stiffer matrix. The third-order estimates are very similar to the simulated results and do not seem to show a clear trend with respect to them.

Decreasing the elastic contrast further to $c_{\text{el}} = 0.01$ leads to similar behaviour as seen for $c_{\text{el}} = 0.1$. The computed material properties are closer to the upper three-point bound as well as the third-order estimate. Table 4.8 shows that the percentage deviation between the meshes is bigger than for $c_{\text{el}} = 0.1$. Nevertheless, the maximum deviation is less than 3%, with respect to the smooth mesh, which is smaller than the deviations computed for $c_{\text{el}} = 100$. It is also worth mentioning that the percentage deviation for the bulk modulus is bigger than the one for the shear modulus. This behaviour is reversed compared to that for $c_{\text{el}} = 100$. Again, no consistent ordering with respect to the third-order estimates is present, although there seems to be some tendency for the latter scheme to predict higher bulk moduli than do the voxel models.

Table 4.4: Comparison of the normalized effective shear modulus G and bulk modulus K computed with different types of mesh for an elastic contrast of $c_{\mathrm{el}} = 100$. The deviations ΔK and ΔG are given in % and are normalized with respect to the smooth mesh.

	G		K		Deviations	
ξ_{p}	Smooth	Voxel	Smooth	Voxel	ΔG	ΔK
0.05	0.42742	0.43239	0.90267	0.90741	1.1630	0.5248
0.15	0.53682	0.55542	1.07221	1.08978	3.4651	1.6387
0.25	0.68682	0.73128	1.28783	1.33534	6.4723	3.6892
0.35	0.90670	0.98936	1.59686	1.67098	9.1169	4.6416
0.45	1.28845	1.51636	2.08692	2.29122	17.6887	9.7895
0.55	1.76183	2.17558	2.67023	3.03515	23.4841	13.6662

Table 4.5: Normalized effective shear modulus G and bulk modulus K predicted with the third-order estimates using the statistical parameters from Gillman et al. and an elastic contrast of $c_{\mathrm{el}} = 100$. The percentage deviations ΔK and ΔG are between the smooth mesh and the third-order estimates and are normalized with respect to the third-order estimates.

	Third-order estimates		Deviations	
ξ_{p}	G	K	ΔG	ΔK
0.05	0.42703	0.90239	0.0895	0.0311
0.15	0.53140	1.06790	1.0200	0.4036
0.25	0.67184	1.28180	2.2306	0.4704
0.35	0.86713	1.56552	4.5635	2.0019
0.45	1.14875	1.95553	12.1610	6.7189
0.55	1.61072	2.56124	9.3815	4.2554

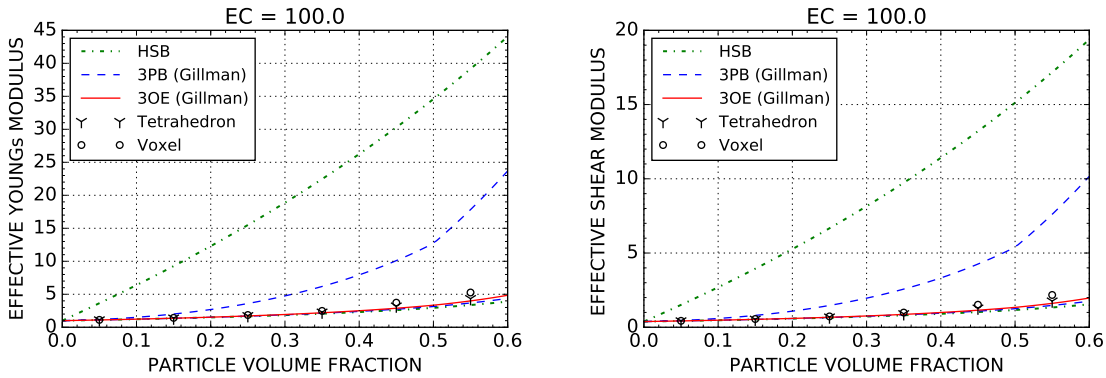

(a) Youngs's modulus

(b) Shear modulus

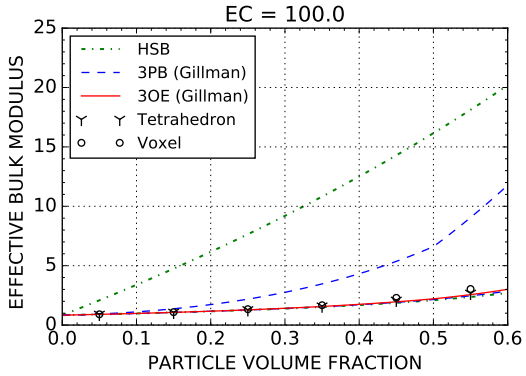

(c) Bulk modulus

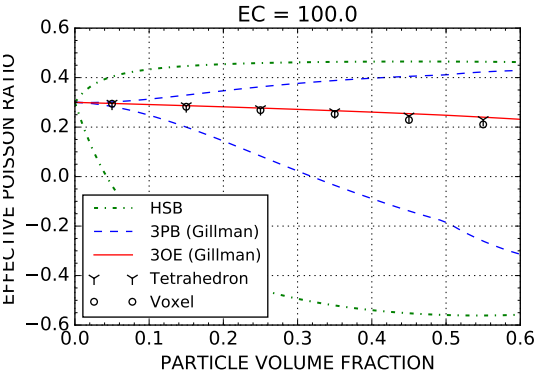

(d) Poisson's ratio

Figure 4.12: Effective material properties predicted with smooth and voxel meshes in comparison with various bounds and estimates for an elastic contrast of $c_{\mathrm{el}} = 100$.

Table 4.6: Comparison of the normalized effective shear modulus G and bulk modulus K computed with different types of mesh for an elastic contrast of $c_{\mathrm{el}} = 0.1$. The percentage deviations ΔK and ΔG are between the smooth mesh and the third-order estimates and are normalized with respect to the third-order estimates.

	G		K		Deviations	
ξ_{p}	Smooth	Voxel	Smooth	Voxel	ΔG	ΔK
0.05	0.35621	0.35604	0.74306	0.74207	-0.0463	-0.1327
0.15	0.30366	0.30338	0.59179	0.59017	-0.0939	-0.2741
0.25	0.25657	0.25653	0.47042	0.47015	-0.0136	-0.0565
0.35	0.21503	0.21458	0.37488	0.37259	-0.2130	-0.6127
0.45	0.17668	0.17614	0.29186	0.28921	-0.3056	-0.9086
0.55	0.14457	0.14427	0.22755	0.22573	-0.2089	-0.8003

Table 4.7: Normalized effective shear modulus G and bulk modulus K predicted with the third-order estimates using the statistical parameters from Gillman et al. and an elastic contrast of $c_{\mathrm{el}} = 0.1$. The percentage deviations ΔK and ΔG are between the smooth mesh and the third-order estimates and are normalized with respect to the third-order estimates.

	Third-order estimates		Deviations	
ξ_{p}	G	K	ΔG	ΔK
0.05	0.35615	0.74291	0.0022	0.0202
0.15	0.30368	0.59125	-0.0056	0.0925
0.25	0.25673	0.47007	-0.0627	0.0751
0.35	0.21486	0.37201	0.0833	0.7712
0.45	0.17777	0.29179	-0.6131	0.0247
0.55	0.14393	0.22158	0.4447	2.6970

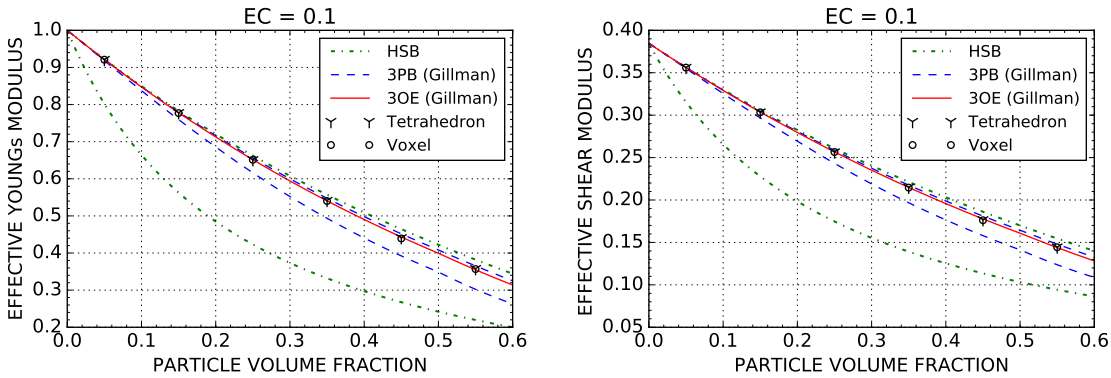

(a) Youngs's modulus

(b) Shear modulus

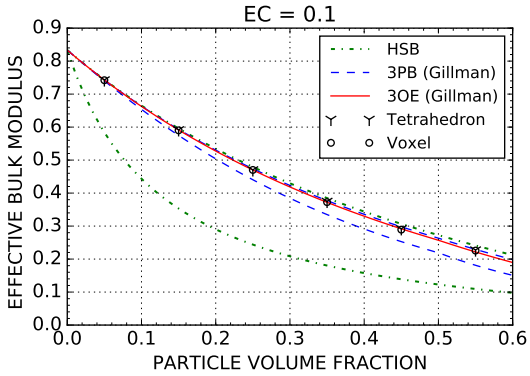

(c) Bulk modulus

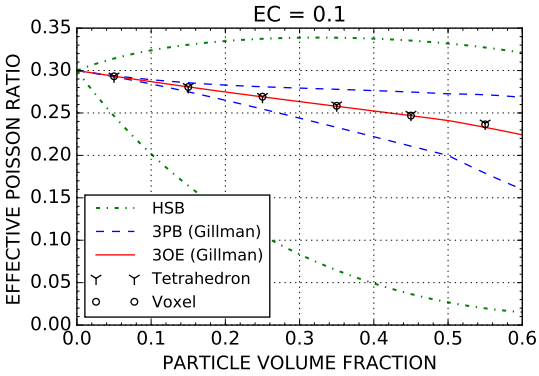

(d) Poisson's ratio

Figure 4.13: Effective material properties predicted with smooth and voxel meshes in comparison with various bounds and estimates for an elastic contrast of $c_{\mathrm{el}} = 0.1$.

Table 4.8: Comparison of the normalized effective shear modulus G and bulk modulus K computed with different types of mesh for an elastic contrast of $c_{\mathrm{el}} = 0.01$. The deviations ΔK and ΔG are given in % and are normalized with respect to the smooth mesh.

	G		K		Deviations	
ξ_{p}	Smooth	Voxel	Smooth	Voxel	ΔG	ΔK
0.05	0.34930	0.34924	0.72849	0.73014	-0.0192	0.2268
0.15	0.28585	0.28505	0.56379	0.56223	-0.2774	-0.2767
0.25	0.23071	0.22913	0.43703	0.43301	-0.6835	-0.9212
0.35	0.18145	0.17990	0.33408	0.33003	-0.8526	-1.2126
0.45	0.13658	0.13486	0.24716	0.24222	-1.2630	-1.9995
0.55	0.10167	0.09989	0.18373	0.17888	-1.7574	-2.6386

Table 4.9: Normalized effective shear modulus G and bulk modulus K predicted with the third-order estimates using the statistical parameters from Gillman et al. and an elastic contrast of $c_{\mathrm{el}} = 0.01$. The percentage deviations ΔK and ΔG are between the smooth mesh and the third-order estimates and are normalized with respect to the third-order estimates.

	Third-order estimates		Deviations	
ξ_{p}	G	K	ΔG	ΔK
0.05	0.34979	0.73228	-0.1389	-0.5174
0.15	0.28639	0.56534	-0.1882	-0.2736
0.25	0.23066	0.43462	0.0212	0.5561
0.35	0.18197	0.33092	-0.2907	0.9543
0.45	0.13990	0.24774	-2.3703	-0.2333
0.55	0.10194	0.17475	-0.2560	5.1381

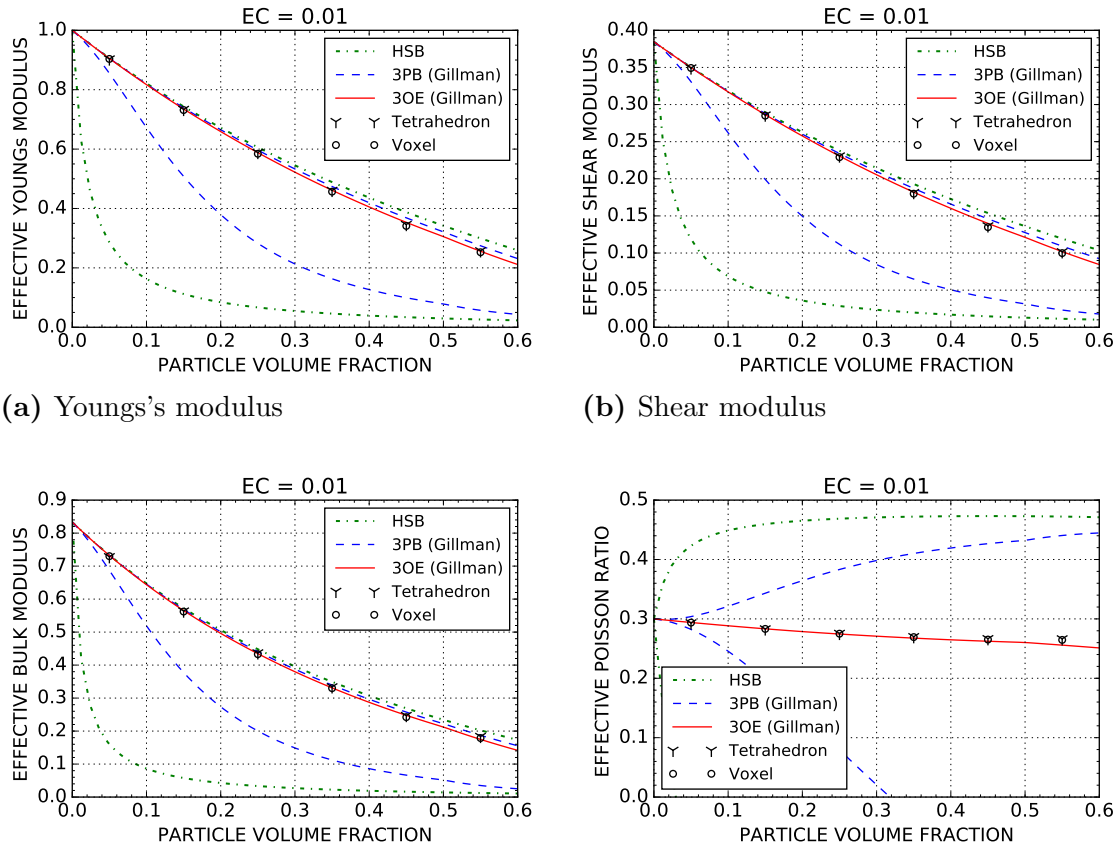

(a) Youngs's modulus

(b) Shear modulus

(c) Bulk modulus

(d) Poisson's ratio

Figure 4.14: Effective material properties predicted with smooth and voxel meshes in comparison with various bounds and estimates for an elastic contrast of $c_{\mathrm{el}} = 0.01$.

Table 4.10: Number of degrees of freedom (abbr. DOF) for different meshes used for analysis. The smooth meshes discretized with tetrahedral elements are used for comparison.

Element type		**DOF in Millions**					
Voxel		0.4	1.2	3.3	4	6	10
Tetrahedron	quadratic	0.6	3				
	linear	0.08	0.4	0.8			

4.3 Convergence Behaviour of Different Element and Mesh Types

As one can conclude from the preceding section the voxel based meshes tend to predict higher effective moduli, and thus stiffer macroscopic behaviour than smooth discretizations using tetrahedral elements. Therefore this sections takes a closer look at the convergence behaviour of the different discretizations. For this purpose five different phase arrangements of 40 particles each with a particle volume fraction of $\xi_{\mathrm{p}} = 0.55$ were studied. The material properties used for the constituents can be found in the first row of table 4.1, the elastic contrast being $c_{\mathrm{el}} = 10$. The results of the analysis were computed with the same set of five SVEs for different element types and differently fine discretizations. Afterwards the results were ensemble averaged and the closest isotropic tensor was evaluated to obtain the effective material properties.

The different element types were 10-node fully integrated tetrahedra with quadratic interpolation (C3D10 in Abaqus), 4-node fully integrated tetrahedra with linear interpolation (C3D4 in Abaqus) and 8-node hexahedra with linear interpolation (C3D8 in Abaqus) with full integration. The numbers of degrees of freedom of the different meshes are listed in table 4.10. For the voxel meshes the number of degrees of freedom is identical for the five different phase arrangements whereas for the smooth meshes the given numbers of degrees of freedom are the mean values of the different phase arrangements.

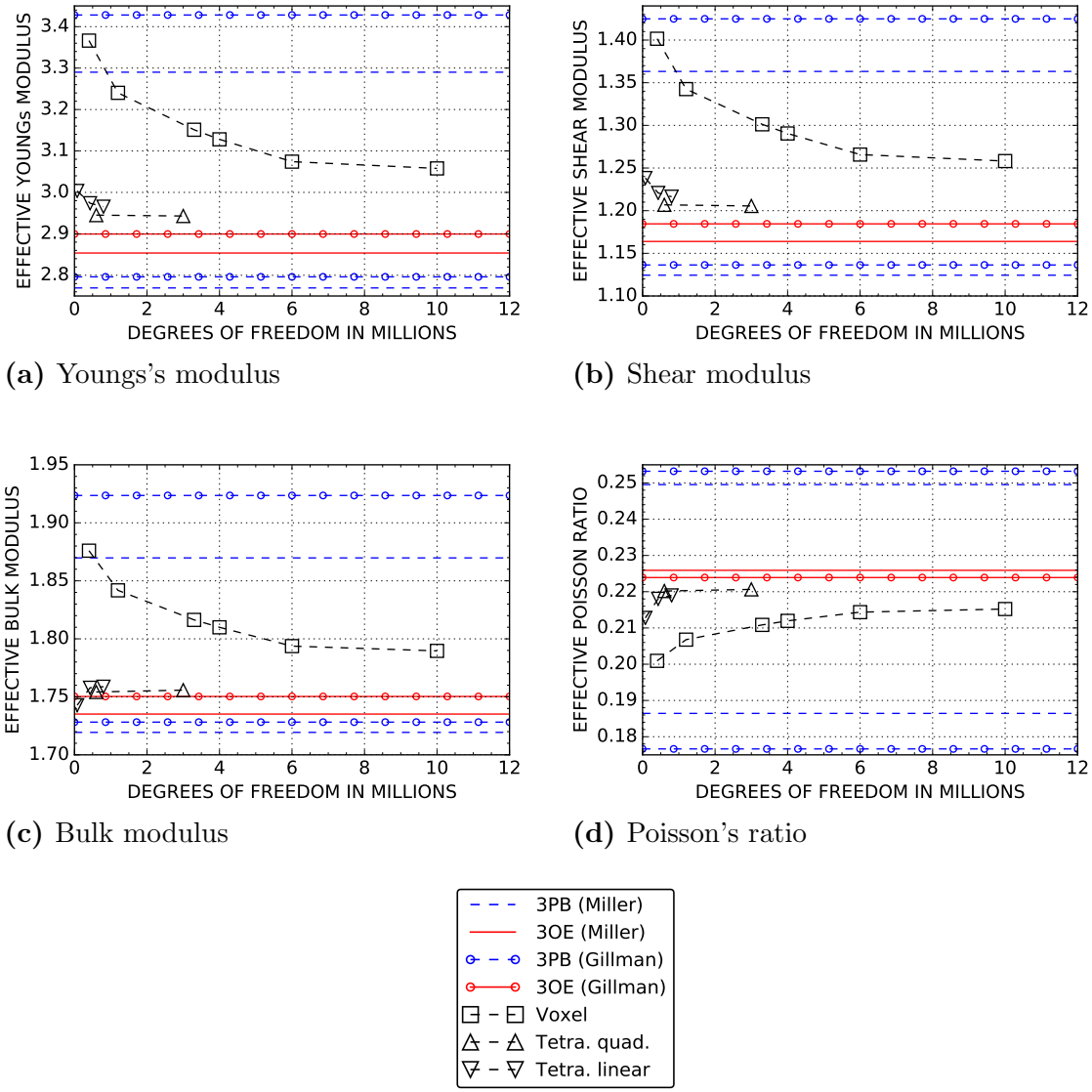

(a) Youngs's modulus

(b) Shear modulus

(c) Bulk modulus

(d) Poisson's ratio

(e) Legend

Figure 4.15: Comparison of the convergence behaviour of different models. Each analysis consists of 5 SVE, 40 particles each at $\xi_p = 0.55$. Three-point bounds and the third-order estimate with statistical parameters from Miller et al. and Gillman et al. are given as reference.

The results of the analyses are shown in figure 4.15. Enlarged versions of the plots are presented in appendix A.5, page 88.

The coarsest discretizations of the smooth meshes using quadratic and linear tetrahe-

dral elements have the same reference element size and the same number of elements. This was the coarsest discretization which could be meshed successfully. Nevertheless, for the smooth models using quadratic tetrahedral elements fairly good results are already achieved. The predicted material behaviour is close to the third-order estimates but slightly above them. A refinement of the mesh shows only a small tendency to approach the third-order estimates more closely, the predicted responses having essentially converged.

The smooth models meshed with linear tetrahedron elements show surprisingly good convergence behaviour and also quickly approach the predictions of the quadratic elements with higher refinement steps. One peculiarity which can be seen with the linear elements is that they underestimate the effective bulk modulus for very coarse discretizations.

The voxel based analyses show less satisfactory convergence behaviour in comparison to the smooth meshes. The material properties level off only at significantly higher numbers of degrees of freedom, and, for very coarse discretizations effective moduli are obtained that are outside the three-point bounds, probably due to the effects discussed in section 3.3.2. For figure 4.15 the statistical parameters by Miller et al. are used, which give rise to lower values of the upper bounds than the parameters derived by Gillman et al. Despite the fairly high number of degrees of freedom involved, the effective moduli predicted with the voxel meshes are noticeably higher than the results obtained with the smooth meshes and the third-order estimates.

For the main analysis voxel meshes with six millions degrees of freedom were used. As one can see in figure 4.15 this discretization gives results fairly close to the convergence limit.

4.4 Influence of SVE Size

For a fixed SVE size and a fixed number of particles, particle size must vary when the particle volume fraction is changing. Therefore, the ratio between the edge length

Table 4.11: Relation between particle volume fraction ξ_p and the ratio $\frac{L_{SVE}}{d_p}$. d_p is the diameter of the particles, the SVE size L_{SVE} and the number of particles n_p are fixed values. These are the same SVEs as used in section 4.2

L_{SVE}	ξ_p	n_p	d_p	$\frac{L_{SVE}}{d_p}$
1	0.05	40	0.1337	7.482
	0.10		0.1684	5.939
	0.15		0.1928	5.188
	0.20		0.2122	4.713
	0.25		0.2285	4.376
	0.30		0.2429	4.118
	0.35		0.2557	3.911
	0.40		0.2673	3.741
	0.45		0.2780	3.597
	0.50		0.2879	3.473
	0.55		0.2972	3.364
	0.60		0.3060	3.268

of the SVE and the particle diameter changes. This effect can be seen in table 4.11. According to Drugan and Willis [7] the latter parameter can be connected to the error on the effective material properties. They predict, that if the cell length to particle diameter ratio is $\frac{L_{SVE}}{d_p} > 2$ the maximum error in terms of the effective moduli will be less than 5%, irrespective of the particle volume fraction. For a ratio of $\frac{L_{SVE}}{d_p} \geq 4.5$ this error will drop below 1%. Segurado et al. [25] reported that, when using periodic boundary conditions, the scatter of the moduli will be "almost negligible" when $\frac{L_{SVE}}{d_p} > 3.74$ and $\xi_p \leq 0.3$.

Table 4.11 shows the values of n_p, d_p and $\frac{L_{SVE}}{d_p}$ pertaining to the volume elements used in this thesis. For the volume fractions in excess of $\xi_p = 0.4$, $\frac{L_{SVE}}{d_p}$ can be seen to fall below the value quoted in [25]. Therefore additional analyses for those particle volume fractions with a higher number of particles were done.

Since, in contrast to [7] and [25], the present work uses ensemble averaging and isotropization for improving the results, the above statements on the necessary size

Table 4.12: Parameters of the SVEs set up such that the ratio $\frac{L_{\mathrm{SVE}}}{d_{\mathrm{p}}}$ approaches a value of 5. The SVE edge length L_{SVE} was kept unchanged.

L_{SVE}	ξ_{p}	n_{p}	d_{p}	$\frac{L_{\mathrm{SVE}}}{d_{\mathrm{p}}}$
1	0.35	84	0.200	5.008
	0.40	90	0.204	4.902
	0.45	105	0.202	4.962
	0.50	100	0.210	4.714
	0.55	105	0.216	4.641
	0.60	105	0.222	4.508

of volume elements are not strictly applicable to it and probably are to conservative. The number of particles was increased to reach a ratio of $\frac{L_{\mathrm{SVE}}}{d_{\mathrm{p}}} = 5$. This, however, could not be achieved for all volume fractions considered because difficulties were encountered in generating sufficient numbers of meshable microgeometries with the desired parameters for particle volume fractions exceeding $\xi_{\mathrm{p}} = 0.50$. In table 4.12 one can see the SVE parameters which could be achieved.

4.4.1 Comparison of Differently Sized SVEs

A comparison of the effective moduli predicted with the SVEs defined in table 4.12 and with the smaller volume elements described in table 4.11 can be seen in figure 4.16. The same meshing parameters were used for five microgeometries for each volume fraction. Using the same meshing parameters but having smaller spheres to discretize leads to a poorer representation of the actual microgeometry, especially with respect to the shape of the spheres. As one can see in figure 4.16 the new smooth SVEs using tetrahedral elements result in slightly less stiff material behaviour which is well within the three-point bounds. This indicates that the larger numbers of particles, even thought they are less well discretized due to their smaller size, lead to material properties which are closer to the third order estimates.

There was no such clear effect for voxel based meshes. As one can see in figure 4.16

Table 4.13: Comparison of effective material properties predicted from volume elements containing different numbers of particles using smooth quadratic meshes. The exact number of particles used is given in table 4.12. The elastic contrast was $c_{\mathrm{el}} = 10$. The deviations are given in %, normalized with respect to the 40-particle SVEs.

	G		K		Deviations	
ξ_{p}	40 particles	"larger" SVE	40 particles	"larger" SVE	ΔG	ΔK
0.35	0.76030	0.75775	1.30122	1.29380	0.3351	0.5702
0.40	0.85426	0.84849	1.40241	1.39688	0.6753	0.3943
0.45	0.96471	0.95112	1.51764	1.50497	1.4083	0.8348
0.50	1.07808	1.06438	1.63442	1.62216	1.2708	0.7501
0.55	1.20689	1.20466	1.76172	1.75786	0.1848	0.2191
0.60	1.40125	1.40006	1.93807	1.93678	0.0849	0.0666

Table 4.14: Comparison of the normalized effective shear modulus G and bulk modulus K computed with different meshes for the "larger" SVEs containing more particles. The deviations ΔK and ΔG are given in %, normalized with respect to the smooth meshes. The elastic contrast is $c_{\mathrm{el}} = 10$.

	G		K		Deviations	
ξ_{p}	Smooth	Voxel	Smooth	Voxel	ΔG	ΔK
0.35	0.75775	0.78730	1.29380	1.31628	3.9000	1.7375
0.40	0.84849	0.88823	1.39688	1.42100	4.6836	1.7267
0.45	0.95112	1.00407	1.50497	1.53609	5.5670	2.0678
0.50	1.06438	1.12910	1.62216	1.65820	6.0805	2.2217
0.55	1.20466	1.29642	1.75786	1.81015	7.6171	2.9746
0.60	1.40006	1.54191	1.93678	2.01672	10.1317	4.1275

the averaged material properties obtained from the new set of SVEs are generally close to the results from the SVEs with a smaller number of particles with no obvious tendencies. This is interesting because a fixed number of voxels was used and thus one might expect the decreasing particle size to lead to badly resolved spheres. In figure 4.17 an example of such a voxel mesh is shown. Therefore it is remarkable that the predictions are still within the three-point bounds, which assume perfect spheres.

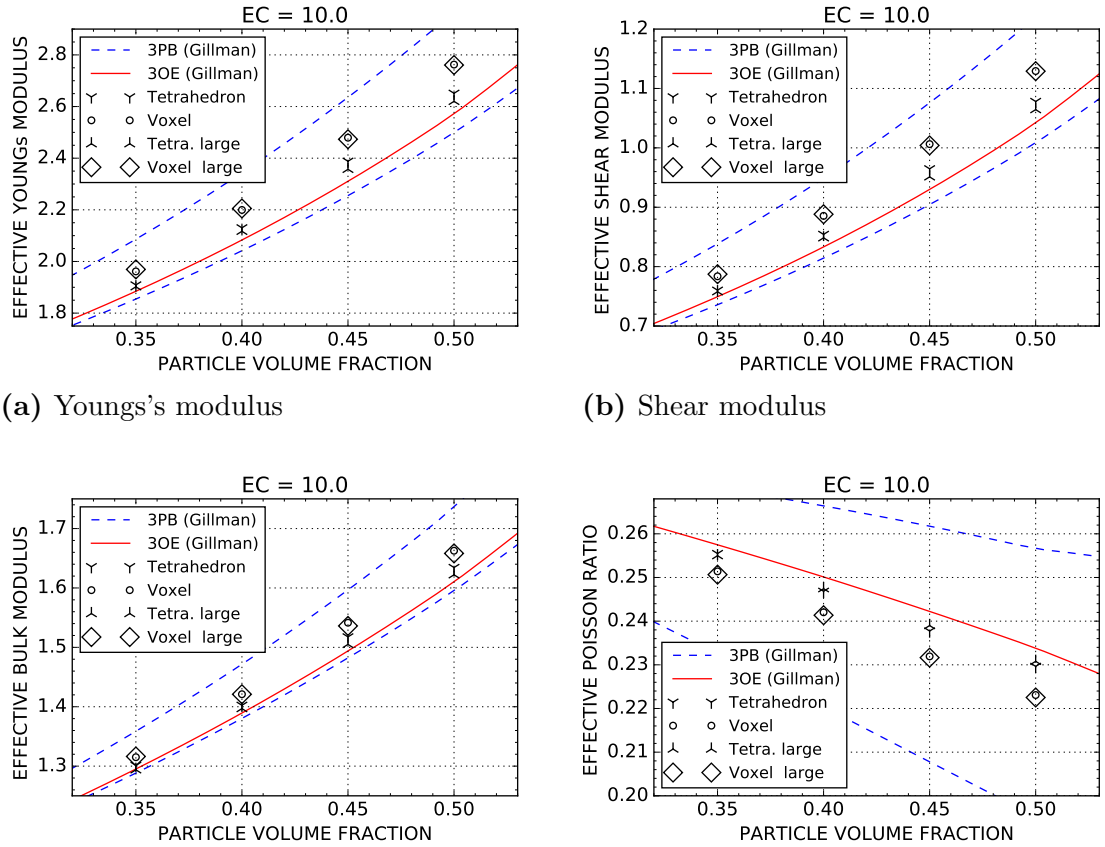

(a) Youngs's modulus

(b) Shear modulus

(c) Bulk modulus

(d) Poisson's ratio

Figure 4.16: Enlarged section of the upper part of range of particle volume fraction ξ_p. The resulting effective material properties were computed with smooth and voxel meshes for an elastic contrast of $c_{el} = 10$.

Table 4.13 shows the percentage deviations between the SVEs with standard and "large" numbers of particles. As one can see for the bulk modulus the difference is always below 1% and for the shear modulus the percentage deviation is always less than 1.5% The bulk modulus predicted with the voxel mesh using the high number of particles differs slightly more from the third-order estimates than does the value obtained with the "standard" arrangements of 40 particles. This may indicate that achieving smooth convergence with the voxel meshes may be non-trivial in terms of the voxel resolution required. The present analysis indicates that the improvement in terms of this analysis is not worth the effort for generating and meshing suitable

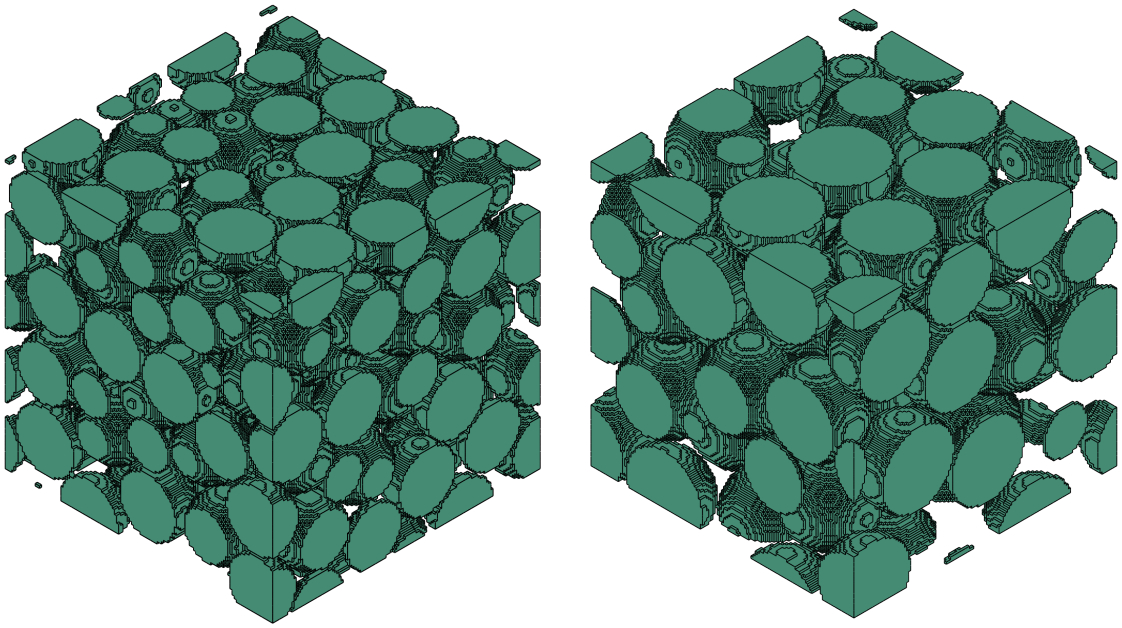

(a) 105 particles **(b)** 40 particles

Figure 4.17: Examples of voxel meshed arrangements used in this thesis with a particle volume fraction of $\xi_p = 0.55$ and 105 particles in comparison with another arrangement with $\xi_p = 0.55$ and 40 particles

microgeometries.

Table 4.14 shows a comparison of different moduli predicted with different meshes for the "larger" SVEs.

Arrangements with High Volume Fractions and Increased Numbers of Particles

Usually, in this thesis, the minimum distance between two particles was set to 0.01 of the particle diameter. Nevertheless, for some high particle volume fractions and SVEs with increased numbers of particles it was necessary to decrease this distance to values as small as 0.003 particle diameters. This had an influence on the meshing. With unchanged voxel discretization more particles tend to be connected and, therefore, super inhomogeneities are created, see section 3.3.2, because the voxels cannot

resolve the microgeometry anymore, leading to overestimating the effective moduli. Another issue, which appeared with the tetrahedra meshes, is that there was a significant number of microgeometries, which could be generated with Arigen, but were subjected to meshing complications. Generally speaking, out of ten tries to generate a satisfactory microgeometry only three to four could be meshed. This fact leaves doubts about the statistical quality of the resulting SVEs where the minimum distance between neighbouring particles is very small- the fact that many arrangements could not be meshed may bias the resulting effective moduli.

In figure 4.18 one can see the effective material properties predicted for the more highly packed arrangements. All the results obtained for the particle volume fraction of $\xi_{\mathrm{p}} = 0.6$ were obtained with microgeometries with reduced distance between the particles. This also applies to the results for $\xi_{\mathrm{p}} = 0.55$ and a particle count of $n_{\mathrm{p}} = 105$. As one can see the resulting effective moduli evaluated from the voxel models tend to increase and therefore represent a "stiffer" material characteristic. The effective material parameters which were computed with smooth meshes show little change, even though the number of particles per cell has doubled.

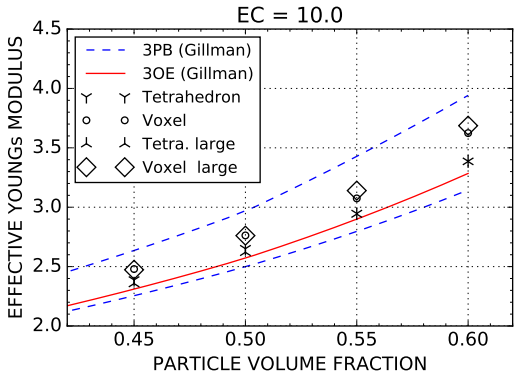

(a) Youngs's modulus

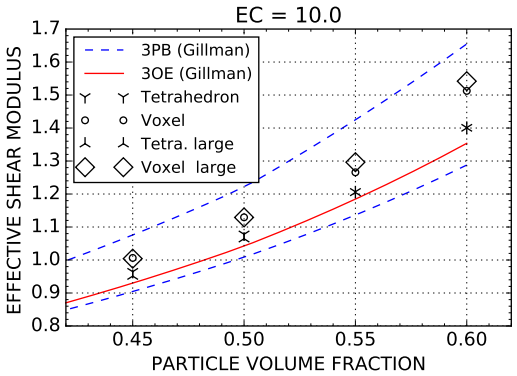

(b) Shear modulus

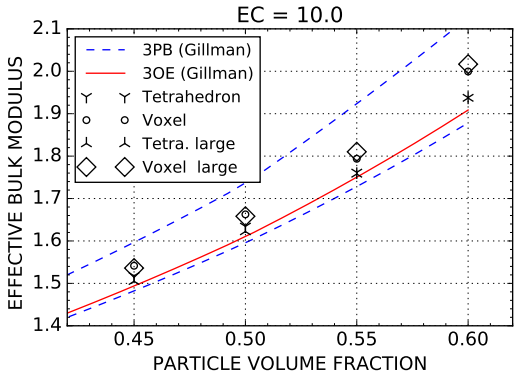

(c) Bulk modulus

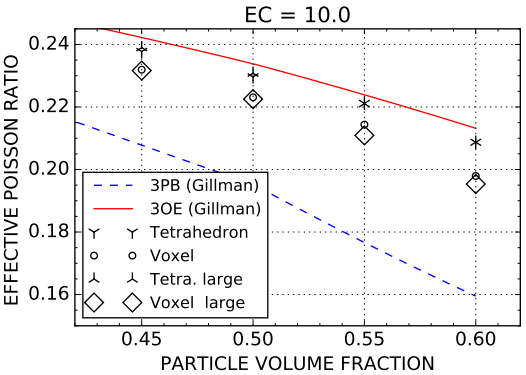

(d) Poisson's ratio

Figure 4.18: Results obtained with highly packed arrangements with decreased minimum distance between the particles. The resulting effective material properties were computed with smooth and voxel meshes for an elastic contrast of $c_{\mathrm{el}} = 10$.

Chapter 5

Conclusion

The present study compares different models for the effective elastic moduli and tensors of composites reinforced by identical spherical particles. These models compare two-point and three-point bounds, third-order estimates as well as smooth and voxel models employing discrete microstructures for periodic homogenization.

The predictions with smooth meshes were found to always comply with the three-point bounds, independent of the three-point statistical parameters used. Therefore, the properties are within the Hashin-Shtrikman bounds as well.

Comparing the smooth geometries with voxel the meshes leads to the observation that with rising particle volume fractions the predictions obtained with the smooth meshes tend to stay closer to analytical estimates than the voxel meshes, see section 4.2.1.

With rising elastic contrast c_{el} the results obtained with the voxels meshes show a clear tendency to exceed analytical estimates and numerical homogenization results using smooth models. This tendency, however, is much smaller for elastic contrasts c_{el} smaller than unity.

When using voxel meshes it is crucial to assure that the individual particles do not become connected due to an excessively coarse discretization. The smooth meshes

are not susceptible to this difficulty, but also show limitations in handling closely approaching particles.

The results indicate that ensemble averaging and isotropizing results from sets of statistically equal SVEs provides valid predictions in comparison with SVEs containing higher numbers of particles for the same particle volume fractions ξ_{p}.

In view of the very different underlying assumptions, the good agreement between the analytical and numerical methods compared in this thesis provides clear evidence of the validity on both types of model.

Appendix A

Results

A.1 Elastic Contrast $c_{\mathbf{el}} = 10$

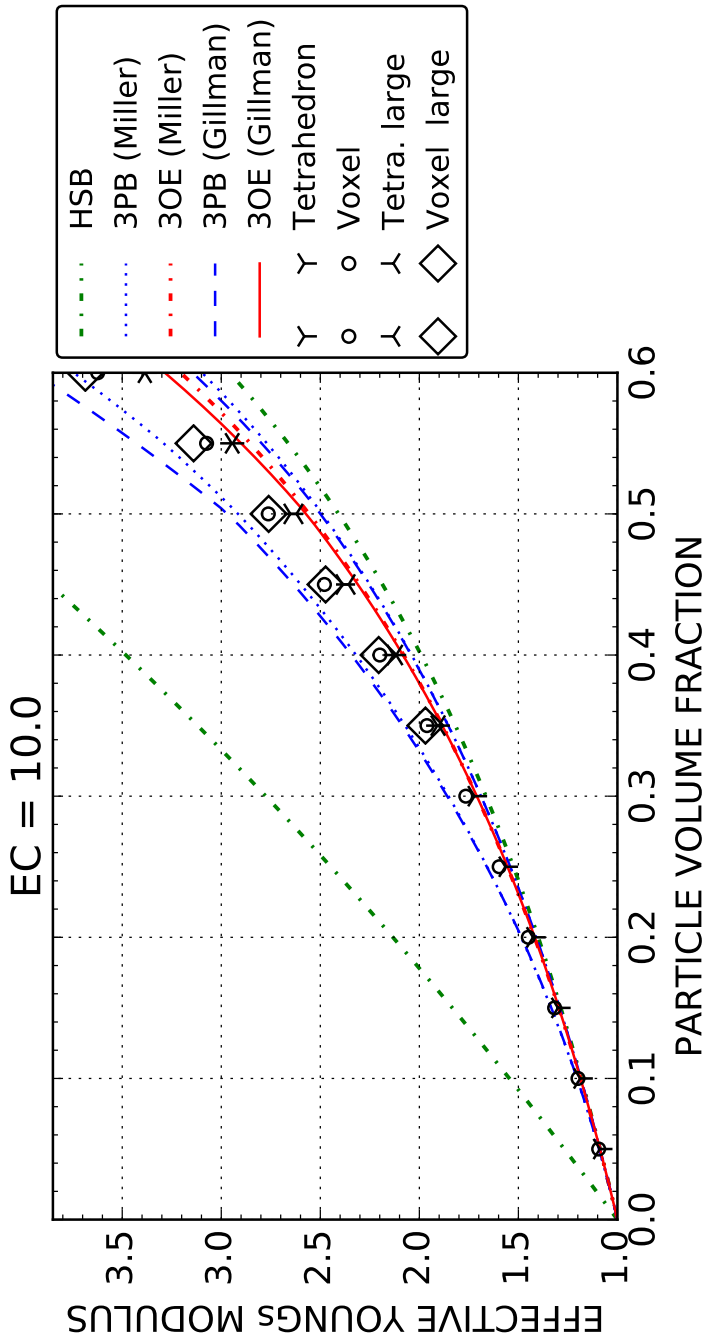

Figure A.1: Effective Young's moduli computed with smooth and voxel meshes in comparison with various bounds and estimates using different three-point statistics. The elastic contrast was $c_{\mathrm{el}} = 10$.

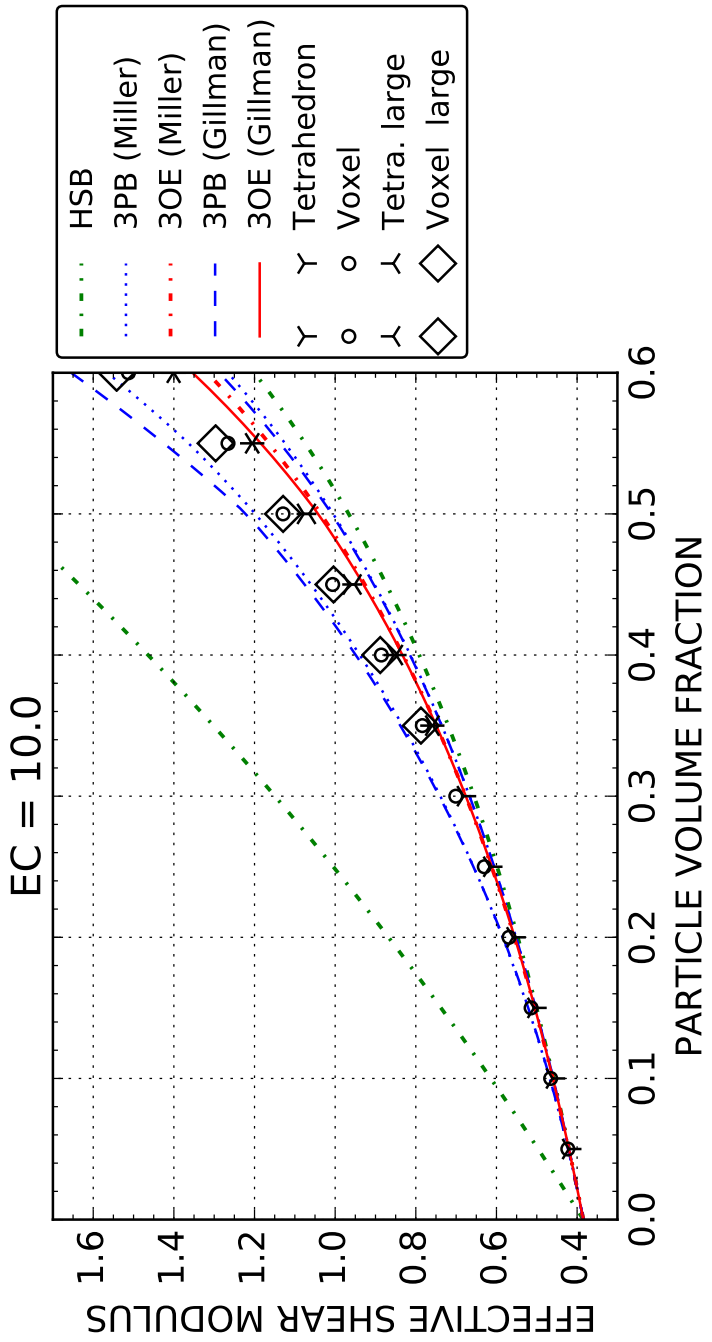

Figure A.2: Effective shear moduli computed with smooth and voxel meshes in comparison with various bounds and estimates using different three-point statistics. The elastic contrast was $c_{\mathrm{el}} = 10$.

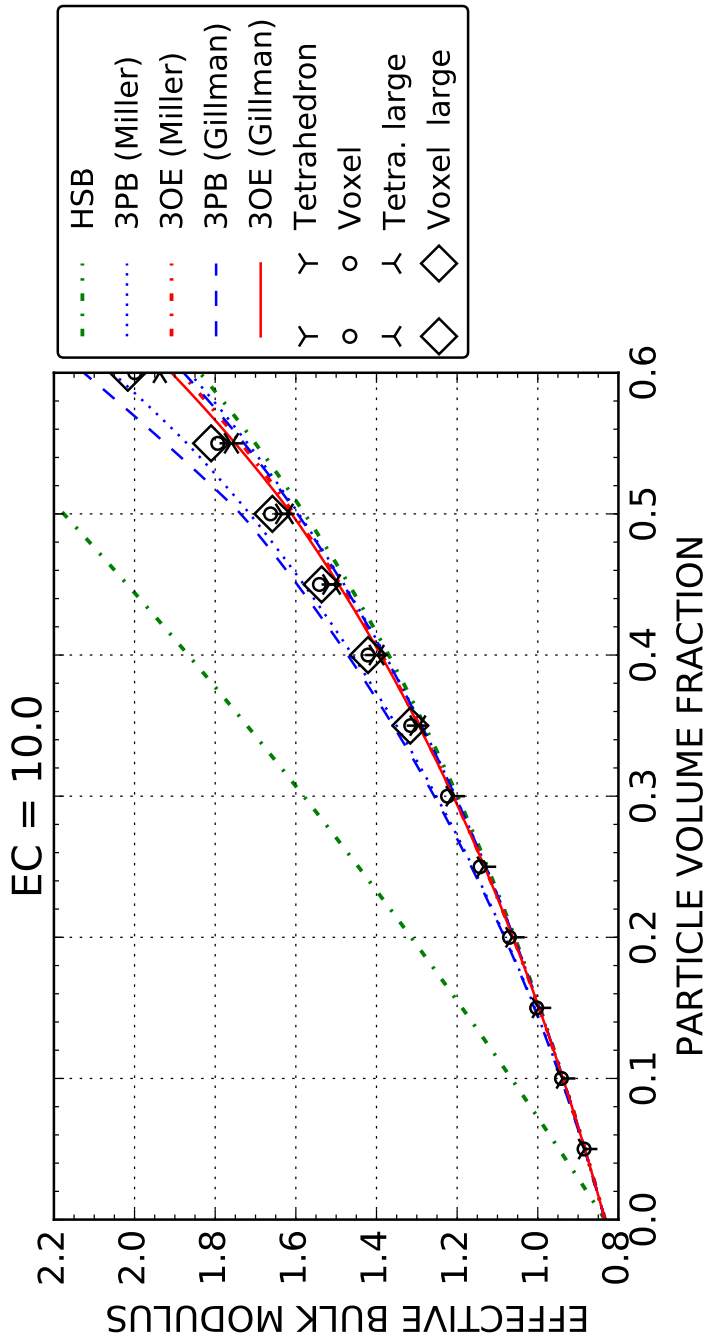

Figure A.3: Effective bulk moduli computed with smooth and voxel meshes in comparison with various bounds and estimates using different three-point statistics. The elastic contrast was $c_{\mathrm{el}} = 10$.

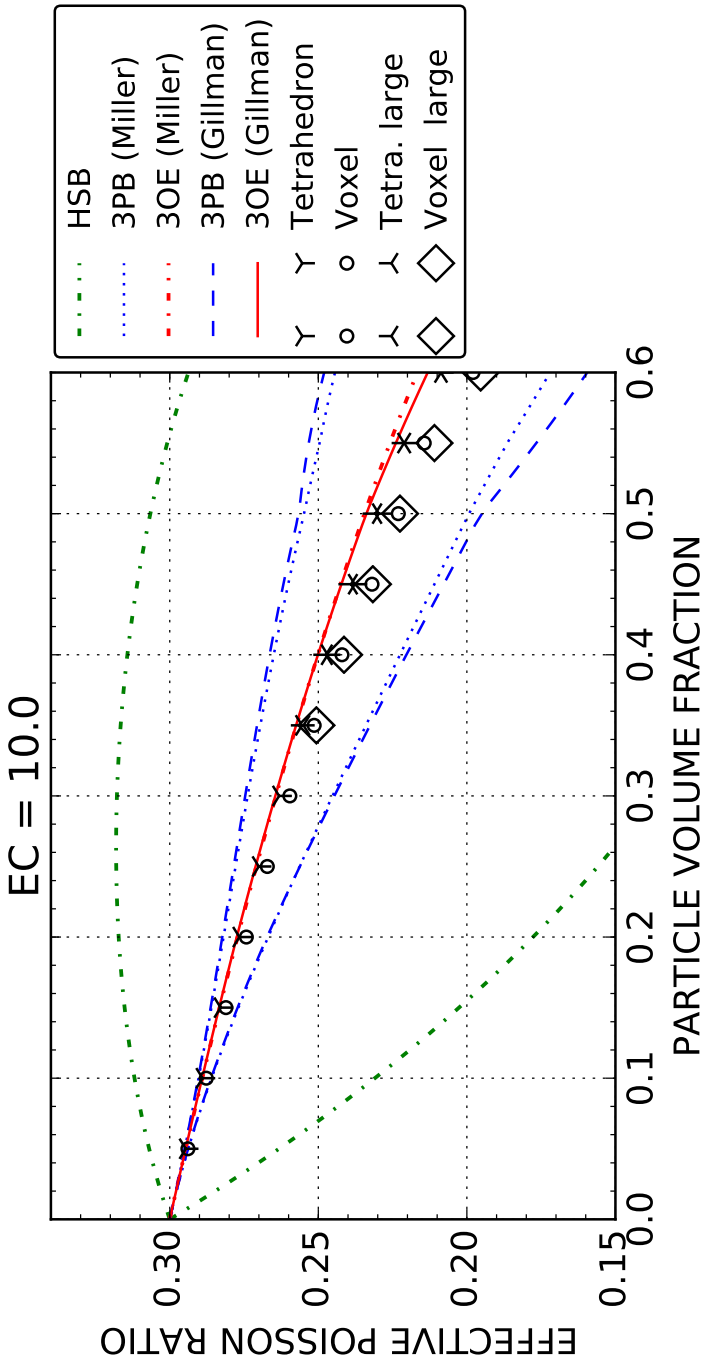

Figure A.4: Effective Poisson's ratios computed with smooth and voxel meshes in comparison with various bounds and estimates using different three-point statistics. The elastic contrast was $c_{\mathrm{el}} = 10$.

A.2 Elastic Contrast $c_{\mathrm{el}} = 100$

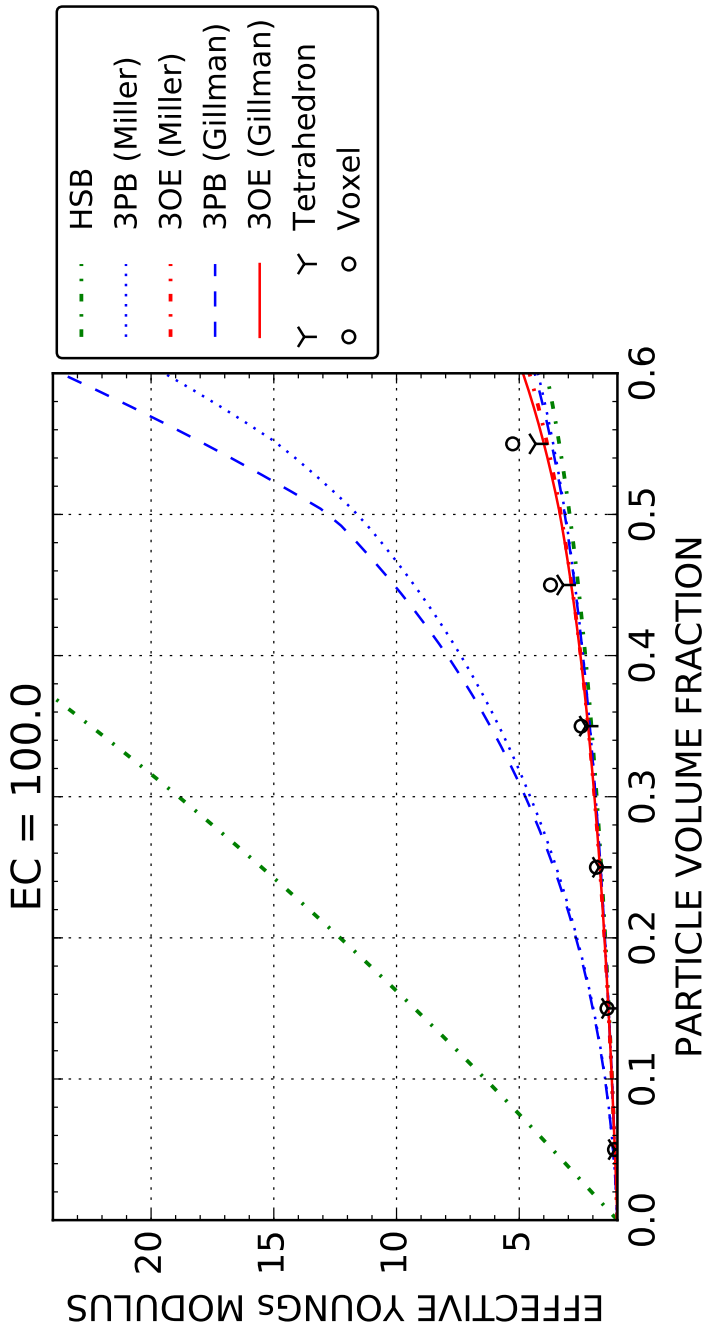

Figure A.5: Effective Young's moduli computed with smooth and voxel meshes in comparison with various bounds and estimates using different three-point statistics. The elastic contrast was $c_{\mathrm{el}} = 100$.

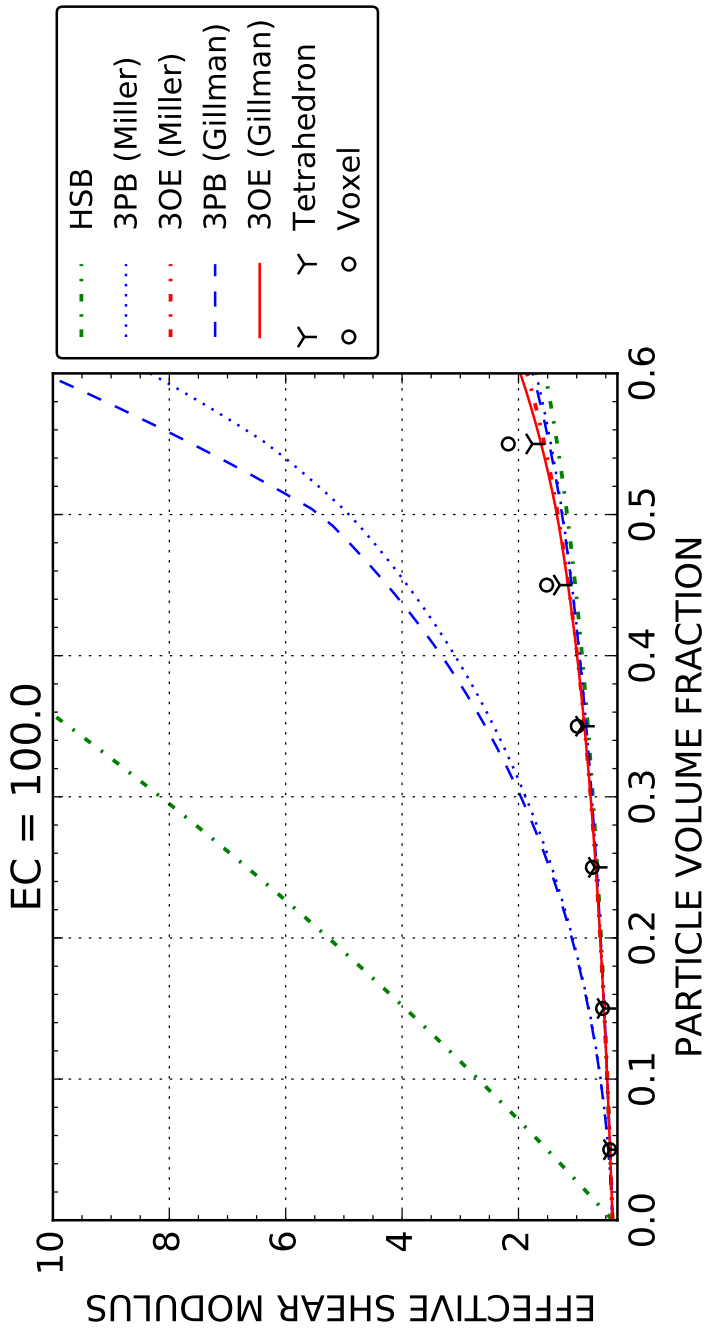

Figure A.6: Effective shear moduli computed with smooth and voxel meshes in comparison with various bounds and estimates using different three-point statistics. The elastic contrast was $c_{\mathrm{el}} = 100$.

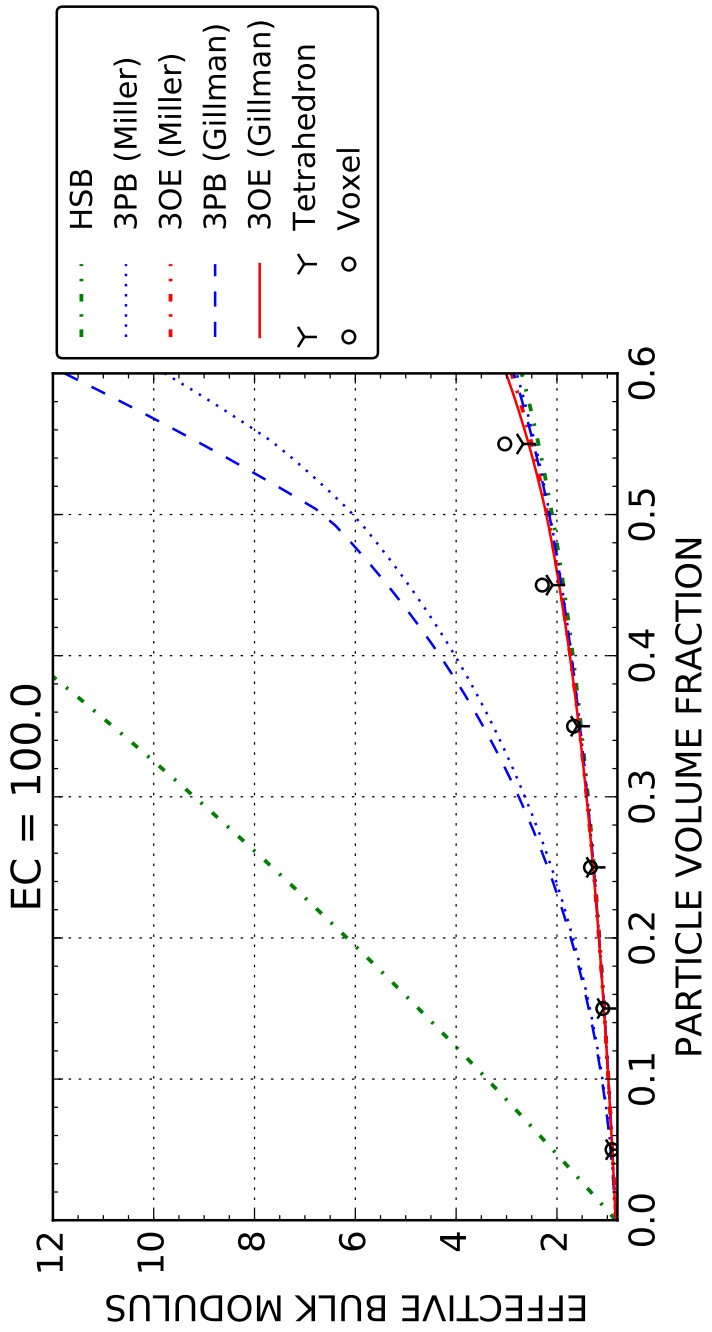

Figure A.7: Effective bulk moduli computed with smooth and voxel meshes in comparison with various bounds and estimates using different three-point statistics. The elastic contrast was $c_{\mathrm{el}} = 100$.

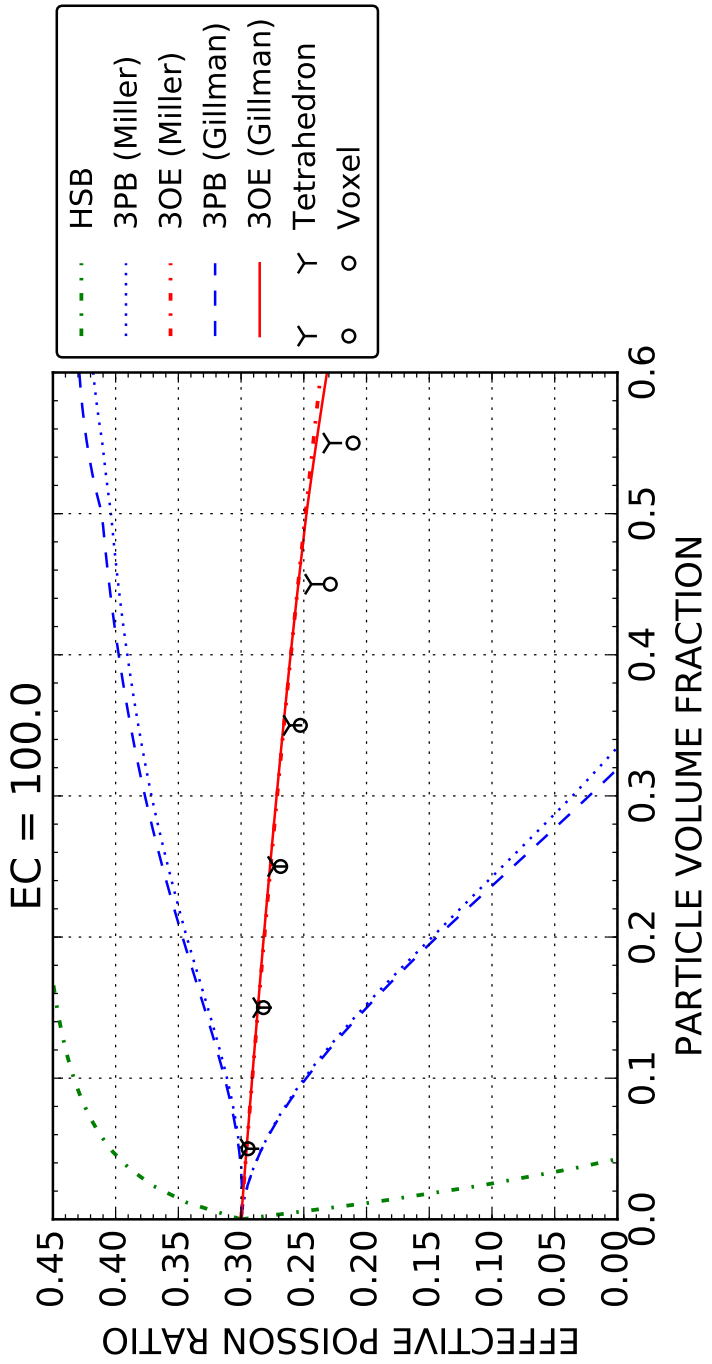

Figure A.8: Effective Poisson's ratios computed with smooth and voxel meshes in comparison with various bounds and estimates using different three-point statistics. The elastic contrast was $c_{\mathrm{el}} = 100$.

A.3 Elastic Contrast $c_{\mathrm{el}} = 0.1$

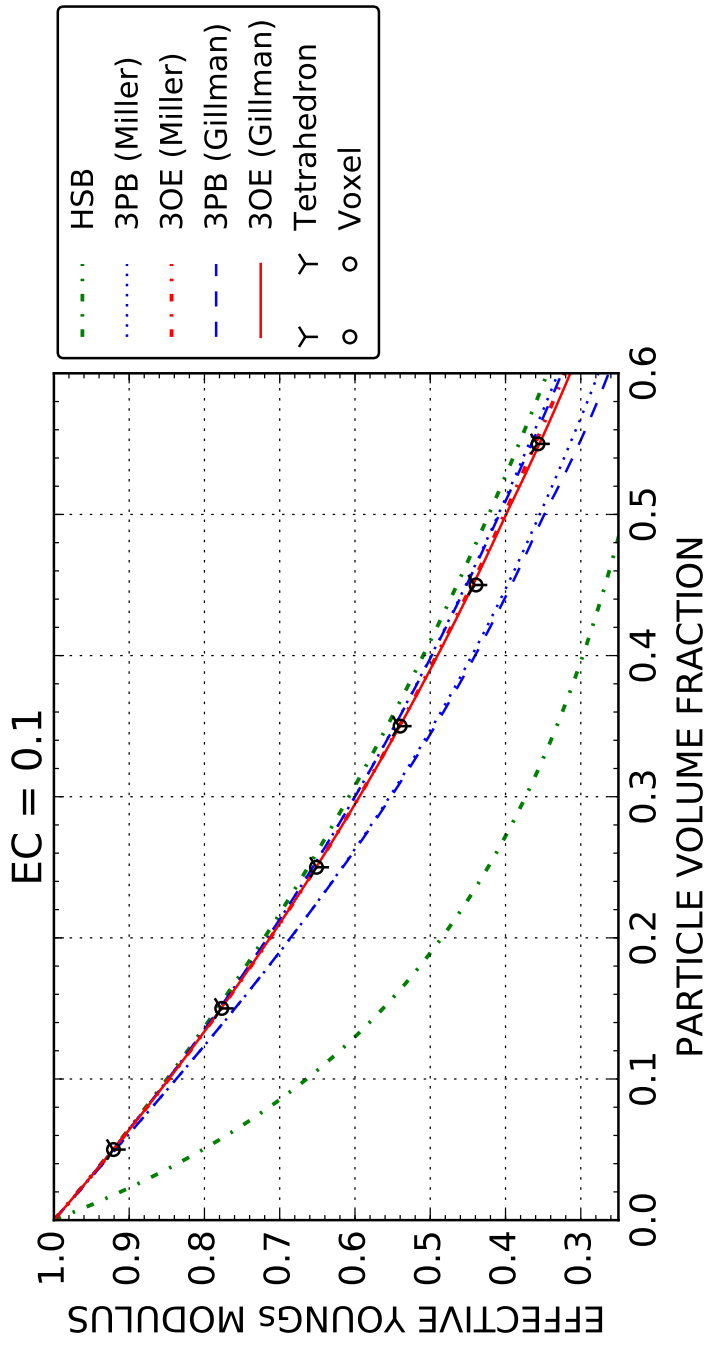

Figure A.9: Effective Young's moduli computed with smooth and voxel meshes in comparison with various bounds and estimates using different three-point statistics. The elastic contrast was $c_{\mathrm{el}} = 0.1$.

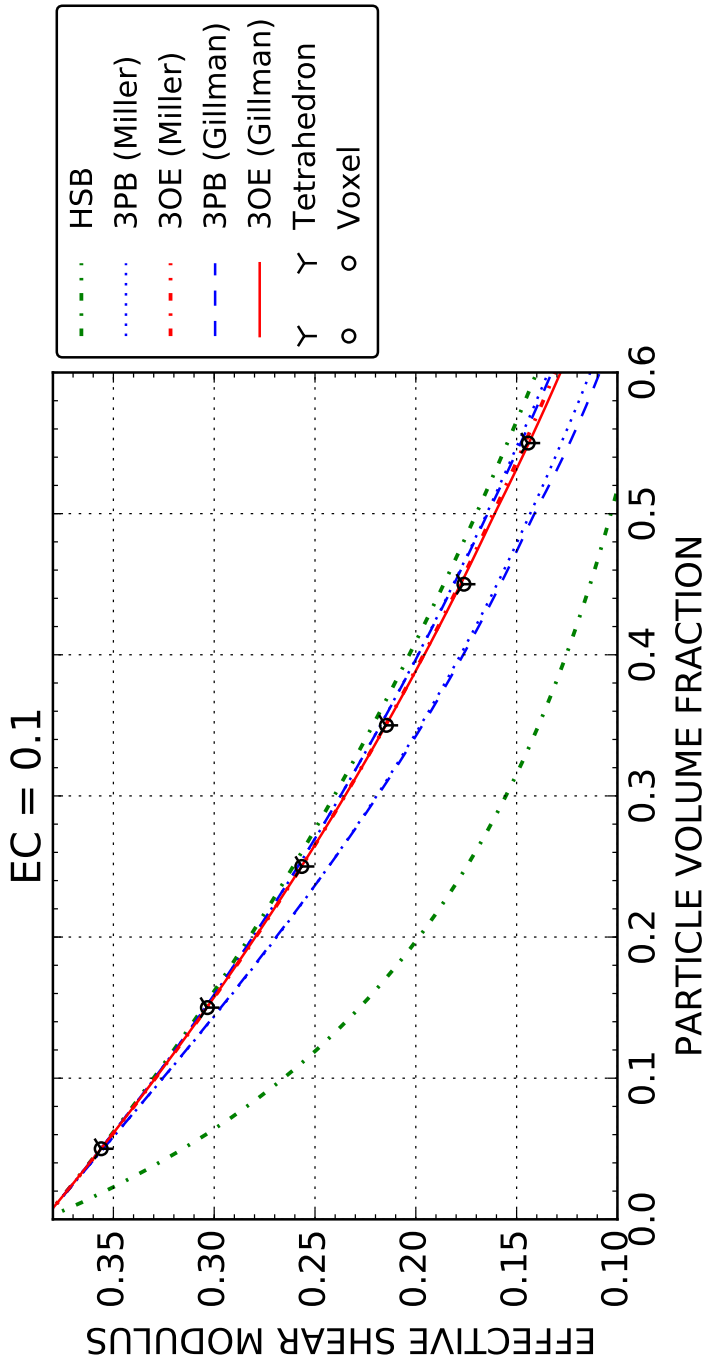

Figure A.10: Effective shear moduli computed with smooth and voxel meshes in comparison with various bounds and estimates using different three-point statistics. The elastic contrast was $c_{\mathrm{el}} = 0.1$.

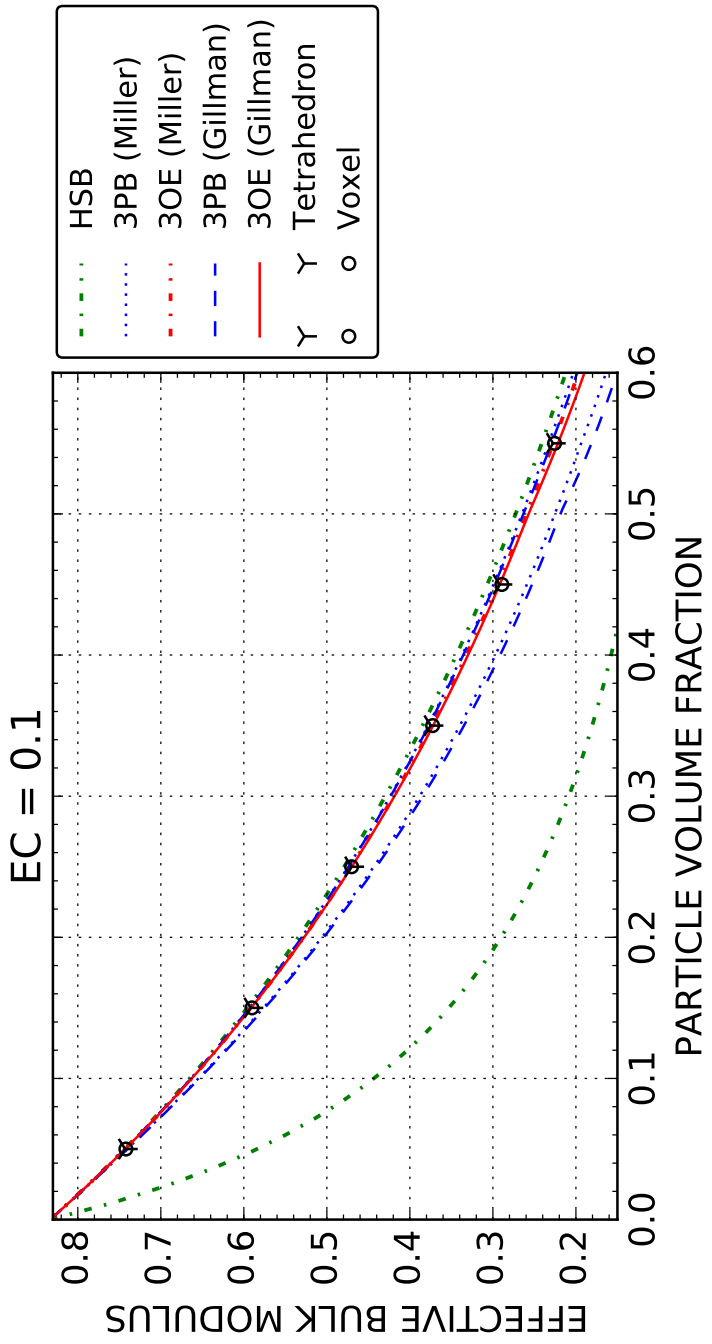

Figure A.11: Effective bulk moduli computed with smooth and voxel meshes in comparison with various bounds and estimates using different three-point statistics. The elastic contrast was $c_{\mathrm{el}} = 0.1$.

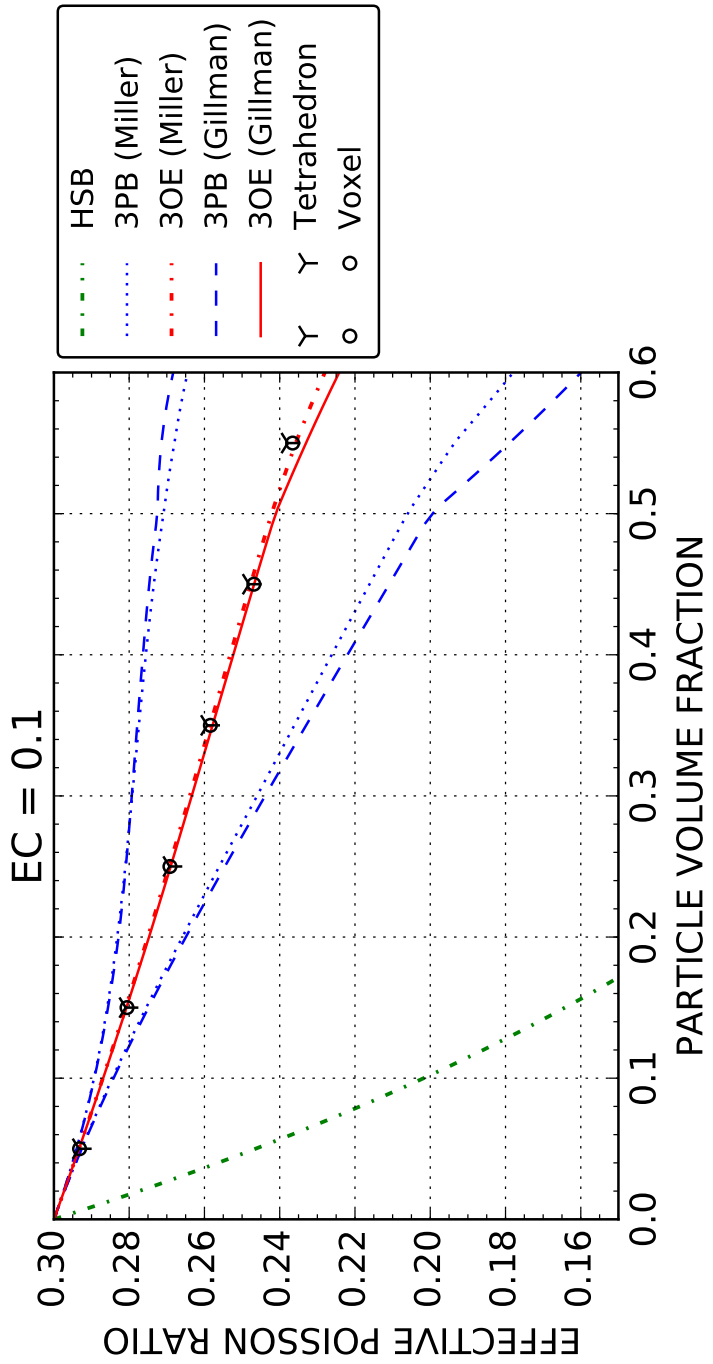

Figure A.12: Effective Poisson's ratios computed with smooth and voxel meshes in comparison with various bounds and estimates using different three-point statistics. The elastic contrast was was $c_{\mathrm{el}} = 0.1$.

A.4 Elastic Contrast $c_{\mathrm{el}} = 0.01$

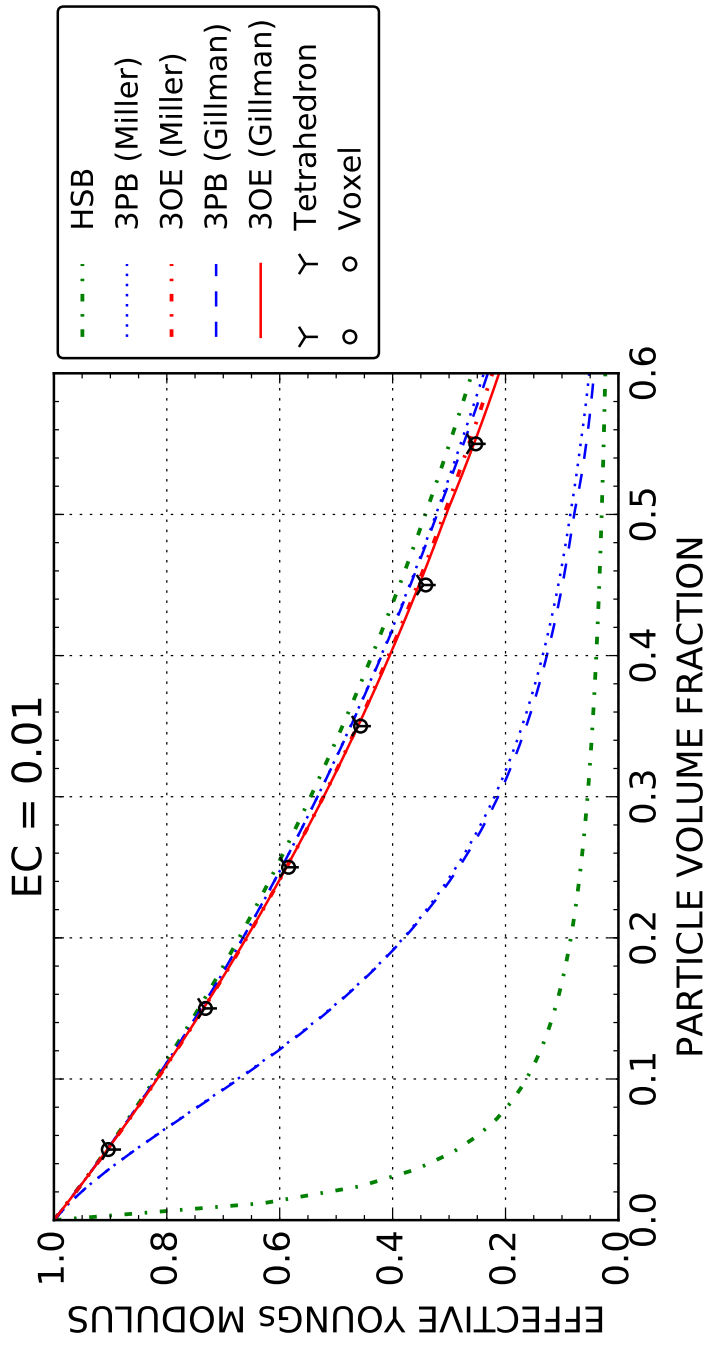

Figure A.13: Effective Young's moduli computed with smooth and voxel meshes in comparison with various bounds and estimates using different three-point statistics. The elastic contrast was $c_{\mathrm{el}} = 0.01$.

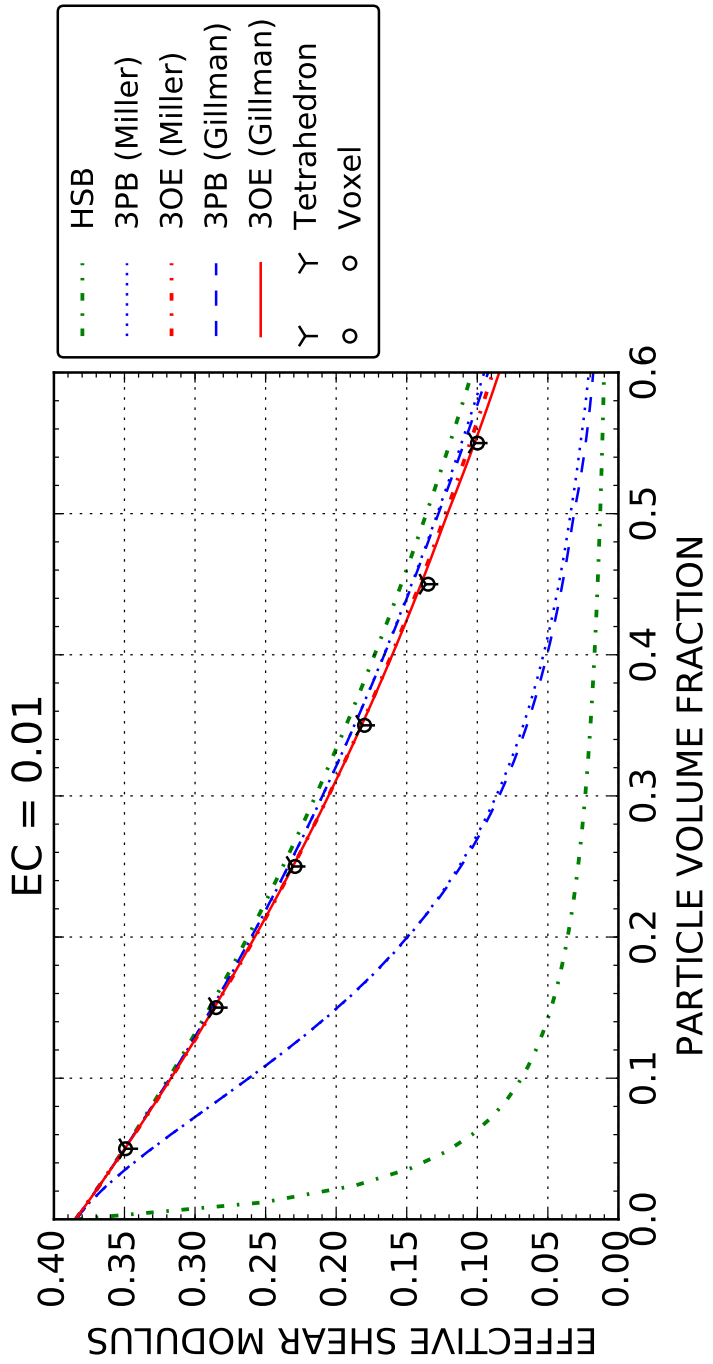

Figure A.14: Effective shear moduli computed with smooth and voxel meshes in comparison with various bounds and estimates using different three-point statistics. The elastic contrast was $c_{\mathrm{el}} = 0.01$.

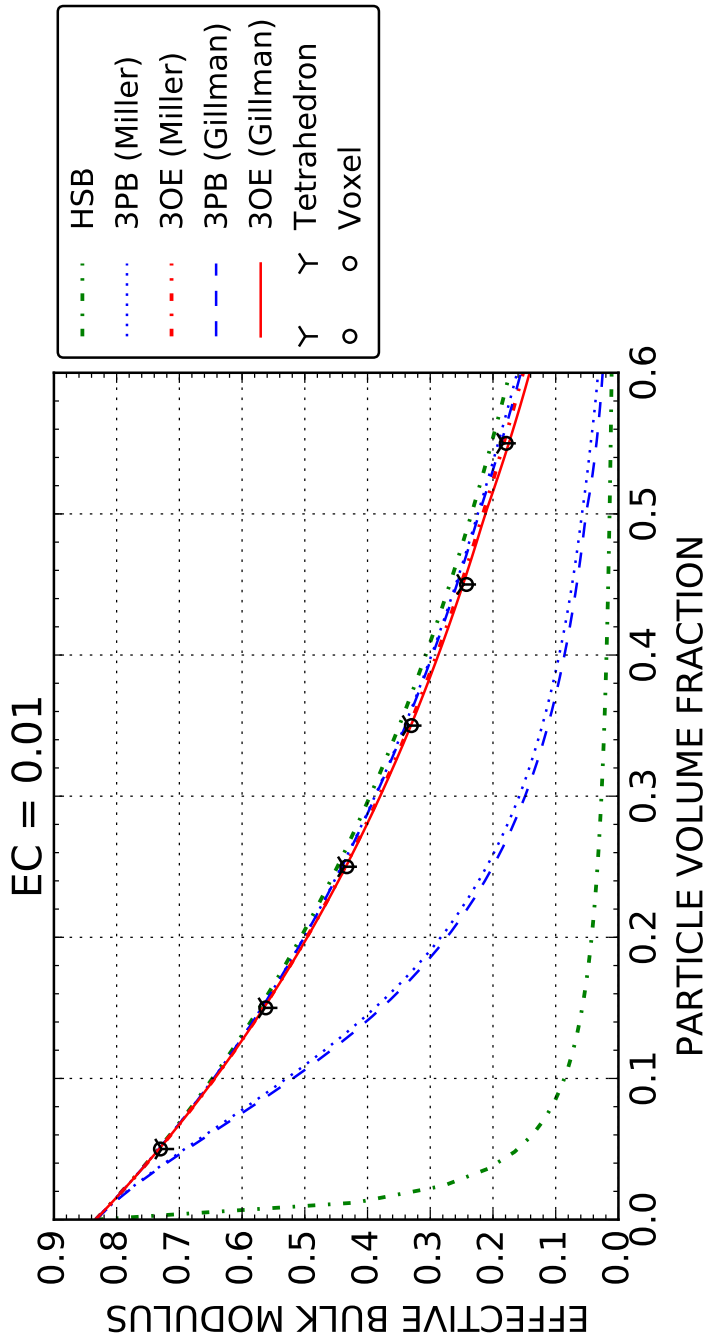

Figure A.15: Effective bulk moduli computed with smooth and voxel meshes in comparison with various bounds and estimates using different three-point statistics. The elastic contrast was $c_{\mathrm{el}} = 0.01$.

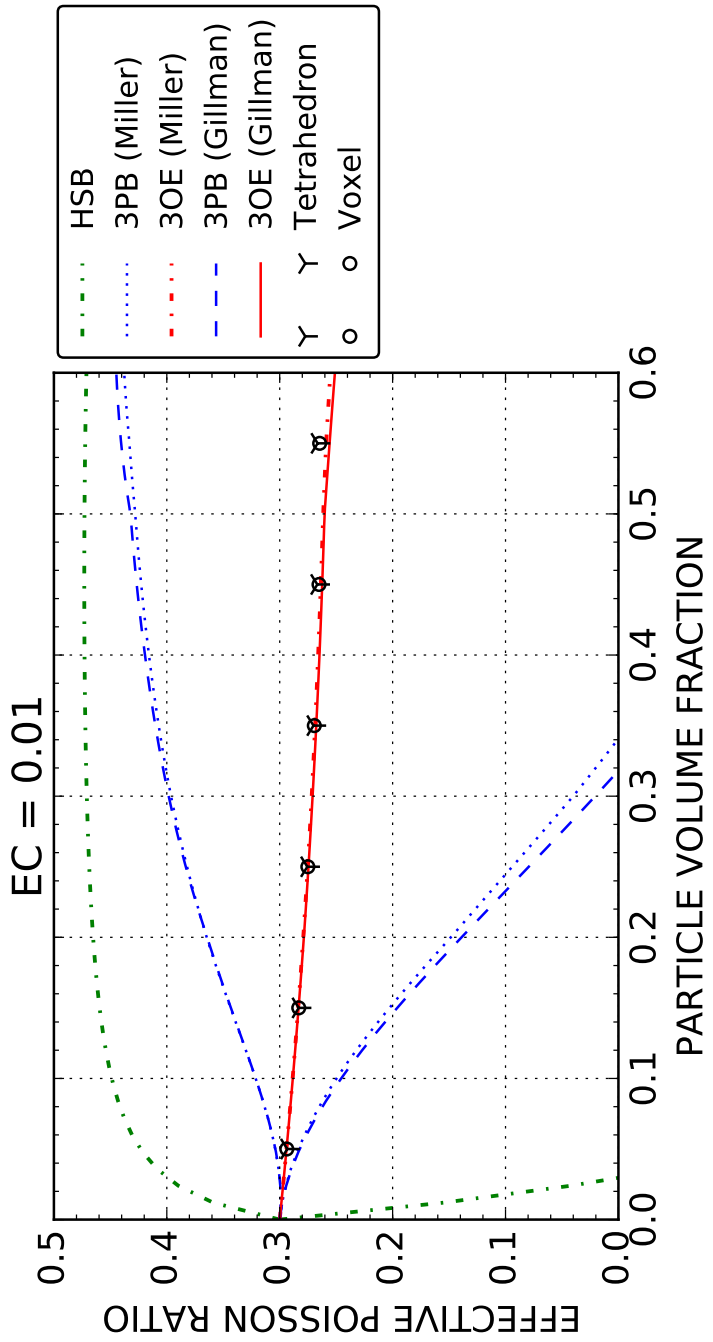

Figure A.16: Effective Poisson's ratios computed with smooth and voxel meshes in comparison with various bounds and estimates using different three-point statistics. The elastic contrast was $c_{\mathrm{el}} = 0.01$.

A.5 Comparison of Degrees of Freedom

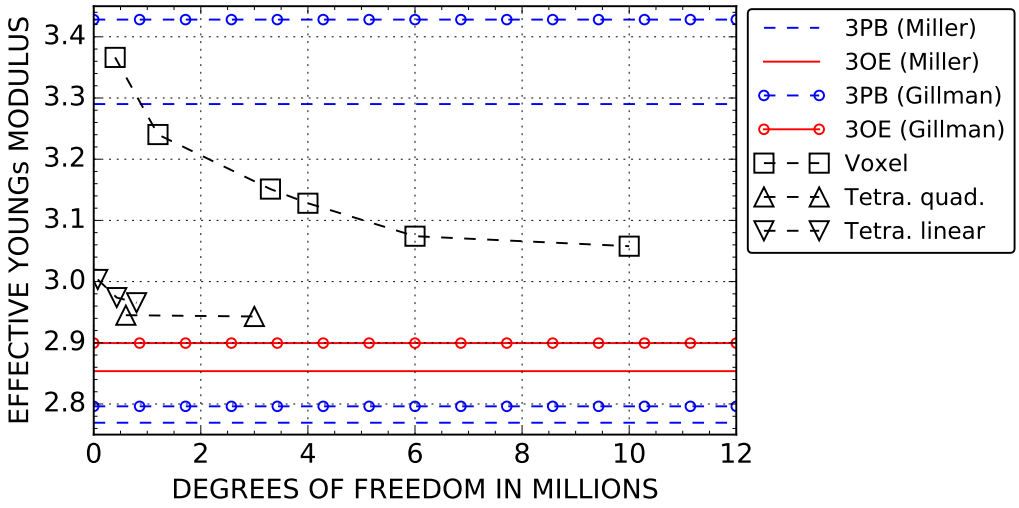

Figure A.17: Convergence behaviour for the effective Young's modulus and different element types in comparison with various bounds and estimates. The analyses consist of 5 statistical equal SVEs, 40 particles each and $\xi_p = 0.55$. The elastic contrast was $c_{el} = 10$.

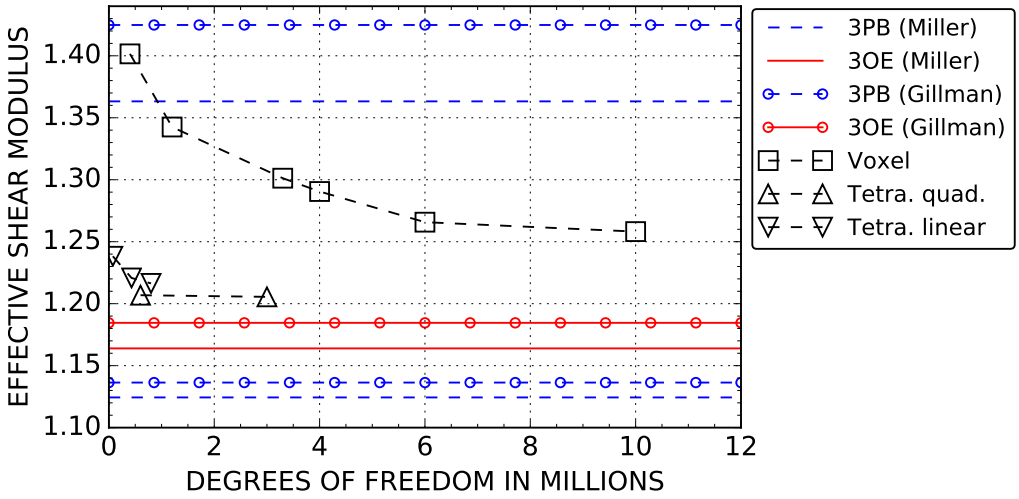

Figure A.18: Convergence behaviour for the effective shear modulus and different element types in comparison with various bounds and estimates. The analyses consist of 5 statistical equal SVEs, 40 particles each and $\xi_p = 0.55$. The elastic contrast was $c_{el} = 10$.

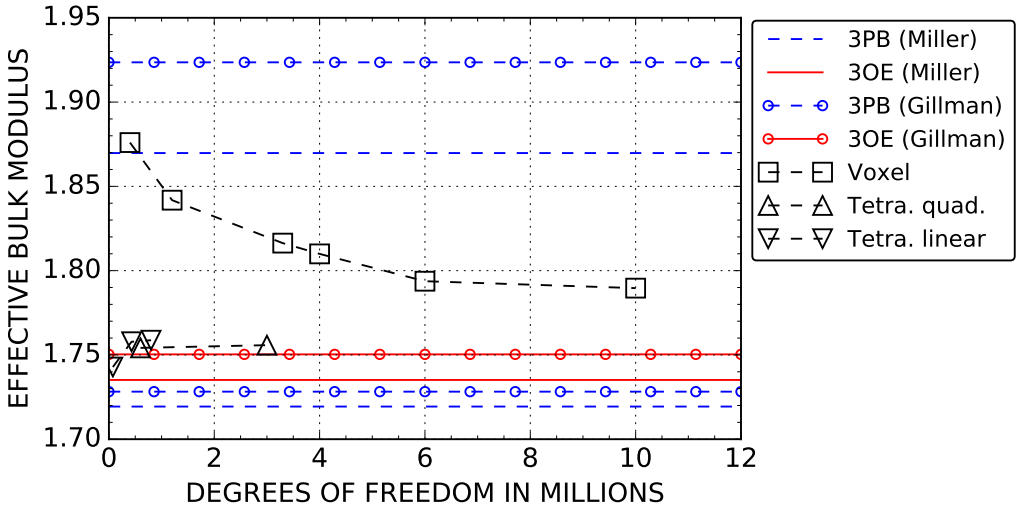

Figure A.19: Convergence behaviour for the effective bulk modulus and different element types in comparison with various bounds and estimates. The analyses consist of 5 statistical equal SVEs, 40 particles each and $\xi_p = 0.55$. The elastic contrast was $c_{el} = 10$.

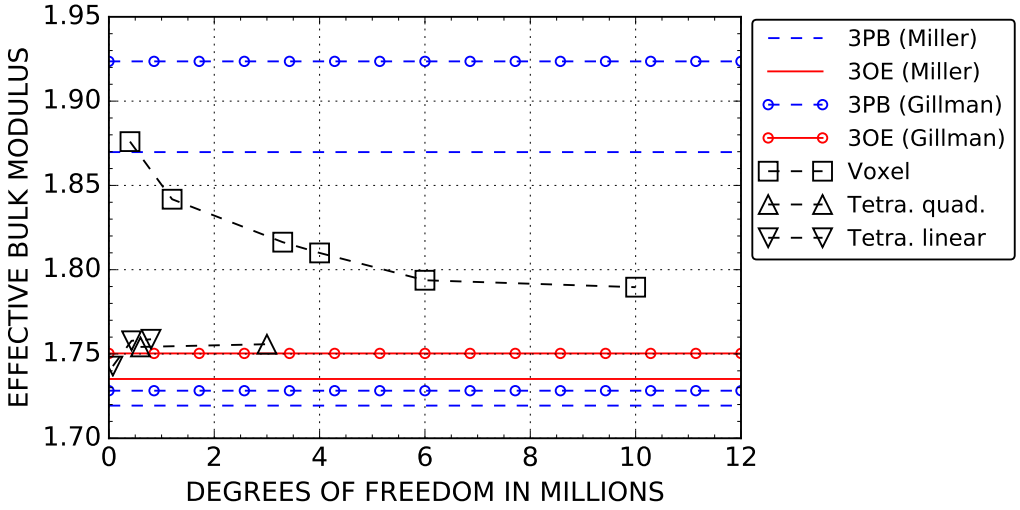

Figure A.20: Convergence behaviour for the effective Poisson's ratio and different element types in comparison with various bounds and estimates. The analyses consist of 5 statistical equal SVEs, 40 particles each and $\xi_p = 0.55$. The elastic contrast was $c_{el} = 10$.

Bibliography

[1] M. Beran and J. Molyneux. Use of classical variational principles to determine bounds for the effective bulk modulus in heterogeneous media. *Quarterly of Applied Mathematics*, 24(2):107–118, 1966.

[2] H.J. Böhm. *Arigen Documentation*. Institute of Lightweight Design an Structural Biomechanics, rev. a-2l/012 edition, 2012.

[3] H.J. Böhm. *A Short Introduction to Basic Aspects of Continuum Micromechanics*. ILSB Report 206. Institute of Lightweight Design an Structural Biomechanics, 2017. URL `https://www.ilsb.tuwien.ac.at/links/downloads/ilsbrep206.pdf`.

[4] X. Chai, M. van Herk, M.C.C.M. Hulshof, and A. Bel. A voxel-based finite element model for the prediction of bladder deformation. *Medical Physics*, 39 (55):55–65, 2012.

[5] T.W. Clyne and P.J. Withers. *An Introduction to Metal Matrix Composites*. Cambridge University Press, Cambridge, 1993.

[6] J.H. Conway and N.J.A. Sloane. *Sphere Packings, Lattices and Groups*, volume 290. Springer-Verlag New York, 2 edition, 1993.

[7] W.J. Drugan and J.R. Willis. A micromechanics-based nonlocal constitutive equation and estimates of representative volume element size for elastic composites. *Journal of the Mechanics and Physics of Solids*, 44(4):491–524, 1996.

[8] J.D. Eshelby. The determination of the elastic field of an ellipsoidal inclusion, and related problems. *Proceedings of the Royal Society A*, 241:376–396, 1957.

[9] A. Gillman, G. Amadio, K. Matouš, and T.L. Jackson. Third-order thermomechanical properties for packs of platonic solids using statistical michromechanics. *Proceedings of the Royal Society London*, 20160060(471), 2015.

[10] Z. Hashin and S. Shtrikman. A variational approach to the theory of the elastic behaviour of multiphase materials. *Journal of the Mechanics and Physics of Solids*, 11(2):127–140, 1963.

[11] R. Hill. The elastic behaviour of a crystalline aggregate. *Proceedings of the Physical Society A*, 65:349–354, 1952.

[12] R. Hill. Elastic properties of reinforced solids: some theoretical principles. *Journal of the Mechanics and Physics of Solids*, 11(5):357–372, 1963.

[13] F.E. Houdaigui, A.F. Forest, S. Gourgues, and D. Jeulin. On the size of the representative volume element for isotropic elastic polycrystalline copper. In Y.L. Bai, Q.S. Zheng, and Y.G. Wei, editors, *Mechanical Behavior and Micro-Mechanics of Nanostructured Materials*. Springer Netherlands, 2007.

[14] J. Huang, K. Krabbenhoft, and A.V. Lyamin. Statistical homogenization of elastic properties of cement paste based on x-ray microtomography images. *International Journal of Solids and Structures*, 50:699–709, 2013.

[15] T. Kanit, S. Forest, I. Galliet, V. Mounoury, and D. Jeulin. Determination of the size of the representative volume element for random composites: statistical and numerical approach. *International Journal of Solids and Structures*, 40: 3647–3679, 2003.

[16] J. Mandel. Contribution théorique à l'étude de l'écrouissage et des lois de l'écoulement plastique. *Applied Mechanics, Springer*, pages 502–509, 1966.

[17] J. Michel, H. Moulinec, and P. Suquet. Effective properties of composite materials with periodic microstructure: a computational approach. *Computer Methods in Applied Mechanics and Engineering*, 172:109–143, 1999.

[18] C.A. Miller and S. Torquato. Effective conductivity of hard-sphere dispersions. *Journal of Applied Physics*, 11(86):5486–5493, 1990.

[19] *Digimat User's Manual*. MSC Software Belgium SA, 2017.0 edition, 2016.

[20] S. Nogales. *Numerical simulation of the thermal and thermomechanical behaviour of metal matrix composites*. Doctoral thesis, TU Wien, Vienna, Austria, 2008.

[21] A.N. Norris. The isotropic material closest to a given anisotropic material. *Journal of Mechanics of Materials and Structures*, 1(2):223–238, 2006.

[22] J.F. Nye. *Physical Properties of Crystals: Their Representation by Tensors and Matrices*. Oxford science publications. Clarendon Press, 1985. ISBN 9780198511656.

[23] M. Ostoja-Starzewski. Material spatial randomness: From statistical to representative volume element. *Probabilistic Engineering Mechanics*, 21(2):112–132, 2006. ISSN 0266-8920. doi: 10.1016/j.probengmech.2005.07.007.

[24] A. Rasool and H.J. Böhm. Effects of particle shape on the macroscopic and microscopic linear behaviors of particle reinforced composites. *International Journal of Engineering Science*, 58:21–34, 2012.

[25] J. Segurado and J. Llorca. A numerical approximation to the elastic properties of sphere-reinforced composites. *Journal of the Mechanics and Physics of Solids*, 50:2107–2121, 2002.

[26] S. Torquato. Effective stiffness tensor of composite media: II. applications to isotropic dispersions. *Journal of the Mechanics and Physics of Solids*, 46(8): 1411–1440, 1998.

[27] S. Torquato. *Random Heterogeneous Materials: Microstructure and Macroscopic Properties*. Springer Science, New York, 2002. ISBN 0-387-95167-9.

[28] S. Torquato, F. Lado, and P.A. Smith. Bulk properties of two-phase disordered media. iv. mechanical properties of suspensions of penetrable spheres at nondilute concentrations. *Journal of Chemical Physics*, 86:6388–6392, 1987.

[29] S. Torquato, C.L.Y. Yeong, M.D. Rintoul, D.L. Milius, and I.A. Aksay. Elastic properties and structure of interpenetrating boron carbide/aluminum multiphase composites. *Journal of the American Ceramic Society*, 82(5):1263–1268, 1999.

[30] K. Watanabe, Y. Iijima, K. Kawano, and H. Igarashi. Voxel based finite element method using homogenization. *IEEE Transactions on Magnetics*, 48(2):543–546, 2012.

[31] R.W. Zimmerman. Hashin–Shtrikman bounds on the Poisson ratio of a composite material. *Mechanics Research Communications*, 19:563–569, 1992.